

Mc

DOC NUM SER CN
UNC31168-PDC A 1




Development Of An Imaging Fourier Transform Spectrometer

Charles W. Pender, Jr.
Sverdrup Technology, Inc.

May 1986

Final Report for Period October 1980 – September 1985

Approved for public release, distribution unlimited.

**ARNOLD ENGINEERING DEVELOPMENT CENTER
ARNOLD AIR FORCE STATION, TENNESSEE
AIR FORCE SYSTEMS COMMAND
UNITED STATES AIR FORCE**

NOTICES

When U. S. Government drawings, specifications, or other data are used for any purpose other than a definitely related Government procurement operation, the Government thereby incurs no responsibility nor any obligation whatsoever, and the fact that the government may have formulated, furnished, or in any way supplied the said drawings, specifications, or other data, is not to be regarded by implication or otherwise, or in any manner licensing the holder or any other person or corporation, or conveying any rights or permission to manufacture, use, or sell any patented invention that may in any way be related thereto.

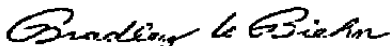
Qualified users may obtain copies of this report from the Defense Technical Information Center.

References to named commercial products in this report are not to be considered in any sense as an endorsement of the product by the United States Air Force or the Government.

This report has been reviewed by the Office of Public Affairs (PA) and is releasable to the National Technical Information Service (NTIS). At NTIS, it will be available to the general public, including foreign nations.

APPROVAL STATEMENT

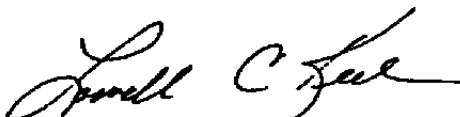
This report has been reviewed and approved.



BRADLEY A. BIEHN, Captain, USAF
Facility Technology Division
Directorate of Technology
Deputy for Operations

Approved for publication:

FOR THE COMMANDER



LOWELL C. KEEL, Lt Colonel, USAF
Director of Technology
Deputy for Operations

UNCLASSIFIED

SECURITY CLASSIFICATION OF THIS PAGE

REPORT DOCUMENTATION PAGE					
1a REPORT SECURITY CLASSIFICATION UNCLASSIFIED		1b RESTRICTIVE MARKINGS			
2a SECURITY CLASSIFICATION AUTHORITY		3 DISTRIBUTION/AVAILABILITY OF REPORT			
2b DECLASSIFICATION/DOWNGRADING SCHEDULE		SEE REVERSE OF THIS PAGE			
4 PERFORMING ORGANIZATION REPORT NUMBER(S) AEDC-TR-86-17		5 MONITORING ORGANIZATION REPORT NUMBER(S)			
6a NAME OF PERFORMING ORGANIZATION Arnold Engineering Development Center	6b OFFICE SYMBOL (If applicable) DOT	7a NAME OF MONITORING ORGANIZATION			
6c ADDRESS (City, State and ZIP Code) Air Force Systems Command Arnold Air Force Station, TN 37389-5000		7b ADDRESS (City, State and ZIP Code)			
8a NAME OF FUNDING/SPONSORING ORGANIZATION Arnold Engineering Development Center	8b OFFICE SYMBOL (If applicable) DD	9 PROCUREMENT INSTRUMENT IDENTIFICATION NUMBER			
8c ADDRESS (City, State and ZIP Code) Air Force Systems Command Arnold Air Force Station, TN 37389-5000		10 SOURCE OF FUNDING NOS			
11 TITLE (Include Security Classification) SEE REVERSE OF THIS PAGE		PROGRAM ELEMENT NO	PROJECT NO	TASK NO	WORK UNIT NO
		65807F			
12 PERSONAL AUTHOR(S) Pender, C. W., Sverdrup Technology, Inc., AEDC Group					
13a TYPE OF REPORT Final	13b TIME COVERED FROM 10/80 TO 9/85	14 DATE OF REPORT (Yr, Mo, Day) May 1986		15 PAGE COUNT 94	
16 SUPPLEMENTARY NOTES Available in Defense Technical Information Center (DTIC).					
17 COSATI CODES		18 SUBJECT TERMS (Continue on reverse if necessary and identify by block number)			
FIELD	GROUP	SUB GR			
20	06	spectroscopy speedmeter			
		infrared			
		technology			
19 ABSTRACT (Continue on reverse if necessary and identify by block number) This study established the feasibility of an Infrared Imaging Fourier Transform Spectrometer (IRIFTS), and the development of a working prototype is described herein. The IRIFTS is a measurement system that can simultaneously acquire spatial, spectral, and temporal IR radiance information. The theory of the components is presented, a more general half-angle obliquity limit is derived for the Fourier Transform Spectrometer (FTS), and the theoretical feasibility of the concept is shown. Commercially available components were acquired, interfaces were constructed, and a one-dimensional (spatial) imaging FTS system prototype was assembled. Results are presented for the operation of the system.					
20 DISTRIBUTION/AVAILABILITY OF ABSTRACT UNCLASSIFIED/UNLIMITED <input type="checkbox"/> SAME AS RPT <input checked="" type="checkbox"/> DTIC USERS <input type="checkbox"/>		21 ABSTRACT SECURITY CLASSIFICATION UNCLASSIFIED			
22a NAME OF RESPONSIBLE INDIVIDUAL W. O. Cole	22b TELEPHONE NUMBER (Include Area Code) (615) 454-7813	22c OFFICE SYMBOL DOS			

UNCLASSIFIED

SECURITY CLASSIFICATION OF THIS PAGE

3. DISTRIBUTION/AVAILABILITY OF REPORT

Approved for public release; distribution is unlimited.

11. TITLE

Development of an Imaging Fourier Transform Spectrometer

UNCLASSIFIED

SECURITY CLASSIFICATION OF THIS PAGE

PREFACE

The work reported herein was conducted by the Arnold Engineering Development Center (AEDC), Air Force Systems Command (AFSC), from October 1980 through September 1985. The results of the research were obtained by Sverdrup Technology, Inc., AEDC Group, operating contractor for propulsion testing at AEDC, AFSC, Arnold Air Force Station, Tennessee, under Project No. DA93. The AEDC/DOT Project Manager was Capt. B. A. Biehn. The manuscript was submitted for publication on March 21, 1986.

CONTENTS

		<u>Page</u>
1.0	INTRODUCTION	5
2.0	MICHELSON INTERFEROMETER THEORY	7
	2.1 Electromagnetic Wave Considerations	9
	2.2 Pathlengths	12
	2.3 Off-Axis Effects	16
	2.4 Resolution and Throughput	23
	2.5 Interferometer Mathematics	24
3.0	DEVELOPMENT OF AN INFRARED IMAGING FOURIER TRANSFORM SPECTROMETER	26
	3.1 IRIFTS Proof-of-Principle Experiments	26
	3.2 One-Dimensional Imaging FTS	31
	3.3 Two-Dimensional Imaging FTS	50
4.0	CONCLUSIONS AND RECOMMENDATIONS	56
	REFERENCES	60

ILLUSTRATIONS

<u>Figure</u>		<u>Page</u>
1.	Michelson Interferometer	8
2.	Ideal Interferometer with Equal Paths and Off-Axis Radiation	14
3.	Ideal Interferometer with Unequal Paths and Off-Axis Radiation	14
4.	Pathlength Difference Schematic	17
5.	Off-Axis Radiation Irradiance	18
6.	Geometries Describing Off-Axis Detectors	20
7.	Off-Axis Detector FOV	22
8.	Optical Setup for Scanning Detector Experiment	28
9.	Transmission Spectra Obtained by Scanning an Image Plane Filled by a Spectrally Varying Source	30
10.	Off-Axis Detector Effects	32
11.	One-Dimensional Imaging FTS	33
12.	Optical Setup Used for 1D Imager	34
13.	FTS Signals	36
14.	Detector Array Equivalent Circuit	38

<u>Figure</u>	<u>Page</u>
15. Block Diagram of Array Signal Control Circuit	39
16. Detector 30 Instrument Responsivity	44
17. Interferogram Displaying Channel Spectra Symptom and IGRAM with that Signal "Fixed"	47
18. Transmission Spectra from the One-Dimensional Imaging FTS	49
19. Emission Spectra of a Propane Flame	51
20. Emission Spectra of an Acetylene Flame	53
21. Emission Spectra of an Alcohol Flame	55
22. IR Camera/FTS System	57
23. IR Camera/FTS 1-D System Results	58

APPENDIXES

A. IR Beamsplitter	65
B. Radiation Transducer	70
C. EOCOM Modulator Specifications	76
D. Detector Array Specifications	76
E. Infrared Measurements and Calibrations	77
F. Infrared Sources	80
NOMENCLATURE	88

1.0 INTRODUCTION

This report describes an investigation that is a part of the research in infrared (IR) measurement technology at the Arnold Engineering Development Center (AEDC), Arnold Air Force Station, Tennessee. The investigation responded to specific developmental requirements for unavailable IR measurement capabilities at AEDC.

The described effort is an investigation into the development of an Infrared Imaging Fourier Transform Spectrometer (IRIFTS). The described IRIFTS system is capable of simultaneously making spectral and spatial infrared radiation measurements. The system concept incorporates a focal plane detector array (which includes multielement detectors, integrated signal conditioning, and involved signal processing) into a conventional Michelson-type interferometer spectrometer to gain spatially resolved information.

At AEDC the need for an IR imaging spectrometer stems from the growing volume of efforts being expended in making measurements of the IR radiation from rocket and jet engine plumes. Spatially, spectrally, and temporally resolved radiometric measurements of the IR signatures of the plumes, produced by rocket and jet engines, are used to evaluate the performance of engines and to identify propulsion systems. Currently, simple radiometers, circular variable filter (CVF) radiometers, scanning IR cameras, dispersive spectrometers, and Fourier Transform Spectrometers (FTS) are used to provide radiometric information. Since these instruments can acquire radiometric data only spectrally or spatially with varying degrees of temporal resolutions, the application of many different kinds of instrument systems is required to assess the character of a source. For example, high-speed radiometers provide temporal information, IR cameras provide spatial information, and spectrometers provide spectral radiance. A map of spatial, spectral, and temporal information is then filled in by extrapolation of the information acquired from the various instruments used. The results of the application of a limited number of different kinds of instruments produces information which is often difficult to correlate and interpret. The results from the individual systems must be interpolated and extrapolated, and the effects of different fields-of-view, instruments responses, data acquisition techniques and so forth must be considered. After all results are considered, then an estimate is made of the spatial and spectral distribution of the plume radiance and of its temporal behavior. Since the estimate may not be an accurate portrayal of the actual source, a more sophisticated measurement technique is needed.

With currently available IR instrumentation, the only instrument capable of mapping the radiance (spectrally, spatially, and temporally) is a high-speed spectrometer. The procedure would consist of either sequentially redirecting the field-of-view of the spectrometer across the source during multiple tests or concurrently applying many identical instrument systems to a single test. These difficult, expensive, and time-consuming processes would introduce

uncertainties due to nonstationary sources and instrument instability associated with multiple firings or multiple instruments. For even moderate spatial, spectral, and temporal resolution, none of the previously mentioned approaches is reasonable.

The problems associated with the use of many instruments or many tests to acquire required information provided the impetus for development of a system capable of rapidly making simultaneous spectral and spatial measurements. The system development is a significant undertaking involving use of state-of-the-art detector arrays and data acquisition systems as well as mechanically sophisticated optical systems. The effort described here is the first step in that development. To provide the desired function a number of concepts were considered. The concepts included an FTS coupled with a mosaic of detectors, an FTS coupled with a scanning IR camera, an FTS coupled with a pyroelectric vidicon, a CVF substituted for the FTS in each of the previously mentioned concepts, a monochromator with scanning mirror and linear array, and various mechanically sophisticated arrangements using one or two monochromators. At the inception of the study, the simplest concepts appeared to be systems incorporating a CVF and monochromator. However, these concepts were determined to include numerous drawbacks which were not apparent with the FTS approaches. Since no FTS imaging system had been developed nor had the theory been discussed in the literature, the first objective of this study was the determination of the feasibility of using one of the FTS concepts. Then if the theoretical feasibility was established, the next objective was to investigate the practicality of developing an operational IRIFTS.

A significant effort was expended in reviewing interferometer theory to establish the feasibility of such a system. However, the classic reviews by Born and Wolf (Ref. 1), Bell (Ref. 2), Mertz (Ref. 3), Martin (Ref. 4), Hecht and Zajac (Ref. 5), Vanasse (Ref. 6), and Steel (Ref. 7) did not adequately describe the situation encountered when dealing with an imaging system. The areas of concern for the theoretical concept were related to the classical half-angle obliquity limit and to beamsplitter behavior. Whether the half-angle obliquity limit imposed too stringent constraints on detector size and location was an unanswered question. Also, whether a nonideal IR beamsplitter could adequately modulate light from extended sources while retaining spatial and spectral information was questionable.

A theory was developed and is presented in Section 2, which offers a more general expression for half-angle obliquity limits to be used with the FTS. The general expression describes limits associated with configuring a spectrometer incorporating a Michelson interferometer and multielement focal plane detector. Proof-of-principle experiments are presented, which demonstrate that spatial as well as spectral information is transmitted through the Michelson interferometer in a retrievable form. A prototype system is described, which has been assembled and evaluated.

The prototype IRIFTS system is a multidimensional [that is, spatial (x), spectral (wavelength), and temporal (t)] IR radiation measurement system. The prototype was assembled from existing optical hardware, detectors, and data acquisition and processing systems, all of which required no extensive modifications. The spectral resolution of the prototype is limited to 16 reciprocal centimeters (cm^{-1}) and is capable of providing simultaneous spectral radiances at 64 spatially (linearly) resolved locations.

The system operational checkout included the determination of the instrument spectral responsivity, the determination of the spatial resolution characteristics of the system, and a series of laboratory measurements demonstrating applications of the instrument.

The underlying concept of this instrument is unique. No commercial instruments based on this concept exist. Only three other exploratory efforts have been reported during the period of this study: some activity by Huppi (Ref. 8) and by Yap (Ref. 9), sponsored by the Air Force Geophysics Laboratory, and investigations by N. J. E. Johnson at Block Engineering (Ref. 10). The approach is timely since the state-of-the-technology in several of the pertinent areas, for example, data acquisition and detector mosaics, has only recently progressed to the level permitting the assembly of the prototype.

2.0 MICHELSON INTERFEROMETER THEORY

In this section some of the theory of the Michelson interferometer is presented since it is the central component of the Infrared Imaging Fourier Transform Spectrometer (IRIFTS). Terminology in this report includes use of the term spectrometer to include the interferometer, collection optics, and detector; the term interferometer refers to a Michelson-type interferometer. More comprehensive descriptions of the Michelson interferometer are available by Bell (Ref. 2), Steel (Ref. 7), and Martin (Ref. 4). The information presented herein is directed toward those issues that are pertinent to an imaging system.

In the Michelson interferometer, radiation is divided at the semi-reflecting surface of a beamsplitter into two beams at right angles. These beams are reflected by plane mirrors to return to the beamsplitter where they are recombined. Variations in pathlengths experienced by the two beams produce interference effects that are apparent in the recombined beam. Figure 1 shows the optical arrangement of the Michelson interferometers used in this study (an EOCOM model FMS 7101 and a Nicolet model HV 8000).

The most unusual optical component in the interferometer is the beamsplitter. In Appendix A the effect of the beamsplitter is considered in some detail since it is the heart of the instrument. The effect of the beamsplitter is first treated from the perspective of the laws

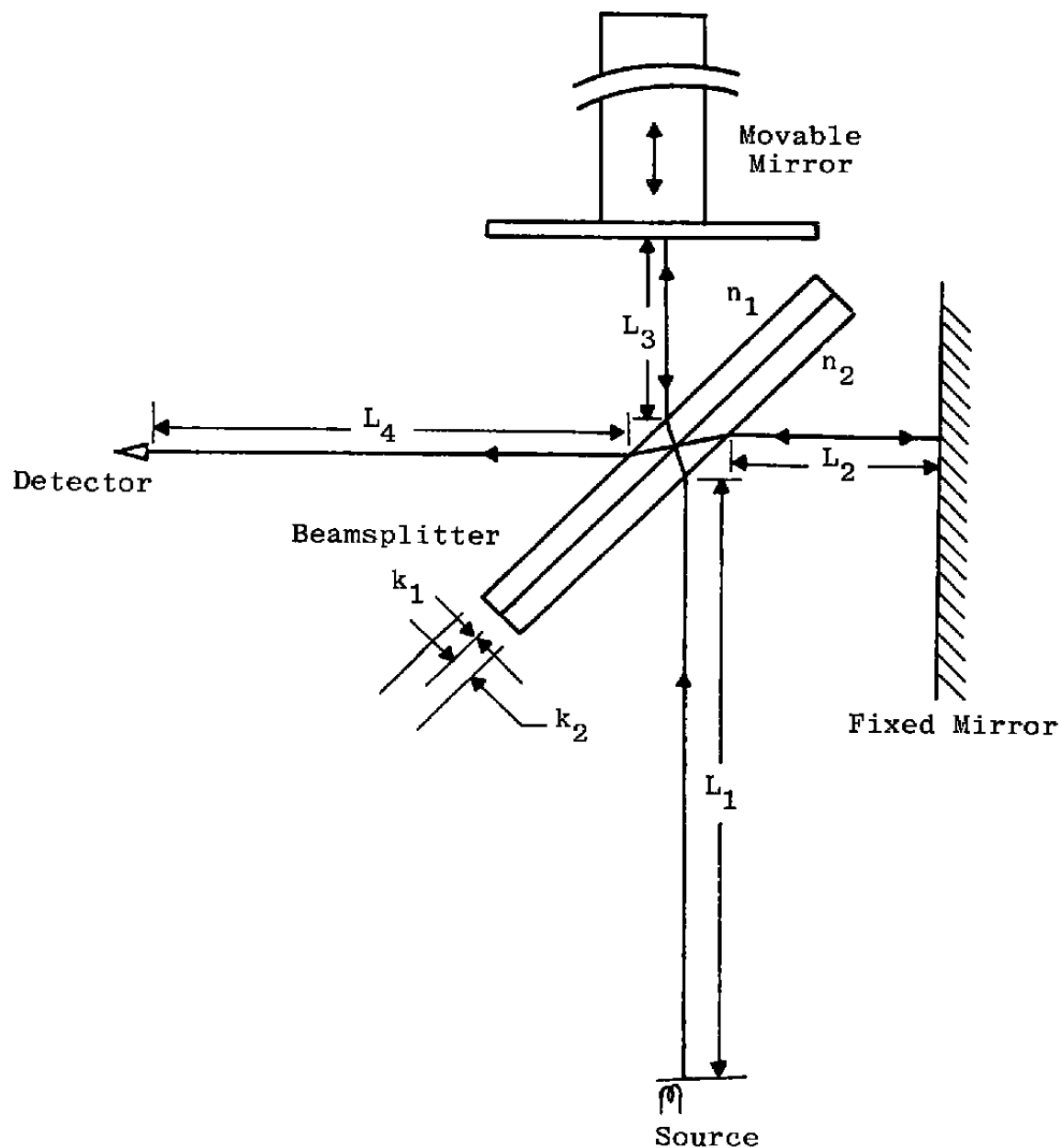


Figure 1. Michelson interferometer.

of reflection and refraction (Snell's law and Fresnel's formulas) with extensions of these laws to absorbing metallic films on transparent substrates. The important features of the beamsplitter are that it divides incident radiation and that moderate variations in its thickness do not significantly impact its performance in the interferometer.

The electromagnetic nature of the light that traverses the beamsplitter is reviewed, as is the effect of superposition of light such as that divided and recombined in the Michelson interferometer. The effect of the movable mirror is then considered since this is the controlled variable in the interferometer. The optical pathlengths of light traversing the interferometer and the resultant irradiance at the exit plane are discussed, after which the effect of an extended source is presented, as well as some discussion of field-of-view and throughput. The classical half-angle obliquity limit is derived, and finally the mathematics necessary to extract spectral information is considered. Sufficient information is provided to show the operation of the FTS and the manner in which data are generated and processed. The references contain numerous articles and texts dealing with various aspects of the Michelson interferometer (Refs. 11 through 24).

2.1 ELECTROMAGNETIC WAVE CONSIDERATIONS

In this section the electromagnetic nature of light is examined to show how the beamsplitter and other interferometer components generate interference effects. The product of the section is an expression [(Eq. (17))] that describes the exiting irradiance from an interferometer caused by some input radiation. The consideration includes the electromagnetic field characterization of the beam, the divided beam, and later the superimposed beams.

The phenomenon of interference of light as exhibited by the Michelson interferometer is best explained by examining the electromagnetic waves that constitute light. A simple linearly polarized plane light wave can be described by constituent electric and magnetic fields (Ref. 5) as

$$\underline{E} = E_0 \cos (\underline{k} \cdot \underline{r} - \omega t) \quad (1)$$

and

$$\underline{B} = B_0 \cos (\underline{k} \cdot \underline{r} - \omega t) \quad (2)$$

where \underline{E} is the electric field magnitude, B is the magnetic field magnitude, \underline{k} is the propagation vector, and \underline{r} is a unit vector that describes a point in space. The energy carried by this electromagnetic wave is described by a Poynting flux, Ref. 25, which is interpreted to describe: (1) the magnitude of the power per unit area that crosses a unit area perpendicular to the energy flow, and (2) the direction of propagation of the wave. In terms of the wave described above, this Poynting vector is (in free space)

$$\underline{S} = (1/\mu_0) \{ \underline{\xi} \times \underline{B} \} \text{ (w/m}^2\text{)} \quad (3)$$

or since $1/\mu_0 = c^2 \epsilon_0$

$$\underline{S} = c^2 \epsilon_0 \underline{\xi}_0 \times \underline{B}_0 \cos(\underline{k} \cdot \underline{r} - \omega t) \quad (4)$$

One of the properties of the Poynting vector (Jackson, Ref. 26) is that the irradiance, E , associated with the light, is the time averaged magnitude of the Poynting vector

$$\begin{aligned} E &= \langle S \rangle = (c^2 \epsilon_0 / 2) [\underline{\xi}_0 \times \underline{B}_0] \\ &= (c/2) \sqrt{[\epsilon_0 / \mu_0]} [\underline{\xi}_0 \times \underline{B}_0] \\ &\quad \text{(Rational MKS units)} \end{aligned} \quad (5)$$

or

$$\begin{aligned} &= c/(8\pi\mu_0) [\underline{\xi}_0 \times \underline{B}_0] \\ &\quad \text{(Gaussian units)} \end{aligned}$$

[Note: For an excellent discussion of different units see Jackson's Appendix (Ref. 26)]

and the irradiance for the plane wave can further be shown to be

$$E = (c\epsilon_0/2) [\xi_0]^2 \quad (6)$$

since $B \propto \xi/c$. Similarly for linear, homogenous, isotropic media, the irradiance is merely

$$E = \{\sqrt{(\epsilon/\mu)}\} [\xi_0]^2/2 \quad (7)$$

Having found the irradiance caused by a single electromagnetic wave, it is now useful to consider two linearly polarized plane waves with the same wavelength

$$\xi_1(r,t) = \xi_{01} \cos(\underline{k}_1 \cdot \underline{r} - \omega t) \quad (8)$$

and

$$\xi_2(r,t) = \xi_{02} \cos(\underline{k}_2 \cdot \underline{r} - \omega t) \quad (9)$$

If the two waves occur at a common spatial and temporal location, the resultant electric field is

$$\underline{E}_{\text{total}} = \underline{E}_1 + \underline{E}_2 \quad (10)$$

and the irradiance attributable to $\underline{E}_{\text{total}}$ is

$$\begin{aligned} E &= \sqrt{(\epsilon/\mu)} \langle \xi_{\text{total}}^2 \rangle \\ &= \sqrt{(\epsilon/\mu)} \{ \langle \xi_1^2 \rangle + \langle \xi_2^2 \rangle + 2 \langle \xi_1 \xi_2 \rangle \} \end{aligned} \quad (11)$$

or following the steps shown by Hecht (Ref. 5)

$$E = E_1 + E_2 + 2(E_1 E_2) \cos(\theta) \quad (12)$$

where $\theta = (\underline{k}_1 \cdot \underline{r} - \underline{k}_2 \cdot \underline{r})$.

The previous discussion can be interpreted, in the case of the entrance plane of the interferometer, to have an irradiance described by Eq. (7). The effect of the beamsplitter is to divide the light into two components, like those in Eqs. (8) and (9), and, after experiencing different pathlengths and recombination after the return pass through the beamsplitter, to produce a resultant irradiance at the exit plane similar to that described in Eq. (12).

The spectral content of the electric field and the spectrally varying nature of the irradiance associated with the light that is passing through the interferometer can be emphasized using a similar set of steps.

More generally the component of the electromagnetic wave traveling along the direction, r , of the interferometer axis can be represented as

$$\xi(r) = \int A(\sigma) \exp\{i(\omega t - 2\pi r \sigma)\} d\sigma \quad (13)$$

where $A(\sigma)$ is the monochromatic magnitude. After traversing an ideal beamsplitter with reflectance, ρ , and transmittance, τ , the light is separated and two waves,

$$\xi_1(r_1) = \int A(\sigma) \rho \tau \exp\{i(\omega t - 2\pi r_1 \sigma)\} d\sigma \quad (14)$$

and

$$\xi_2(r_2) = \int A(\sigma) \rho \tau \exp\{i(\omega t - 2\pi r_2 \sigma)\} d\sigma \quad (15)$$

are produced which add to produce a resultant field

$$\xi(r_1, r_2) = \int A(\sigma) \rho \tau [\exp\{i(\omega t - 2\pi r_1 \sigma)\} + \exp\{i(\omega t - 2\pi r_2 \sigma)\}] d\sigma \quad (16)$$

and in turn an irradiance

$$E(r_1, r_2) = \int A^2(\sigma) (\rho \tau)^2 [1 + \cos\{2\pi(r_1 - r_2)\sigma\}] d\sigma \quad (17)$$

Since, for an interferometer, the two waves originate from the division of a single wave, a more appropriate expression for the irradiance that has passed through an ideal beamsplitter is

$$E = C \int B(\sigma) [1 + \cos\{2\pi \sigma r\}] d\sigma \quad (18)$$

where $B(\sigma) = A^2(\sigma)$, C includes beamsplitter reflectances and the like, and $r = (r_1 - r_2)$. This expression, or more correctly the detector signal resulting from this irradiance, is called the interferogram. Since the interest from our present point of view is the spectral character of the incident irradiance, the varying term is most useful since it has the exact form of the cosine Fourier transform of $B(\sigma)$, and $B(\sigma)$ can therefore be found by performing the inverse cosine Fourier transform.

2.2 PATHLENGTHS

Referring to Fig. 1, the pathlengths of the beams of rays traveling the different paths can be easily calculated. The path of one ray, P1, is from the source to the first surface of the beamsplitter L1; from the front surface of the beamsplitter to the germanium (Ge) layer, $n_1 d_1 / \cos 28^\circ (= k_1)$; from the Ge interface back through the substrate to the front surface, k_1 ; from the front surface of the beamsplitter to the fixed plane mirror, L2; and back, L2; through the substrate, k_1 ; through the Ge film, $n_1 d_1 / \cos 10^\circ (= k_2)$; through the compensator plate, k_1 ; and from the compensator surface to the detector, L4. The pathlength, P1, is therefore

$$P1 = L_1 + 4k_1 + k_2 + 2L_2 + L_4 \quad (19)$$

Following the same logic, the path of the other ray, P2, which travels to the movable mirror is

$$P2 = L_1 + 4k_1 + k_2 + 2L_3 + L_4 \quad (20)$$

where L3 is as shown in Fig. 1. The pathlength difference is seen to be merely the result of a difference between L2 and L3. This treatment presumes identical substrate and compensator plates. Differences from the ideal are considered by numerous authors such as Steel (Ref. 7), Bell (Ref. 2), Vanasse (Ref. 6), Strong (Ref. 12), Loewenstein (Ref. 27), and Sakai (Ref. 28).

It is now useful to present a geometrical treatment of an off-axis ray corresponding to a point on an extended source. In the following treatment Gaussian optics (Ref. 29) are assumed although large angles will be shown in figures. Also the use of a vector approach eases the treatment and is used when convenient.

Figures 2 and 3 are simplified schematics of an interferometer with an ideal beamsplitter and plane mirrors located at equal and unequal distances from the beamsplitter, respectively. Perfect alignment of components is assumed. From inspection of the figure, the pathlengths P1 and P2 appear equal. Here

$$\underline{P1} = \underline{a} + \underline{b} + \underline{c} \text{ and } \underline{P2} = \underline{a} + \underline{d} + \underline{e} \quad (21)$$

where

$$\underline{a} = d\underline{x} + d \tan \theta \underline{y}$$

$$\underline{b} = d \tan \theta \underline{x} + d \underline{y}$$

$$\underline{c} = \frac{d \tan \theta}{\tan (45 + \theta)} \underline{x} - \frac{d}{\tan (45 + \theta)} \underline{y}$$

$$\underline{d} = d \underline{x} + d \tan \theta \underline{y}$$

$$\underline{e} = \frac{-d}{\tan (45 + \theta)} \underline{x} + \frac{d \tan \theta}{\tan (45 + \theta)} \underline{y}$$

and the sum of the two sets of vectors representing the paths are identical. Therefore the path traveled in either circuit of the interferometer, in this case of a perfect instrument with equal pathlengths, leads to the same location on the beamsplitter and indeed to the same location on a detector.

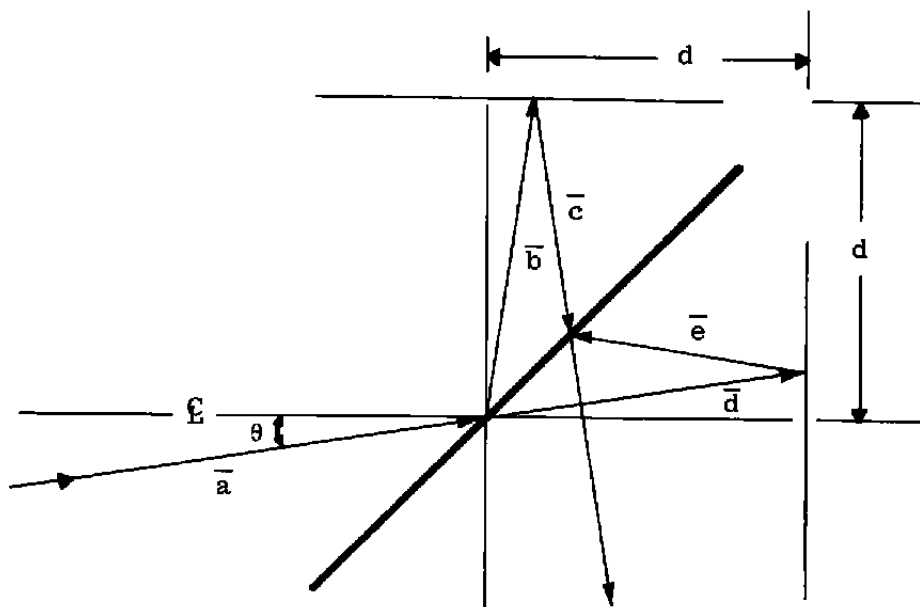


Figure 2. Ideal interferometer with equal paths and off-axis radiation.

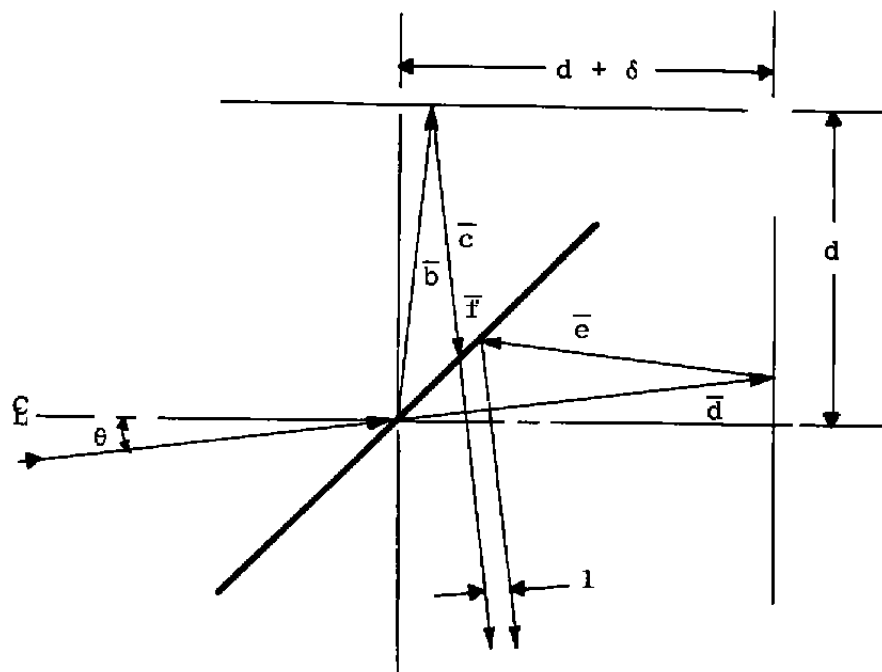


Figure 3. Ideal interferometer with unequal paths and off-axis radiation.

Next it is useful to find the effect of displacing the movable mirror. Figure 3 again presumes perfect alignment but now introduces the case of unequal paths. Again using a vector approach we seek the difference between $\underline{P1}$ and $\underline{P2}$ where

$$\underline{P1} = \underline{a} + \underline{b} + \underline{c} \text{ and } \underline{P2} = \underline{a} + \underline{d} + \underline{e} + \underline{f} \quad (22)$$

and

$$\underline{a} = d\underline{x} + d \tan \theta \underline{y}$$

$$\underline{b} = d \tan \theta \underline{x} + d \underline{y}$$

$$\underline{c} = \frac{d \tan \theta}{\tan (45 + \theta)} \underline{x} - \frac{d}{\tan (45 + \theta)} \underline{y}$$

$$\underline{d} = (d + \delta) \underline{x} + (d + \delta) \tan \theta \underline{y}$$

$$\underline{e} = \frac{-(d + \delta) \sin(45 - \theta)}{\sin (45 + \theta)} \underline{x} - \frac{(d + \delta) \tan \theta \sin (45 - \theta)}{\sin (45 + \theta)} \underline{y}$$

$$\text{and } \underline{f} = -[2\delta \sin^2 \theta \tan(45 - \theta)] \underline{x} + 2\delta \sin \theta \cos \theta \tan(45 - \theta) \underline{y}$$

The resultant separation between beam 1 and beam 2 exiting the interferometer is

$$1 = 2 \delta \sin \theta \quad (23)$$

and the pathlength difference is

$$r = 2 \delta \cos \theta \quad (24)$$

and the exiting beams are propagating at an angle of θ from the axis of the system. This expression and the figure show that off-axis rays are propagated through the interferometer to exit as parallel rays separated by the amount indicated. In the trivial case ($\theta = 0$), the separation is zero, and the exiting angle is also zero, as required.

Before proceeding further it is worthwhile to simplify the schematical presentation being used to make future geometrical ray tracing easier. By stages, one may equivalently describe

the passage of rays through fewer and fewer reflections by merely unfolding our schematical representation (by translating our axis) and ultimately eliminating the beamsplitter. Using the simplified schematic depicted in Fig. 4, in which the beamsplitter has been omitted, the separation, l , the pathlength, r , etc. are much easier to calculate than they were previously.

2.3 OFF-AXIS EFFECTS

The previous geometrical considerations show that in the case of an extended source, an off-axis beam has a slightly different path difference, r , than does an axial beam. With the value of r now known to be related to the mirror displacement, δ , and angle of incidence, θ , by Eq. (23), Eq. (18), presented earlier, can now be restated as

$$E(\delta, \theta) = C \int B(\sigma) [1 + \cos \{2\pi\sigma 2\delta \cos \theta\}] d\sigma \quad (25)$$

and if small angles are assumed

$$E(\delta, \theta) \approx C \int B(\sigma) [1 + \cos \{2\pi\sigma 2\delta (1 - \theta^2/2)\}] d\sigma \quad (26)$$

and the irradiance varies as shown in Figs. 5a and b. These figures show the irradiance for 10- and 2.5- μm radiation as a function of distance (represented in degrees off-axis) from the optical centerline. In the figures the magnitude at $\theta = 0$ deg corresponds to the irradiance at the detector plane on the optical axis. The first minimum occurs at a distance from the optical axis corresponding to an angle of $(\sigma 2\delta)^{-1/2}$.

If the effect of a large source subtending an appreciable solid angle is included

$$E(\delta, \theta) = C \int \int B(\sigma) [1 + \cos \{2\pi\sigma 2\delta \cos \theta\}] d\sigma d\Omega \quad (27)$$

where $\Omega = 2\pi(1 - \cos \theta)$, so that

$$E(\delta, \Omega) = C \int \int B(\sigma) [1 + \cos \{4\pi\sigma\delta - 2\delta\sigma\Omega\}] d\sigma d\Omega \quad (28)$$

Then to find the irradiance at the detector plane, the integration is performed over Ω from 0 to Ω_{\max} and

$$E(\delta, \theta) = C \int B(\sigma) \{1 + \text{sinc}(\Omega_{\max}\sigma\delta) \cos(4\pi\sigma\delta - 2\Omega_{\max}\sigma\delta)\} d\sigma \quad (29)$$

The sinc term ($\text{sinc}\{x\} = [\sin\{x\}/x]$) present in the irradiance expression is associated with the phenomenon discussed above and depicted in Fig. 5. The phenomenon is known as

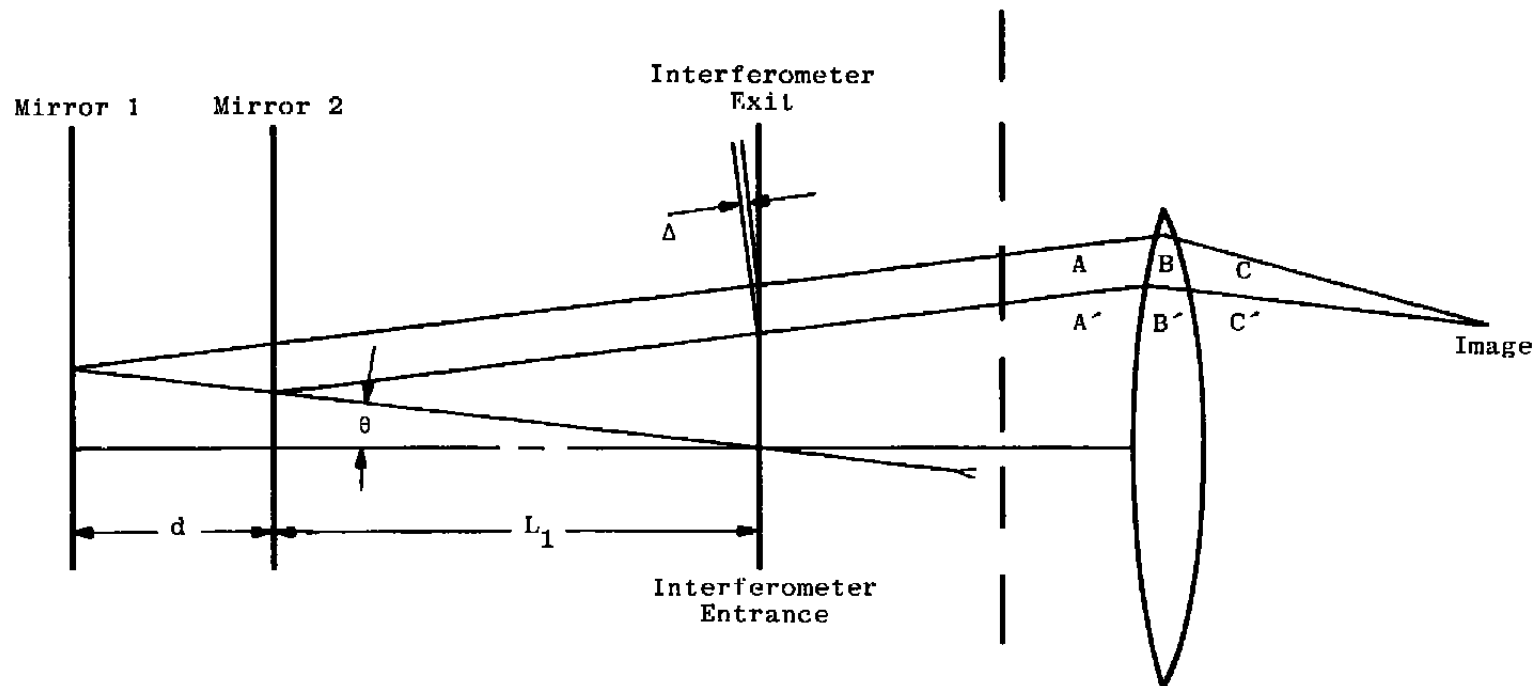


Figure 4. Pathlength difference schematic.

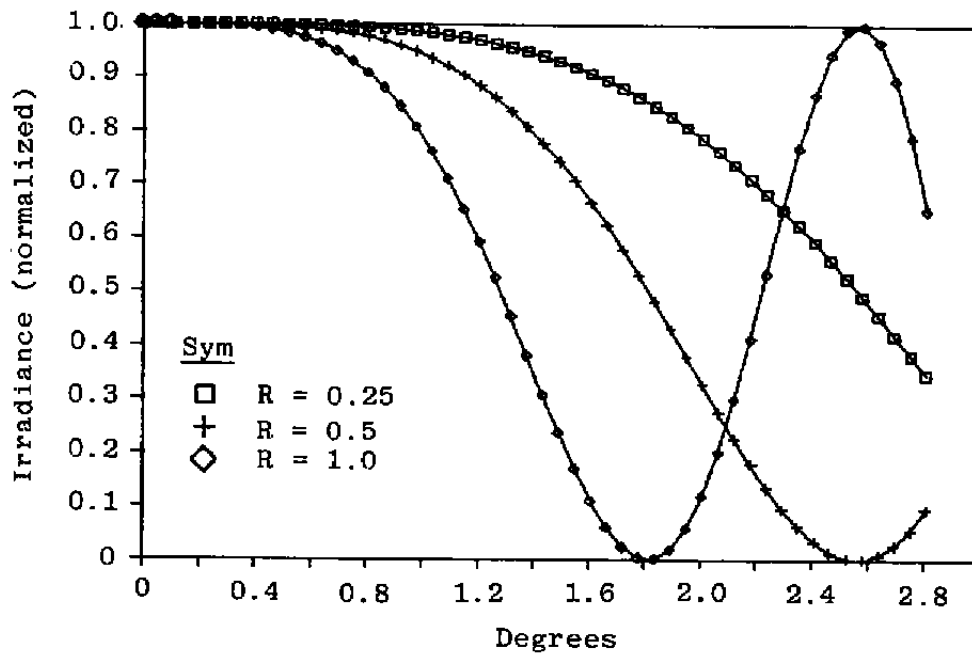
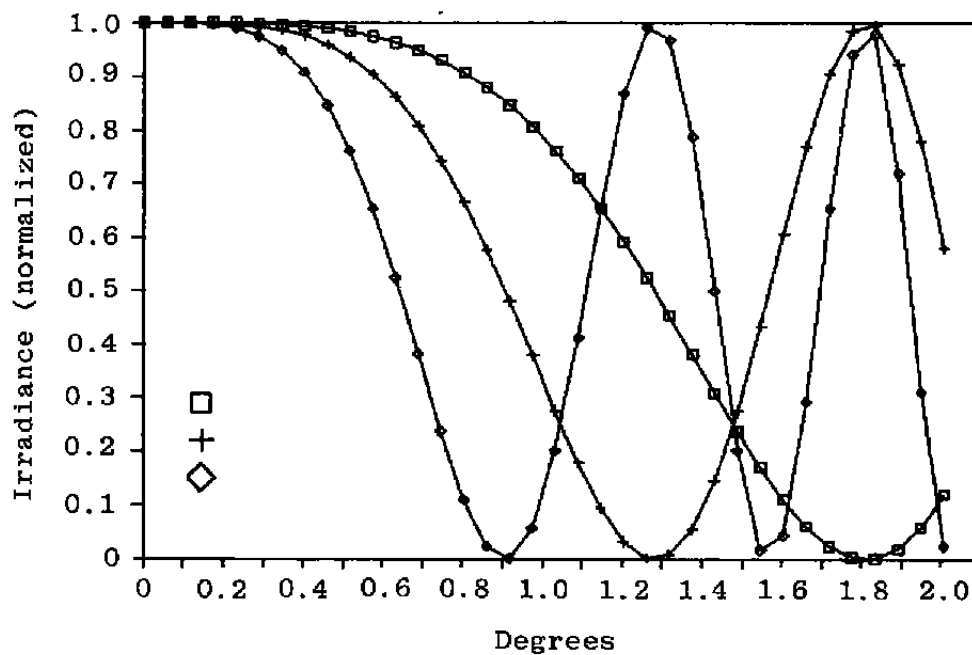
a. 10- μm radiationb. 2.5- μm radiation

Figure 5. Off-axis radiation irradiance.

Haidinger fringes (fringes of equal inclination), which vary in size as a function of pathlength differences and frequency content of the source. A second phenomenon, apparent in the cosine term, is a wave number shift by an amount related to the solid angle.

In the common single detector Michelson interferometer spectrometer, the detector is located on the optical axis, and its size or clear aperture is chosen to remain well within the first fringe described by the sinc function. The first minimum of the sinc function occurs when

$$\Omega_0 = \pi / \{\delta \sigma_{\max}\} \quad (30)$$

but usually (Ref. 14) the limiting aperture is taken as one-half that value or

$$\Omega_{\text{typical}} = \pi / \{2\delta \sigma_{\max}\} \quad (31)$$

and since Ω varies as $\pi\theta^2$

$$\theta = [\Gamma \sigma_{\max}]^{-1/2} \quad (32)$$

where Γ , the optical retardation, is equal to 2δ . This angle is referred to as the half-angle obliquity limit and will be identified by the symbol Υ . The half-angle obliquity limit corresponds to the first minimum associated with the small-angle treatment presented above. This limit is associated with the maximum dimension a detector might have and still receive, across its entire area and over all frequencies of interest and through the complete range of mirror motion, radiation with phase differences less than π .

It is desirable in some cases to have a substantially larger field-of-view than is permissible with the half-angle obliquity limit. Efforts in the past to increase the permissible field-of-view have generally involved the insertion of a variable thickness dielectric compensator plate into the arms of the interferometer. These compensators improve the modulation efficiency over the image plane by being moved in such a way that longitudinal displacement of one of the mirrors does not shift the image, rather, only changes the optical path difference. (For example, see Baker's paper in Ref. 22). This study suggests another way in which the same and even greater fields-of-view might be achieved.

Another approach employing an array of detectors should permit achieving a wider field-of-view as well as producing spatial information about the source. Following a very similar approach as was used to obtain the classic equation [Eq. (29)] describing the irradiance at the detector plane, it is possible to arrive at a different conclusion than that applied to conventional interferometers. The derivation of Eq. (29) was directed toward a detector that extended to cover the solid angle, Ω_{\max} . If smaller detectors located off-axis are assumed

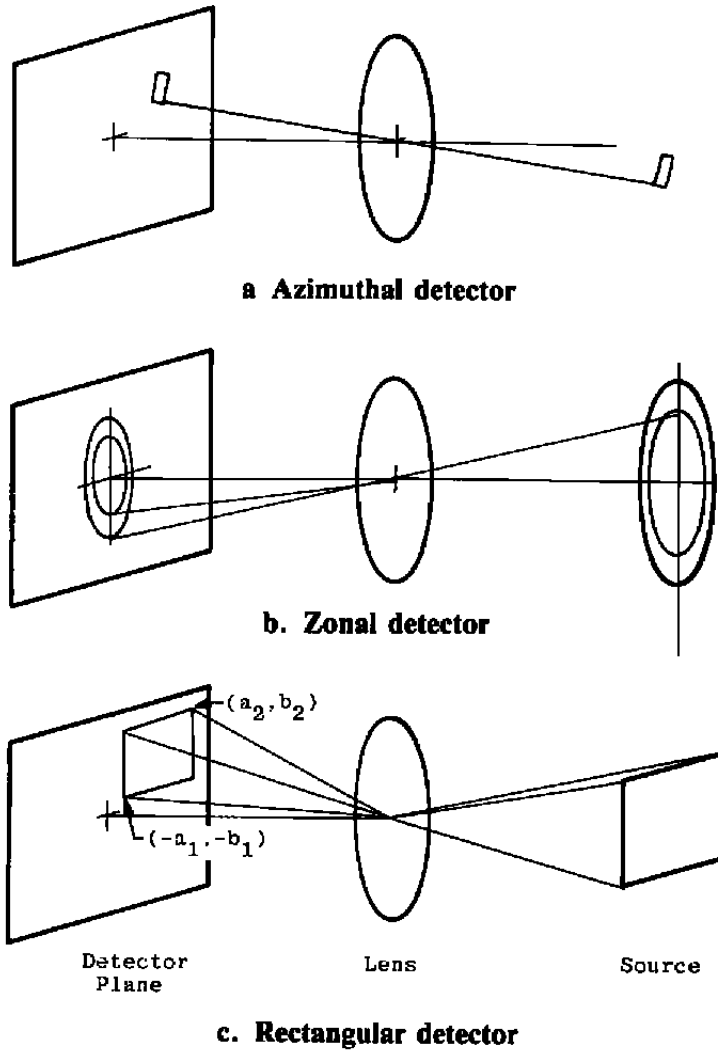


Figure 6. Geometries describing off-axis detectors.

instead, as in Fig. 6, a different expression for irradiance can be obtained. Starting with Eq. (25), it is possible to suggest a detector whose area is defined, in spherical coordinates (Fig. 6a), such that

$$E(\delta) = C \int \int B(\sigma) [1 + \cos\{2\pi\sigma r \cos\theta\}] \sin\theta d\theta d\sigma d\phi \quad (33)$$

with limits of integration of $\phi + \eta$ to $\phi - \eta$ and $\theta + \psi$ to $\theta - \psi$. The result of these integrations is an expression

$$E(\delta) = C' \eta \int \{\sin\theta \sin\psi + \sin[2\pi\sigma r(\sin\theta \sin\psi)] \cos(2\pi\sigma r(\cos\theta \cos\psi))\} d\sigma \quad (34)$$

which can be shown to be equivalent, in the appropriate limits, to Eq. (29). Analysis of this equation and Fig. 5 indicates that small detectors located off-axis may be successfully used at angles substantially exceeding the classic half-angle limit. Using the same steps taken earlier, another limit can be derived for the small off-axis detector. In the previous analysis, the radiation arriving at the large on-axis detector was limited to having phase differences no greater than π . With the same constraint, the half-angle obliquity limit for an off-axis detector can be shown to be

$$\Upsilon = -\tan\theta + [\tan^2\theta + 1/(r\sigma\cos\theta)]^{1/2} \quad (35)$$

which reduces to the classic limit when θ is 0. This limit, while continuing to operate within conventional constraints, permits the use of off-axis detectors outside the classic limit. Figures 7a and b are plots of permissible detector size, for radiation with wavelengths longer than $2\ \mu\text{m}$, to yield 0.5-cm^{-1} and 4.0-cm^{-1} spectra as functions of off-axis positions.

Other investigations have lead to substantiating conclusions. For example, Johnson's work dealing with angular detectors (Ref. 10) shows the irradiance, in an annulus, as shown in Fig. 6b, included between off-axis angles $\Phi - u_1$ and $\Phi + u_2$, to be

$$E(\sigma, \Omega) = C [B(\sigma) \text{sinc}(2\pi\sigma r \sin\psi \sin u_1) \cos(2\pi\sigma r \cos\psi \cos u_1) d\sigma] \quad (36)$$

This equation is similar to Eq. (34) except the previous equation described a small azimuthal section of the annular detector considered here. Results of Johnson's analyses indicate that, for $\psi \geq (4\sigma_{\max} r_{\max})^{-1}$, a "non-classic" half-angle obliquity limit, Υ , for that type detector is

$$\Upsilon = [\{8\}^{1/2} \sigma_{\max} r_{\max} \sin\psi]^{-1} \quad (37)$$

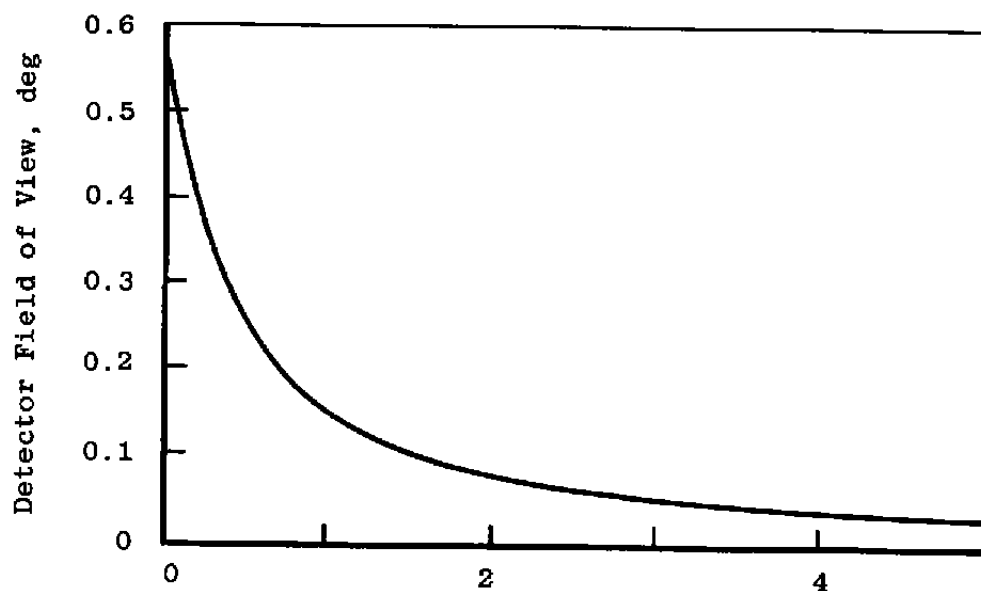
The work of Yap (Ref. 9) follows a similar course with the irradiance of a rectangular detector (see Fig. 6c) described by corner boundaries $(-a_1, -b_1)$ and (a_2, b_2) , being (Ref. 9 and 18)

$$E(\sigma, r) = K B(\sigma) \{F_1 F_2 - F_3 F_4\} \cos(2\pi\sigma r) + (F_1 F_4 + F_2 F_3) \text{sign}(r) \sin(2\pi\sigma r) \} \quad (38)$$

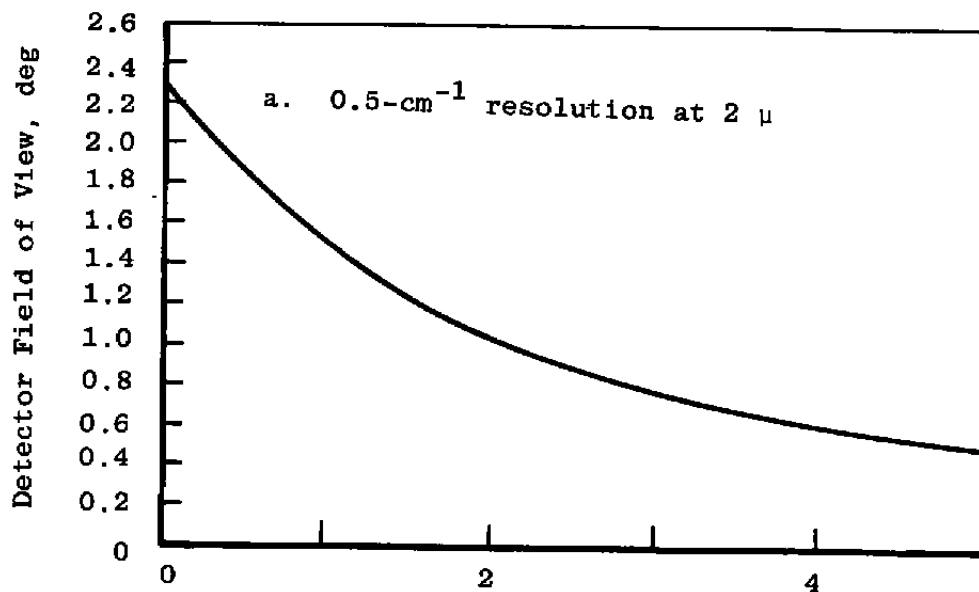
where

K is a constant

$\text{sign}(r) = +1$ for positive retardation



a. 0.5-cm^{-1} resolution at $2\text{ }\mu\text{m}$



b. 8-cm^{-1} resolution at $2\text{ }\mu\text{m}$

Figure 7. Off-axis detector FOV.

– 1 for negative retardation

$$F_1 = ca_1(2\sigma|r|)^{1/2} + ca_2(2\sigma|r|)^{1/2}$$

$$F_2 = cb_1(2\sigma|r|)^{1/2} + cb_2(2\sigma|r|)^{1/2}$$

$$F_3 = sa_1(2\sigma|r|)^{1/2} + sa_2(2\sigma|r|)^{1/2}$$

$$F_4 = sb_1(2\sigma|r|)^{1/2} + sb_2(2\sigma|r|)^{1/2}$$

where

$$c(x) = \int \cos(\pi t^2/2) dt$$

and

$$S(x) = \int \sin(\pi t^2/2) dt$$

are the Fresnel cosine and sine integrals. Results by Yap, while in a different form, also indicate detectors might be used off-axis outside the first fringe of the sinc term in Eq. (29).

The previous discussions of extended sources and off-axis detectors include the presence of a frequency shift attributable to the modified cosine term mentioned first in Eq. (29).

2.4 RESOLUTION AND THROUGHPUT

A maximum retardation was mentioned that can be related to the resolution capability of the interferometer. Several approaches to defining the relationship between resolvability by the interferometer and the retardation required are commonly used. From the experimentalist point of view, it is easiest to resolve two superimposed frequencies if the wave train is examined over a period that includes two interference maxima or minima. Take as an example

$$E = \cos(\omega_1 X) + \cos(\omega_2 X) \quad (39)$$

The first maximum occurs when $X = 0$ and the next occurs when

$$\omega_1 X = n2\pi \text{ and } \omega_2 X = m2\pi \quad (40)$$

since ($\omega = 2\pi f$), for minimum resolvability $m = n + 1$ and

$$X = 1/\Delta f \quad (41)$$

Then using the symbols of our previous discussion, the resolution, $\Delta\sigma$, varies inversely with the retardation

$$\Delta\sigma = 1/r \quad (42)$$

where σ has units of cm^{-1} , and r has units of cm . The resolution is further dependent on other factors (Ref. 30); however, in a properly fabricated instrument, the most significant is the optical retardation of the interferometer.

Another related issue is the throughput or etendue of the spectrometer. In an optical system with two apertures, throughput is the product of the area of one aperture and the solid angle subtended at it by the other aperture. In an imaging system this is the product of the area included within the field-of-view and the solid angle subtended by the entrance pupil at the center of the field-of-view. The smallest throughput encountered within the optical system is the defining element that determines the amount of light that can be transmitted by the system.

For a properly designed Michelson interferometer spectrometer, with the detector offering the greatest restriction, the throughput is found by inserting the value of Ω determined earlier, Eq. (31), in the expression for the throughput

$$T = A \Omega \quad (43)$$

to find the throughput associated with a conventional interferometer

$$T = \{A\pi\}/\{r_{\max}\sigma_{\max}\} \quad (44)$$

For the interferometer using a small off-axis detector the throughput is

$$T = A\{-\tan\theta + [\tan^2\theta + 1/(r\sigma \cos\theta)]^{1/2}\} \quad (45)$$

2.5 INTERFEROMETER MATHEMATICS

The effect the interferometer has on incident radiation has been examined in some detail. We have observed that it modulates input radiation in such a way that the output of the interferometer and a detector is a signal composed of a varying and a nonvarying component

related to the input. We have observed the varying component of the signal, $V(x)$, to have the form of the cosine Fourier transform of the source irradiance, that is

$$V(x) \propto \int B(\sigma) \cos(2\pi\sigma x) d\sigma \quad (46)$$

Therefore with an ideal interferometer, to extract the spectral irradiance information from the electrical signal which varies with path difference in the interferometer, it is merely necessary to find the inverse cosine Fourier transform of the signal. Then

$$B(\sigma) = F\{V(x)\} = 2 \int V(x) \cos(2\pi\sigma x) dx \quad (47)$$

At this point some of the nonideal characteristics can be treated. If the beamsplitter is imperfect, in that the compensator and substrate are not optically identical, and it exhibits a wavelength dependence upon the zero path difference position, an error is introduced. This error, commonly referred to as a phase error, has the effect of adding a phase offset, $\phi(\sigma)$, which results in an electrical signal of the form

$$V(x) = 2 \int B(\sigma) \exp[i2\pi\sigma x] \exp[i\phi(\sigma)] d\sigma \quad (48)$$

which produces a spectrum

$$B'(\sigma) = F\{V(x)\} = B(\sigma) \exp[i\phi(\sigma)] \quad (49)$$

which is the product of the source spectrum plus an undesirable additional phase component. Therefore, in the nonideal interferometer, it is generally necessary to perform a phase correction, PC, to obtain the real spectrum, $B(\sigma)$

$$B(\sigma) = PC\{B'(\sigma)\} \quad (50)$$

This operation effectively multiplies the erroneous spectrum by a correction factor to generate the real spectrum

$$B(\sigma) = B'(\sigma) \exp[-i\phi(\sigma)] \quad (51)$$

It should be mentioned that, in the nonideal interferometer, pathlengths are not infinite and sampling of the signal, $V(x)$, is not continuous. These complications to the ideal case are handled by using the discrete Fourier transform on the discrete, or sampled, data and by multiplying the data by another corrective function, the apodization function, to reduce the finite measurement length effects. For brevity these processes will not be detailed in this

document. For more discussion see Anderson (Ref. 31), or other articles included in the references (Refs. 32 through 36).

3.0 DEVELOPMENT OF AN INFRARED IMAGING FOURIER TRANSFORM SPECTROMETER

In the introduction the need was established for an infrared imaging spectrometer. The concept of using an interferometer and focal plane array of detectors was introduced. The theory of the interferometer was briefly reviewed and extended to include off-axis detectors. At this point in the report, the background material has been presented that is needed for describing the development of the IRIFTS.

The development included first a series of proof-of-principle experiments, then definition of a desired system, followed by inclusion of considerations and compromises to permit a realizable prototype, and finally the construction of two prototypes and their checkout.

3.1 IRIFTS PROOF-OF-PRINCIPLE EXPERIMENTS

At the onset (circa 1979) of the investigation into the feasibility of an imaging spectrometer using an FTS, the concept of using an interferometer as a modulating window into an imaging system was unsubstantiated in the literature, was theoretically questionable, and was perceived as a challenging effort requiring the integration of state-of-the-technology components. The first effort was to experimentally demonstrate that spatially resolvable spectral information was transferred through an interferometer.

During the early conceptual stage of the development, different assumptions were perceived as leading to conflicting forecasts of feasibility. On the one hand, application of Kirchhoff's superposition law to multiple small co-located interferometers suggested that it would be possible to use a focal plane array of detectors with no problem. On the other hand, the classical half-angle obliquity limit associated with interferometer spectrometers suggested problems with using multiple and off-axis detectors. Also the half-angle obliquity limit [Eq. (35)], determined in Section 2, was experimentally unverified. Several experiments were therefore devised to establish the feasibility of the concept. The experiments involved scanning detectors across an FTS image plane simulating a focal plane detector array. At the detector plane, spatial information was expected to be present, as in any other simple optical system, as well as the interference phenomena normally associated with the FTS.

The series of experiments were conducted using an indium antimonide (InSb) liquid-nitrogen-cooled detector on an X-Y traverse mount, a Nicolet HV8000 optical bench, a water-

cooled globar source, a variable aperture, and a circular variable filter. The setup is depicted in Fig. 8.

The interferometer had a germanium (Ge) on potassium bromide (KBr) beamsplitter with 2-in. aperture. The flat interferometer mirrors were 4 in. in diameter. The optics used included M1, M2, and M5, 4-5-in. spherical mirrors with 9.0-in. focal lengths, and M3 and M4, 4.5-in. turning mirrors. As the schematic (Fig. 8) suggests, the globar source was imaged by M1 onto the aperture, which then served as the source. The detector was then imaged onto the aperture using mirrors M5, M4, M3, and M2. Mirrors M2 and M5 served to collimate light which passed through the system.

The use of an InSb detector (discussed in Appendix B) permitted operation of the interferometer modulator at a speed that resulted in laser interference fringes occurring at a frequency of 25.6 kHz. The signal was passed through a high pass filter set at 100 Hz and a low pass filter set at 50 kHz. Various gains were used during the course of the experiment. The gain settings were stored with the data and used during all reductions of the data.

The experiments were conducted with a maximum retardation (optical path difference) of 0.25 cm for 4-cm^{-1} resolution spectra. Interferogram data points were acquired every $1.26\text{ }\mu\text{m}$, so that a maximum frequency of 3950 cm^{-1} could be discerned. The implications of these preceding parameter selections can be found by reexamining the theory of the interferometer and by details of FTS principles of operation, which will be presented in the next section.

The first experiment consisted of scanning the detector across the image plane to determine the image size. In this experiment the distance from the detector to mirror, M5, and aperture to M2 distance were adjusted for an optical gain of unity. A quartz beamsplitter was used during optical alignment for visual confirmation of accuracy of component locations. The next step was the installation of a circular aperture in front of the detector with 0.01-in. diameter to accurately define the detector size. The result of several experiments verified that the optical gain was within 5 percent of unity, as expected. A very nearly uniform interferogram magnitude was produced while the detector was completely covered by source image, and the signal began to be attenuated when the image edge touched and began to move off the detector. The largest aperture used during these experiments was 0.372 in. in diameter, so that the classic half-angle obliquity limit for these experiments, 1.8 deg, was not exceeded. In addition to verifying the optical gain of the setup, the experiment verified that interferograms were produced over the entire source image.

In a second set of experiments, again using the setup of Fig. 8, a circular variable filter (CVF) was located against the back-illuminated aperture and was used as a source. Rather

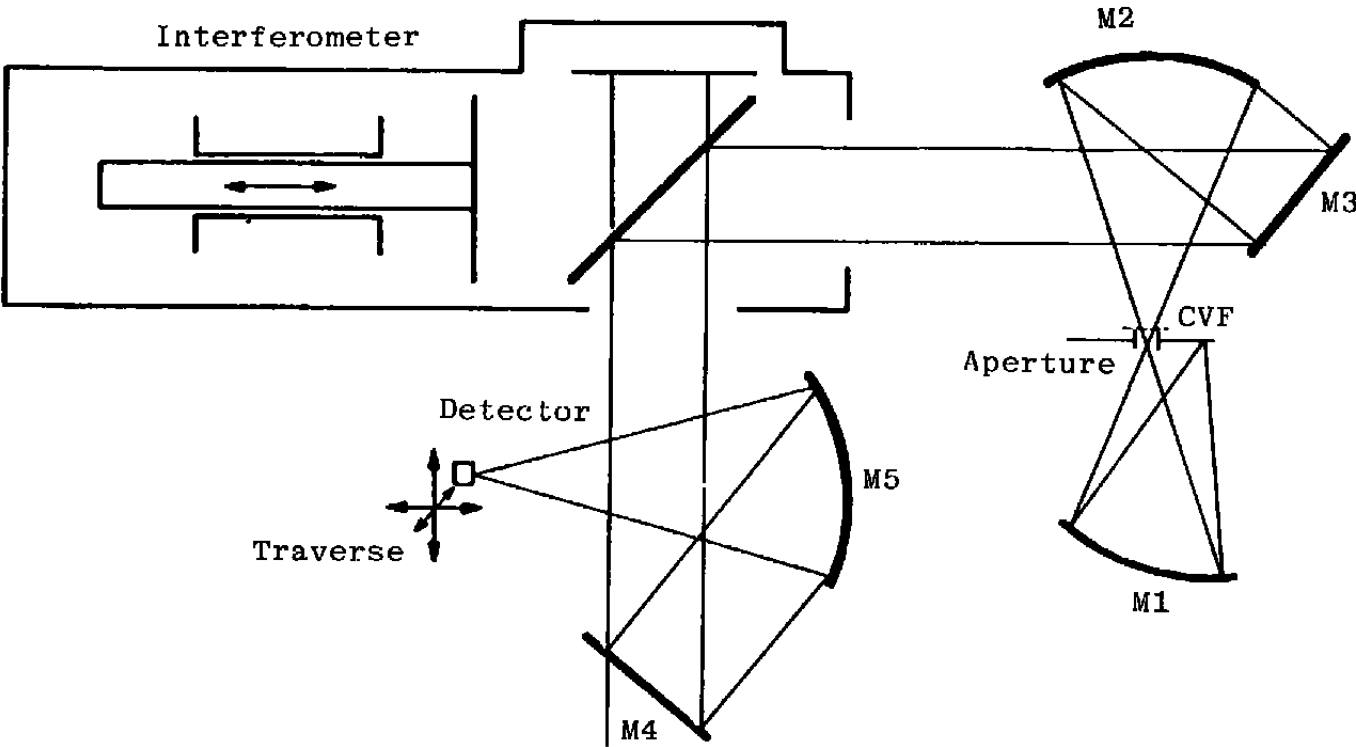


Figure 8. Optical setup for scanning detector experiment.

than calibrating the instrument for an emission measurement, a transmission technique was used. First, data were acquired as the detector was scanned across the image of the CVF, then the CVF was removed and a similar set of data was acquired for the open aperture. The two data sets were processed (using the Happ Genzel apodization function) and then ratioed to generate transmittances for the individual locations across the CVF. Results of this series of experiments are summarized in Fig. 9. The spectra were obtained at 0.05-cm intervals, and the observed transmittances are in agreement with the manufacturer's specifications of spectral variance across the CVF and of magnitude of transmittance. The figure has hidden lines removed for clarity but requires care in interpretation. Figure 9 is meant to illustrate that, at different positions, the transmitted radiation is from different spectral regions. For example, the center of the spectral band of the spectrum located at $x = 0$ is at approximately 4420 cm^{-1} , while the center of the last spectrum (the rearmost), located at $x = 1.65 \text{ cm}$, is at approximately 4100 cm^{-1} .

The results illustrate that at the image plane (within the half-angle obliquity limit) the spectral information is linked as expected with the spatial information. The results are supportive of the feasibility of an imaging interferometer spectrometer built within the constraint of the classic half-angle obliquity limit. From the standpoint of verifying or disproving the half-angle obliquity limit, the experiment was not successful since mechanical limitations prevented exceeding that limit.

A third set of experiments was conducted in which the interferometer was tilted, to duplicate the condition of an off-axis detector, while viewing collimated light that had passed through a sample cell containing HCl gas. Figure 10 shows spectra obtained with the interferometer well aligned and also with the interferometer tilted 1.8 deg. The spectra were generated with 2-cm^{-1} resolution, which is sufficient to discern Cl isotope splitting. The top trace shows the isotope splitting and displays the absorption lines correctly located relative to the wave number axis. The lower trace has reduced magnitude because of vignetting, but continues to show isotope splitting while showing the spectrum displaced from its true position by an amount predicted by Eqs. (29), (34), or (38). The significance of this experiment is two-fold. First, the off-axis detector generates a displaced spectrum as predicted, which must be considered in any work using off-axis detectors. Second, the detector was displaced beyond the classic half-angle obliquity limit without displaying any significant loss of spectral resolution. These observations, together with the results of the analyses done in the previous section on off-axis theory, suggest the viability of constructing an IRIFTS.

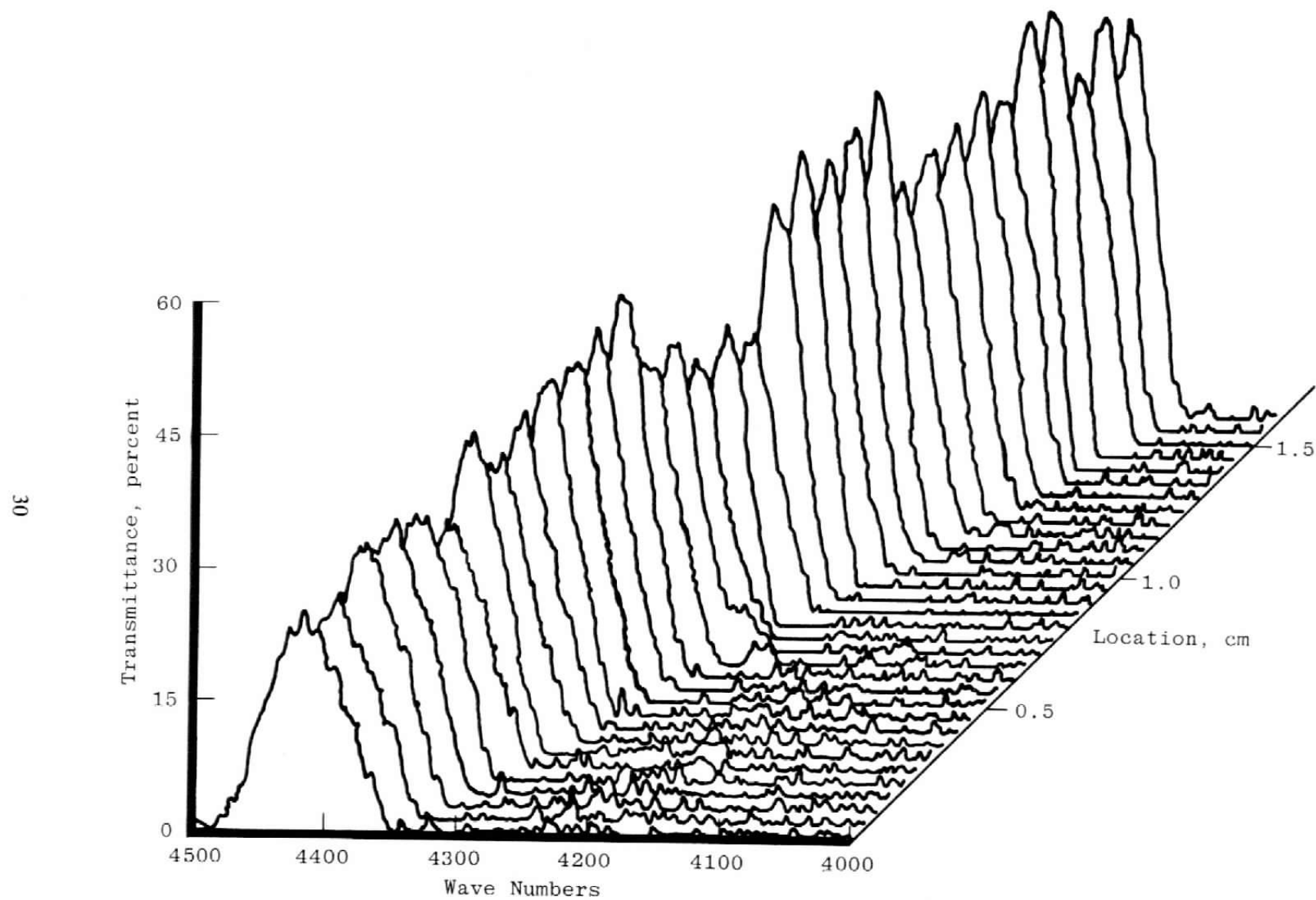


Figure 9. Transmission spectra obtained by scanning an image plane filled by a spectrally varying source.

3.2 ONE-DIMENSIONAL IMAGING FTS

Having substantiated the feasibility of an IRIFTS, by performing the proof-of-principle experiments presented in the previous section, the development of a prototype one-dimensional (1-D) imaging FTS was undertaken. Of the factors dictating the direction of the development, the primary consideration was the availability of components. Considerable importance was also placed on the use of a concept that required no mechanically sophisticated developments. The interferometer which was available for an extended period and for modifications was an EOCOM model 7101. The other major component in the system was the detector array or the IR camera depending upon the approach. The ideal detector was an array of InSb detectors; however, the cost of such an array and the associated signal handling electronics was much greater than could be justified for the demonstration phase of the effort. A Spiricon linear pyroelectric detector array and an AGA model 780 Thermovision® were available and were used. The data system used in the majority of experiments was a Nicolet model 1180E.

The availability and status of the components demanded some compromise from the ideal. For example, the detector array on hand was a linear array and could therefore only be used to acquire 1-D spatial information. The detector type also presented another problem. The pyroelectric detector has a responsivity about three orders of magnitude lower than the InSb detector used in the proof-of-principle experiments. The limitations associated with each of the components were evaluated and a "nonideal" prototype 1-D IRIFTS was assembled. The major limitations of the prototype are the slow scan time required by the detector and data system and the low detector sensitivity.

The concept chosen for implementation uses the configuration shown in Fig. 11. The complexity of the system is such that the principles of operation and shortcomings of the major components are discussed individually before the total system is described. The integrated system is described and results are presented and discussed.

3.2.1 FTS Modulator

The theory of the Michelson interferometer was presented earlier; however, the principles of operation of the modulator will be described in order to point out limitations which will affect the operation of the 1-D imager system.

The EOCOM model 7101 Fourier Multiplex Spectrometer modulator is a stable mount for a movable mirror whose motion produces the interference effects described in the theoretical review. The EOCOM optical head is the predecessor of the Nicolet model HV8000 used in the proof-of-principle experiments. The modulator system is depicted in Fig. 12 and consists

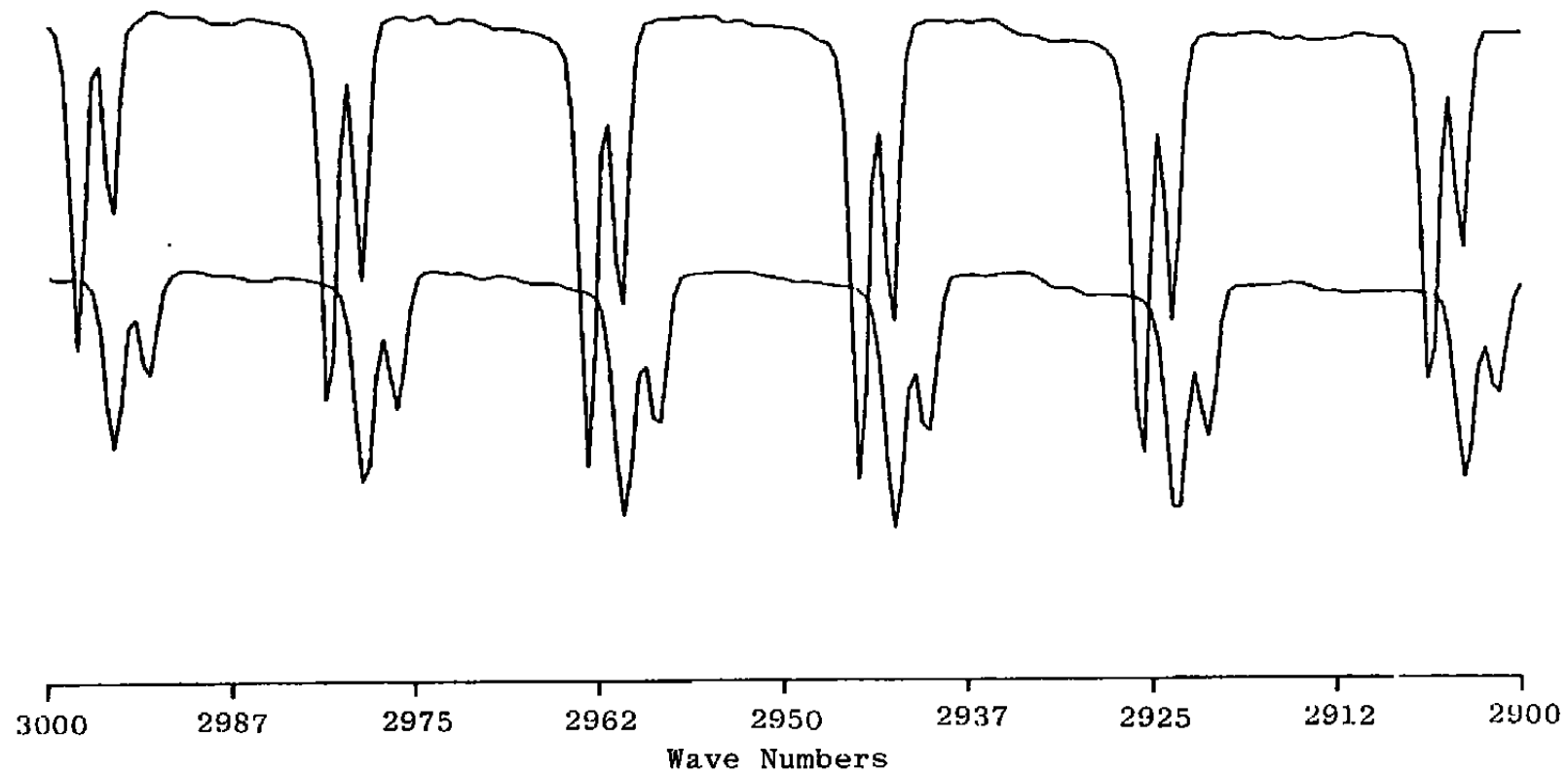


Figure 10. Off-axis detector effects.

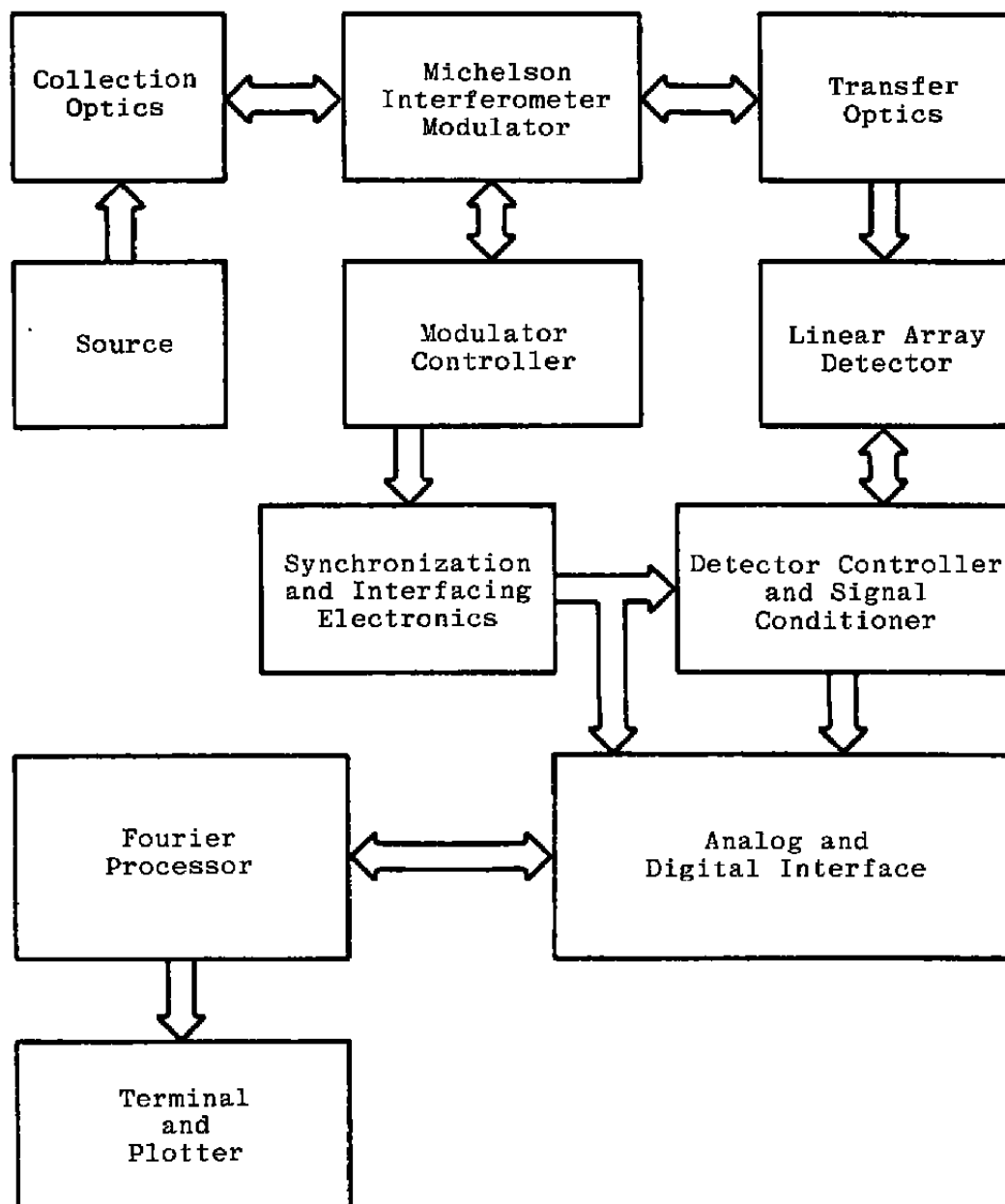


Figure 11. One-dimensional imaging FTS.

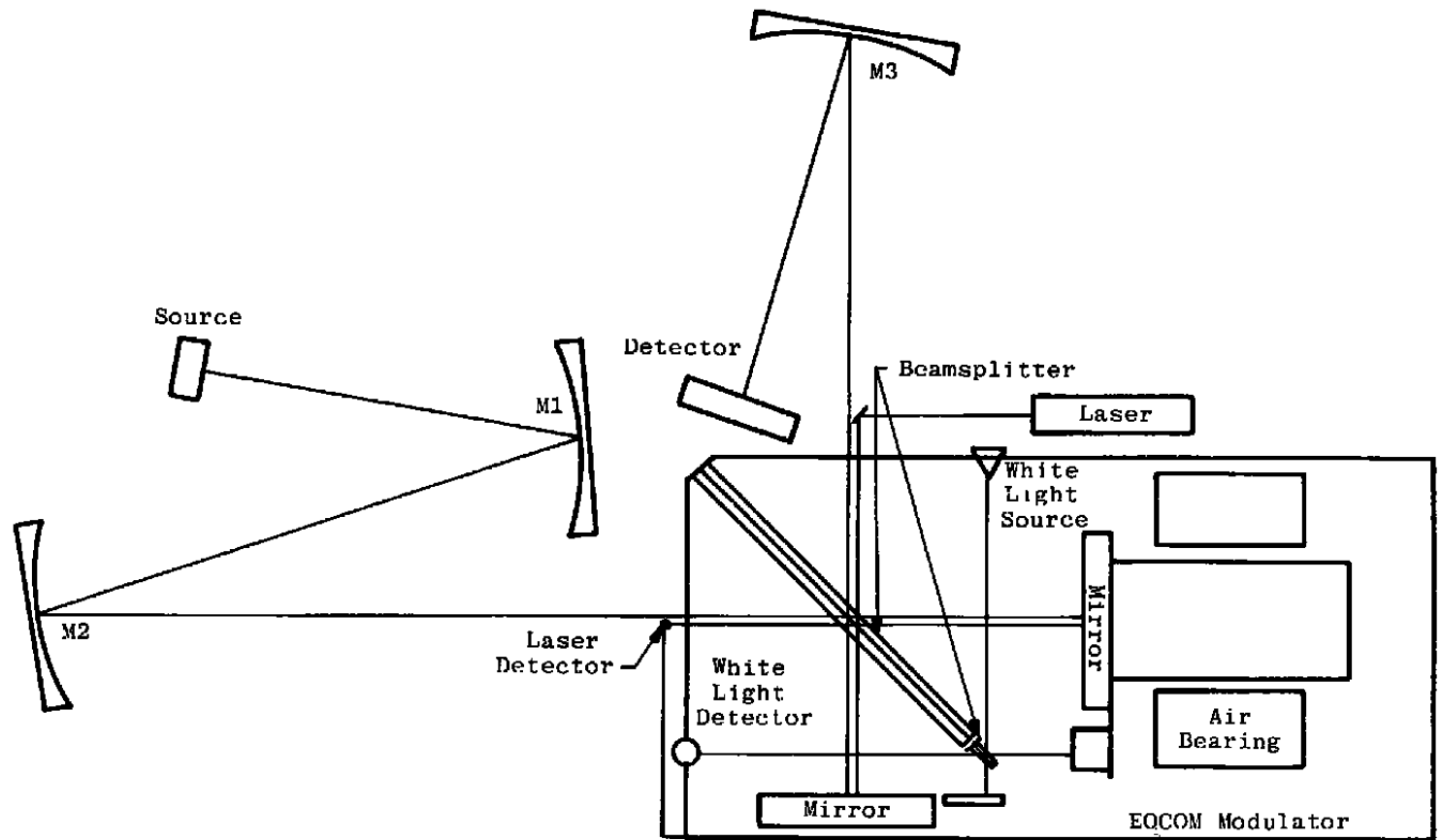


Figure 12. Optical setup used for 1-D imager.

of the IR interferometer, a laser interferometer, and a white light interferometer. The modulator uses a tubular structure in which the moving mirror is supported by air bearings on two precision stainless rods. A linear drive motor provides motive force. The specifications of the instrument are listed in Appendix C. The primary interferometer has 2-in. optics and is intended for the IR radiation. The white light interferometer uses the same mirror drive as the IR mirror and is in the system to provide a well-defined fiducial from which all spatial measurements can be referenced. The laser interferometer in the EOCOM uses an uncoated central region of the IR beamsplitter and the same mirrors as the IR interferometer. The function of this interferometer is to accurately describe the spatial position of the movable mirror while data are being collected.

Figure 13 illustrates the relation between the signals from the three interferometers. The top trace is the signal resulting from an infrared source and shows an interferogram that includes the IR grand maximum (point where the highest voltage occurs), corresponding to a zero path difference between the paths traveled to the fixed and to the moveable mirrors. The bottom trace is the laser interferogram, which is a sine wave caused by the monochromatic (laser) source. The period of the laser interferogram is the wavelength of the laser light being used (in this case the 0.6328- μm HeNe line). The laser signal is input through a zero crossing detector into a digital circuit which generates a synchronization (sync) signal with a period some multiple of the analog laser interferogram. The third trace is the white light interferogram, similar to the IR interferogram. The white light source produces a broad spectrum of short wavelength radiation, which produces an interferogram with a very well-defined white light grand maximum. The white light signal is input to a discriminator, and a signal called "take data" is produced. The mechanical arrangement of the white light mirror versus the IR mirror is such that the white light grand maximum occurs prior to the IR grand maximum. All signals result from the same movable mirror mount motion; therefore, the laser and white light signals indicate mirror displacement or position. The digital signals are used to begin a data collection (while the take data signal is high) and to sample data at precisely known spatial intervals (using the laser synch signal as an analog to digital conversion command).

The control unit provides mirror direction and velocity control and pathlength selection. Velocity control is critical in this application in several ways. First, a very low velocity is required because of the time required to scan the detectors in the array between each laser fringe. Second, any error in the velocity will result in an error in the sampling time; and third, the error, if sufficiently large, will cause the signal frequency to exceed the bandpass of the signal electronics. Each of these problem areas will be readdressed later.

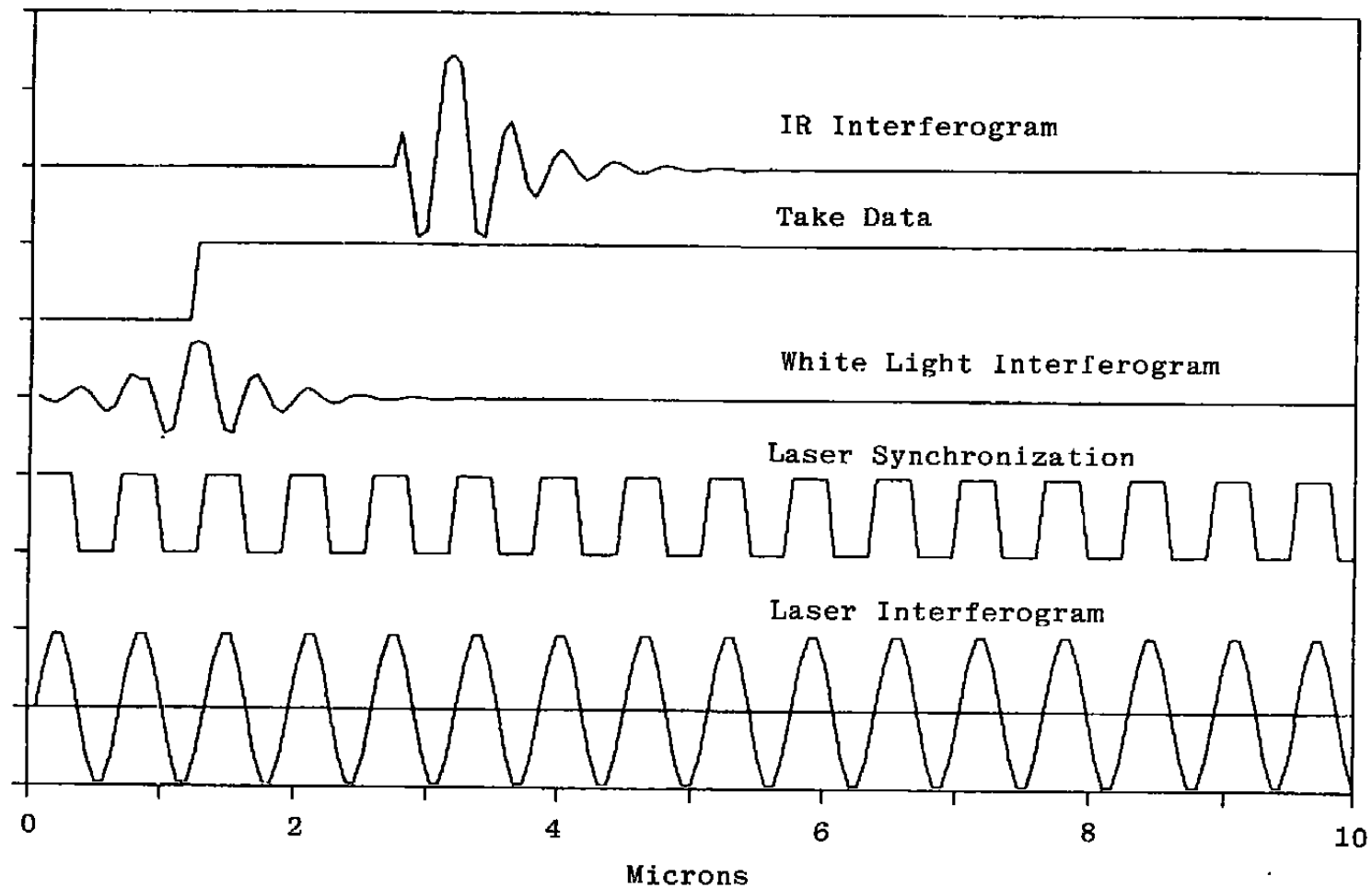


Figure 13. FTS signals.

3.2.2 Pyroelectric Infrared Detector Array System

The prototype of the array of pyroelectric detectors used in this study was developed by C. B. Roundy. A discussion of this type detector is included in Appendix B. The advantages of the detector are its low cost, room temperature operation, and broad spectral range. The disadvantage of the pyroelectric array is its insensitivity. The detectors in the array have a responsivity of 180 v/w and an NEP of 80 nw (array specifications are listed in Appendix D). The detectors are made from lithium tantalate (LiTaO_3) and are covered by a ZnSe wedge-shaped window. The ZnSe is semitransparent from the visible to 22 μm . The wedge shape is to eliminate channeled spectra effects that could be caused from this window.

Although originally thought to have a uniform spectral responsivity from the UV through 22 μm , the detectors have proved to exhibit channel spectra phenomenon in the 2- to 10- μm region. The channel spectra effect occurs because the LiTaO_3 detector is transparent in this region. The front surface of the detector is coated with absorbing film, which allows a substantial portion of the radiation to be transmitted through the film and on through the detector. The radiation is reflected from the support structure at the rear of the detector. Interference effects (channeled spectra) then occur as a function of the wavelength of the incident radiation and the thickness of the detector. These detectors are approximately 50 μm thick and have an index of refraction of approximately 2.15. This channel spectra effect causes a nonuniform spectral responsivity, which will be discussed later in the results section.

Figure 14 is an equivalent circuit for the detector array and the integral scanning electronics. The circuit described by the block diagram in Fig. 15 is used to sequence the shift register scanning circuit that turns the FET switches on and off. On the initial scan the multiplex switch is turned on with the video line grounded to charge each detector to a 5-v bias. During the following period (determined by the interval between start pulses) the bias voltage on each detector is either decreased or increased because of the pyroelectric effect. Then in the next scan the charge generated is transmitted onto the video line for observation. The video is again grounded and the cycle repeated. The output signal obtained from each scan of the 64 element array is a train of 64 charge pulses, each proportional to the change in temperature on the corresponding detector element since the previous scan.

This behavior of the detector, having an output proportional to the change in input radiation, is unique among the detectors typically used for radiometric instrumentation (see Appendix B). In this application the input to the detector is of the form

$$E = C[B(\sigma) [1 + \cos(2\pi\sigma\tau)]d\sigma \quad (47)$$

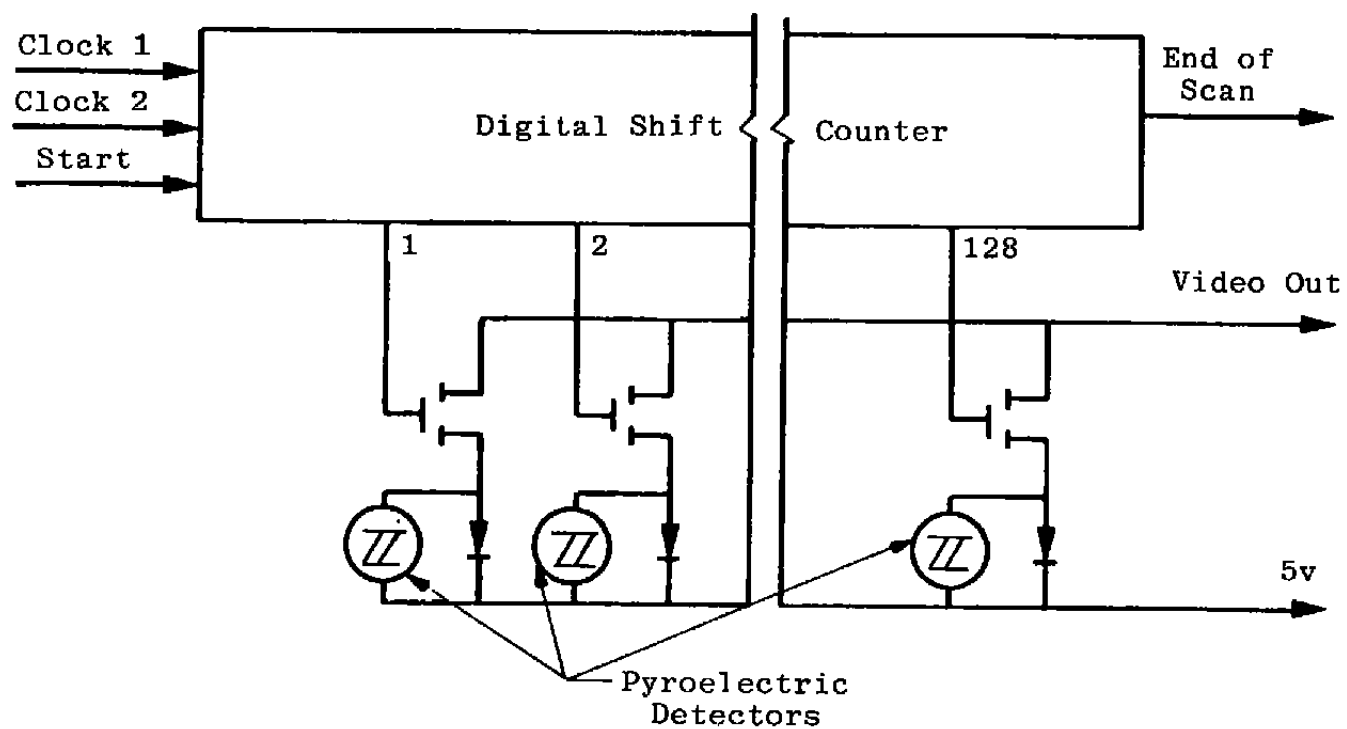


Figure 14. Detector array equivalent circuit.

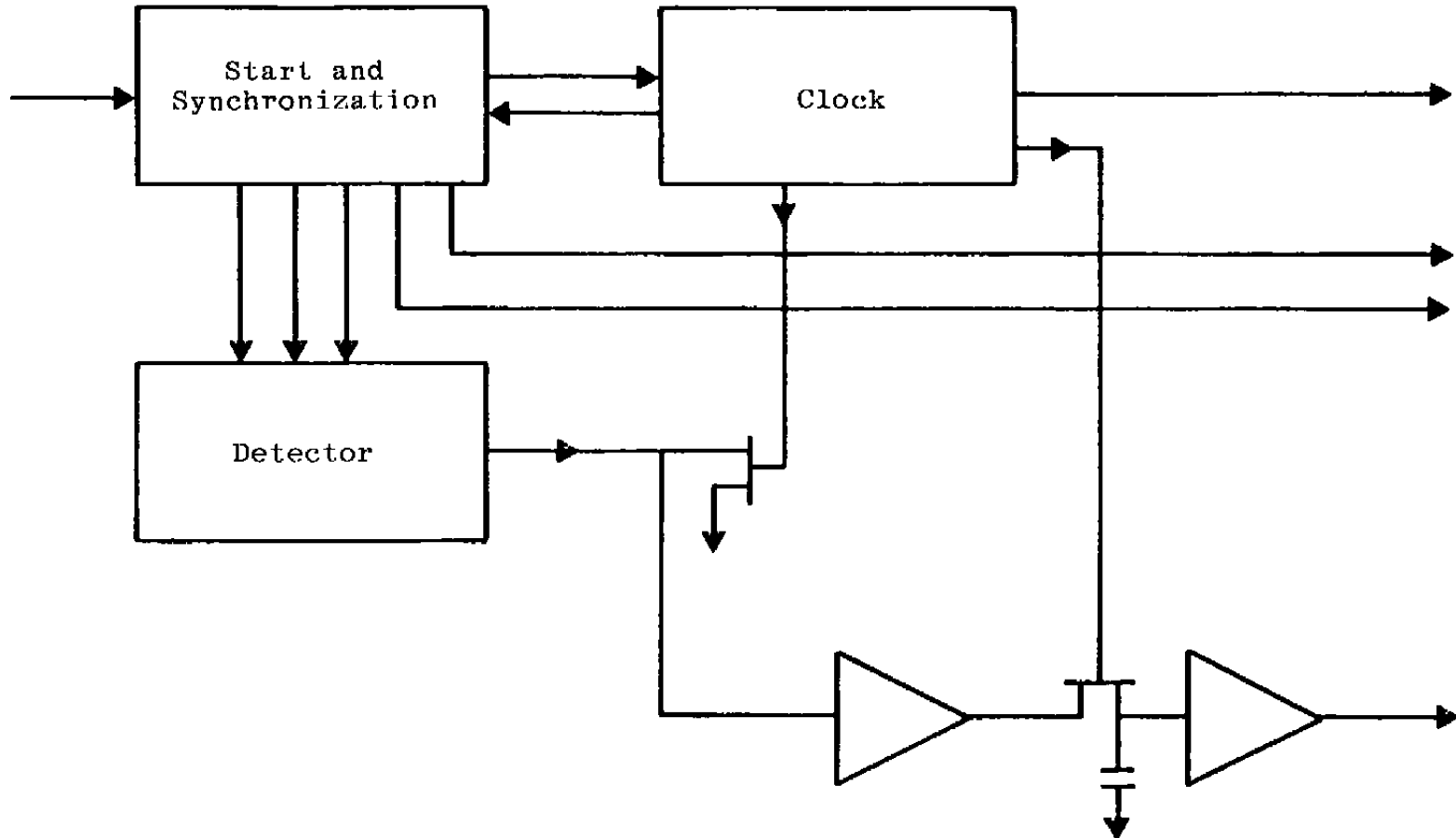


Figure 15. Block diagram of array signal control circuit.

Therefore, since the detector responds to changes, the output is proportional to the time derivative of the input and is

$$dE/dt = C' \int B(\sigma) \sin(2\pi\sigma r) d\sigma \quad (48)$$

where $C' = C \, dr/dt$. The output signal is changed by a 90-deg phase displacement from that from a typical detector. The change from C to C' reflects the fact that as long as the FTS modulator velocity is constant, C' is constant and the instrument response is a function not only of detector and optics characteristics but also the velocity used. Although this factor suggests the detector will function better at higher velocities, that is not necessarily the case.

3.2.3. System Integration of the One-Dimensional Imager

The components depicted in Fig. 11 were assembled. The assembly consisted of the mechanical layout of the optical components and the interfacing of the electrical signals for controls and data acquisition.

3.2.3.1 Optical Arrangement

The optics were setup approximately as shown in Fig. 12 during different experiments. A quartz beamsplitter was used during alignments, and a Ge/KBr beamsplitter was used during data collections. In the optical arrangement shown in Fig. 12, the mirror, M1 (6-in. diam, spherical, 250-mm f.l.) collected radiation from a source and transferred it to M2 (spherical, 4-in. diam, 125-mm f.l.) for collimation. The collimated light then passed through the modulator to M3 (identical to M2) and was focused on the array of detectors. This arrangement has an image of the source located between M1 and M2 in a position convenient for insertion of samples for transmittance measurement. In several of the experiments minor variations were made; however, the same general arrangement was used, and exactly the same optical components were used.

The optical arrangements yielded off-axis detectors located a maximum of 5.8 deg from the optical centerline. The detector size in the dimension parallel to a perpendicular from the optical axis was $360 \, \mu\text{m}$, providing fields-of-view of 0.2 deg. This was within the derived half-angle obliquity limit [Eq. (35)] of 0.28 deg for 4-cm^{-1} resolution and radiation with wavelengths greater than $2.5 \, \mu\text{m}$.

3.2.3.2 Electrical Signals

With reference to Fig. 11, a number of items were considered during the interfacing of the electrical signals generated by the different subassemblies in the system. The modulator controller was modified; the detector controller clock was augmented, and the gain circuitry was optimized; a synchronization and interface unit was designed and fabricated; and the analog signals were amplified and filtered to take advantage of the full dynamic range of the digital data acquisition system.

The mirror motion of the EOCOM modulator is produced by an electromagnetic linear induction motor whose drive circuit is controlled by feedback from an inductively coupled velocity tachometer. Rate-of-motion of the EOCOM in its original form was controlled by a reference voltage provided by a digital-to-analog converter (D/A). The range of available speeds was inadequate for the purposes of the study; therefore, modifications were made to permit much slower velocities. The modifications included reducing the time constant associated with the drive current circuit, replacing the voltage reference circuit for higher resolution, eliminating lengthy cabling to reduce electrical noise pickup and mounting the interferometer on a Newport Research Corporation optical bench using Barry Control vibration isolation mounts. These changes reduced the range of vibrational environments which the interferometer could tolerate but were found necessary to permit adequate reduction of the mirror velocity. The modification made the modulator scan satisfactorily at a slowest velocity of 200 $\mu\text{m}/\text{sec}$.

The slowest modulator velocity realizable and other factors were considered, and a detector array scan rate of 300 Hz was selected. The detector array clock rate (A/D sampling rate) for interrogating each detector element was chosen to be 54 kHz (near the lower limit, see Appendix D). The voltage responsivity of the detector is best when operated with a chopping frequency of 6 Hz with the responsivity diminishing as the frequency is increased. Therefore, if a slower velocity for the modulator could be used, a slower detector scan rate could also be used, and an improvement of responsivity of an order of magnitude could be realized.

3.2.4 Data Handling

In most of the experiments that will be discussed, the data handling was accomplished with a Nicolet 1180E data processor and associated signal conditioners. A part of a state-of-the-technology Fourier transform IR spectrometer, the data system has many features tailored

to the spectral imager development. Some parameters worth attention are a 32K word storage buffer, a 40-kHz average memory to disc transfer rate, a 90-kHz, 15 bit analog-to-digital converter (ADC) with associated signal conditioning, a 10-Mbyte disc, and limited general purpose acquisition software. Data were acquired from either a single detector element or from the entire array. In the event the single detector mode was used, standard software for data analysis was sufficient. In the event the array mode was used, data were acquired serially and required the use of a special demultiplexing data processing program, which was developed to extract single detector interferograms. Individual interferograms were subsequently processed using standard prepackaged software, which performed the functions described in Appendix E.

3.2.5 Results

The 1-D system has been used in numerous experiments to evaluate its performance. As in the case of the proof-of-principle experiments with a scanned detector, results from this prototype substantiate the feasibility of the concept. Three kinds of experiments were performed and will be discussed. The first experiments were conducted to find the spatial resolution of the system. The second experiments produced the instrument responsivity. The third experiments were directed toward spatially varying sources. Some anomalous behavior was observed and will be discussed.

The development of the 1-D imaging spectrometer took place over an extended period because of several problems. The detector originally purchased for the study was a 128-element array of $85 \times 1000\text{-}\mu\text{m}$ detectors, which was discovered to have a sensitivity significantly less than specified and required. Fortunately the manufacturer had expanded his product line to include a 64 element array of $360 \times 2000\text{-}\mu\text{m}$ detectors during the period of the initial investigation and an exchange was made. The larger detectors had eight times the area of the previous ones and were therefore marginally usable. The reduction of the number of detectors reduced the volume of spatial data that could be obtained with a single scan but did not significantly impact the experiments. The most extensive delay involved a data system problem associated with the system disk drive. After a number of unsuccessful attempts by the manufacturer to replace or repair the disk drive, a system upgrade with a Winchester disk system was added, permitting completion of the last set of experiments to be described.

3.2.5.1 Spatial Resolution Experiments

In the first experiments, different optical setups were used to produce various optical gains with different sources being observed. In numerous experiments, basic geometrical optics principles were found to describe the imaging behavior of the system. For example, with

an optical gain of one, a 0.9-in. source produced a 0.9-in. image on the detector array (that is, on 57 detectors) or a 0.3-in. source produced an image on 19 detectors. The only surprises came in the presence of channel spectra in the results and in the amount of time required to perform the data analysis.

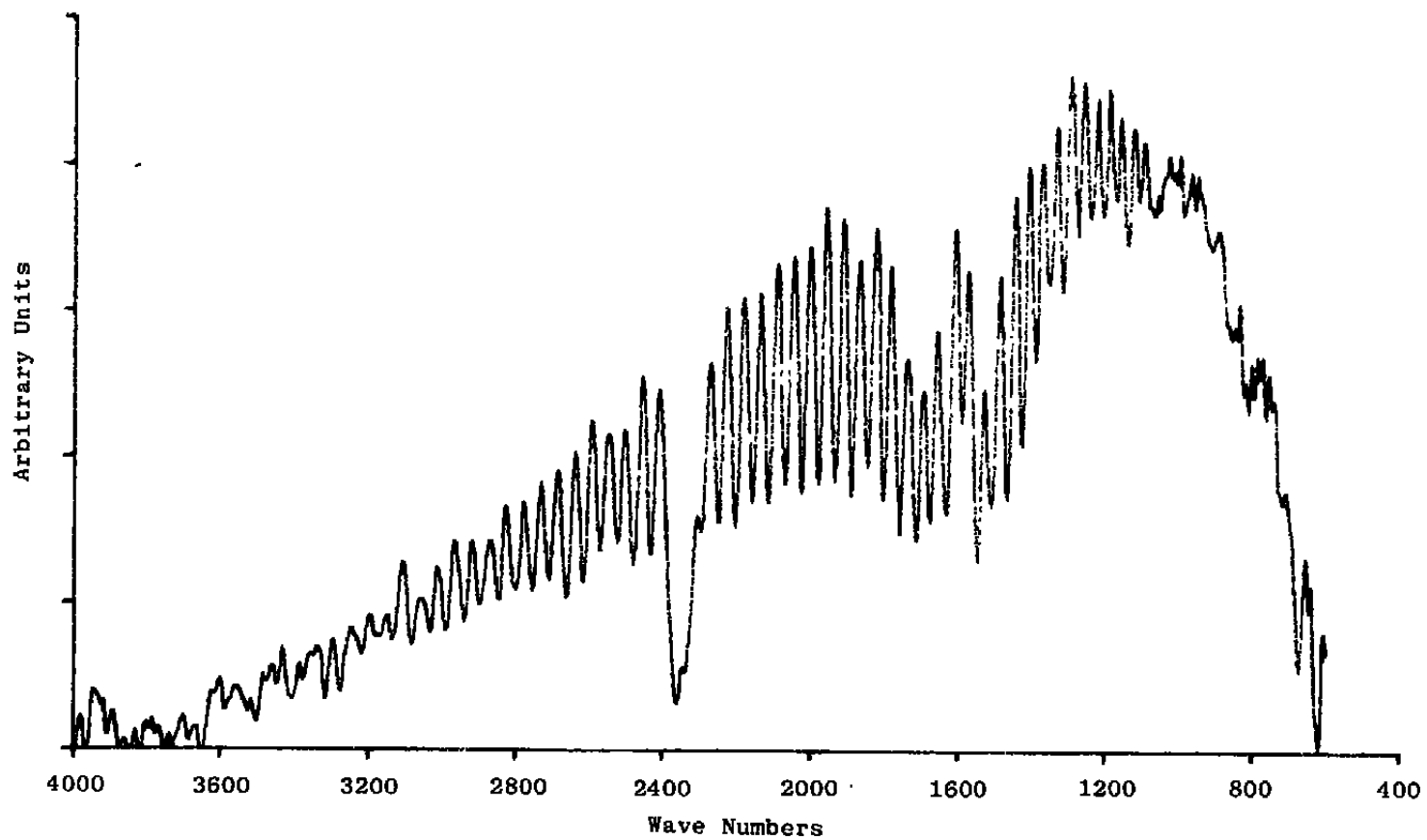
3.2.5.2 Instrument Response

The presence of the channel spectra became very apparent in the course of determining the instrument response for the various detectors. The optical layout included no window, which was thought to be responsible for the effect. After considerable experimentation to find and eliminate the cause, a discussion with the inventor of the detector revealed a recently observed property of the detector. The absorbing film used to flatten the response in the near IR was found to be transparent in the near IR (as is the detector itself). These facts suggested that the channelled spectrum might be generated within the detectors themselves. Calculation of the frequency which would be caused by the detector thickness and refractive index produced the exact experimentally observed frequency. A typical instrument response (from detector number 30) is shown in Fig. 16. For a discussion of the calibration technique used, see Appendix E. Figure 16a shows the channel spectrum phenomenon, which is the high-frequency oscillation superimposed on the spectrum. Figure 16b shows the same spectrum after a "fix" has been applied to the interferogram. The instrument response, Fig. 16b, shows several interesting features. At 2350 cm^{-1} ($4.26\text{ }\mu\text{m}$), atmospheric CO_2 absorption is obvious. Around 1600 cm^{-1} ($6.27\text{ }\mu\text{m}$), H_2O absorption is also obvious. Figure 16c shows a combination of the instrument response as a function of wavelength and a greatly smoothed curve, which has the atmospheric absorption filled in.

In Fig. 17 the technique used to "fix" the interferogram to eliminate the channel spectrum is demonstrated. In the lower trace the oscillations around data point 400 are the classic symptom of channel spectra. The technique of merely filling in a straight line of data in place of the oscillatory data partially eliminates the symptom (Fig. 16b) but has the deleterious effect of degrading the spectrum.

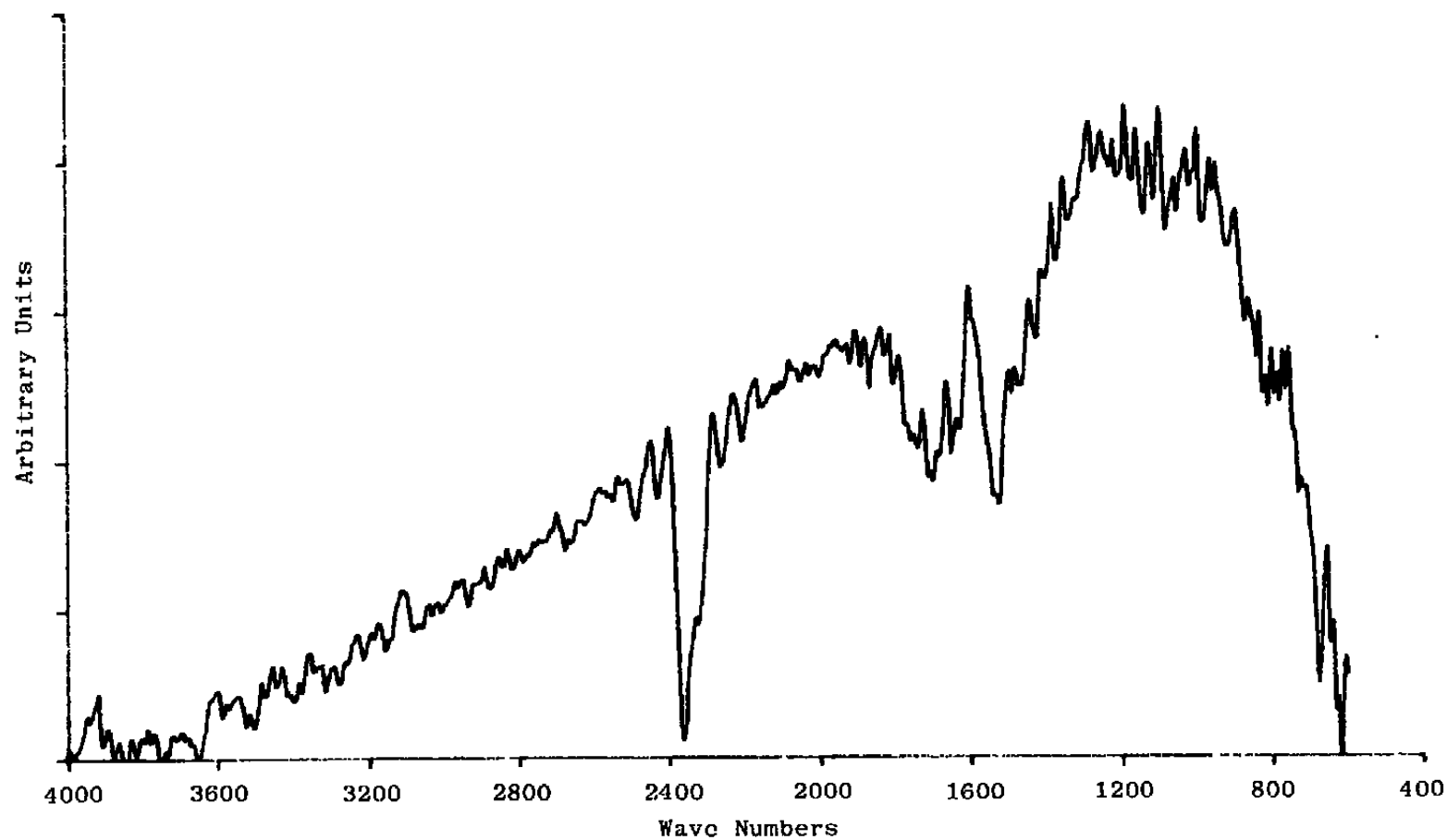
3.2.5.3 Applications

In another set of experiments, the goal was to produce some results that would display the spatial and spectral information gathering power of the instrument. The results presented are representative of the type measurements that can be made with an imaging spectrometer. A number of configurations were used. Data were acquired from identical setups and ratioed to produce near 100-percent transmission spectra, giving confidence in the stability of the instrument. In another experiment, measurements were made of a global source which was

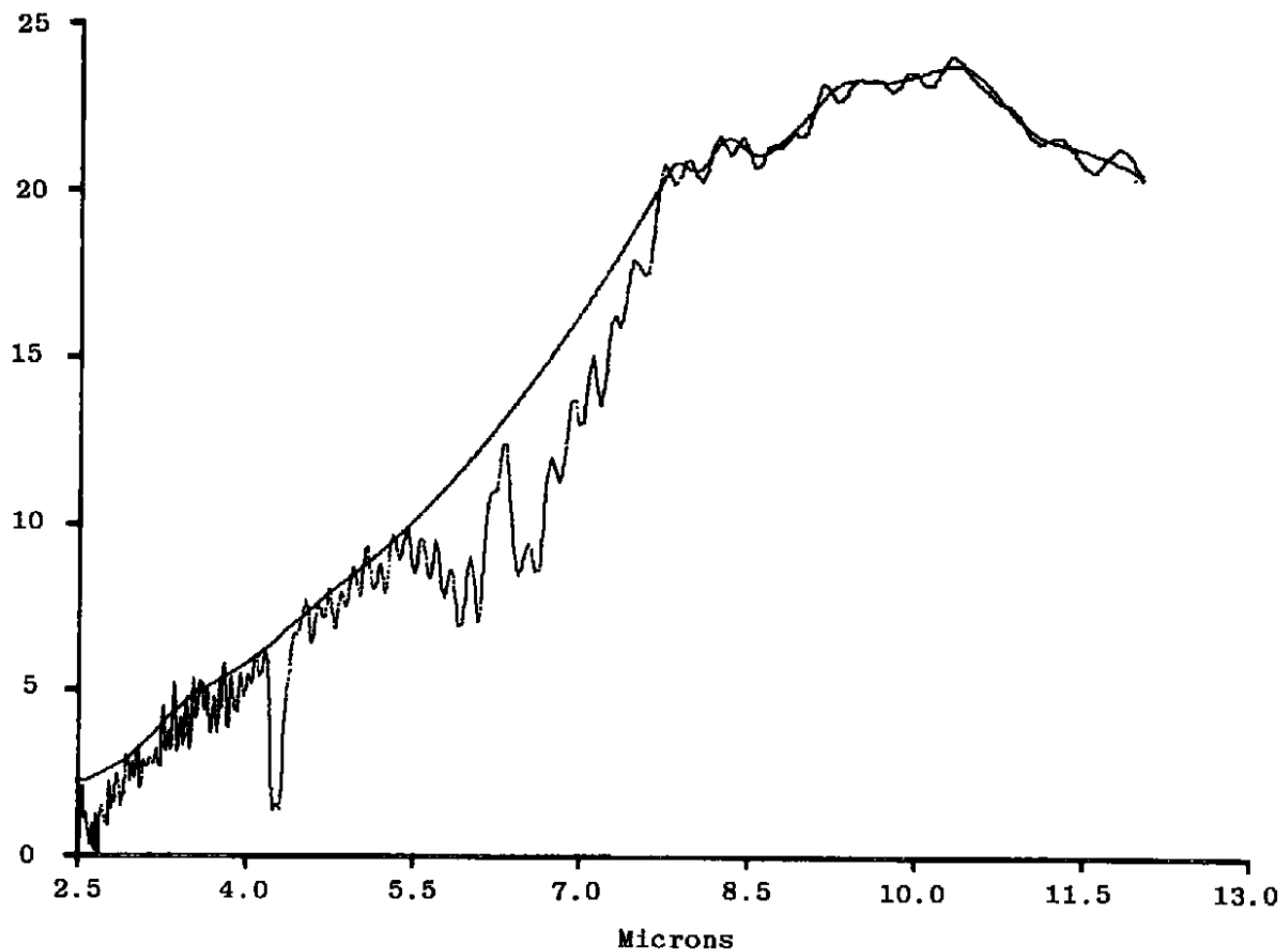


a. With channel spectra

Figure 16. Detector 30 instrument responsivity.



b. With channel spectra removed
Figure 16. Continued.



c. Converted to micron scale
Figure 16. Concluded.

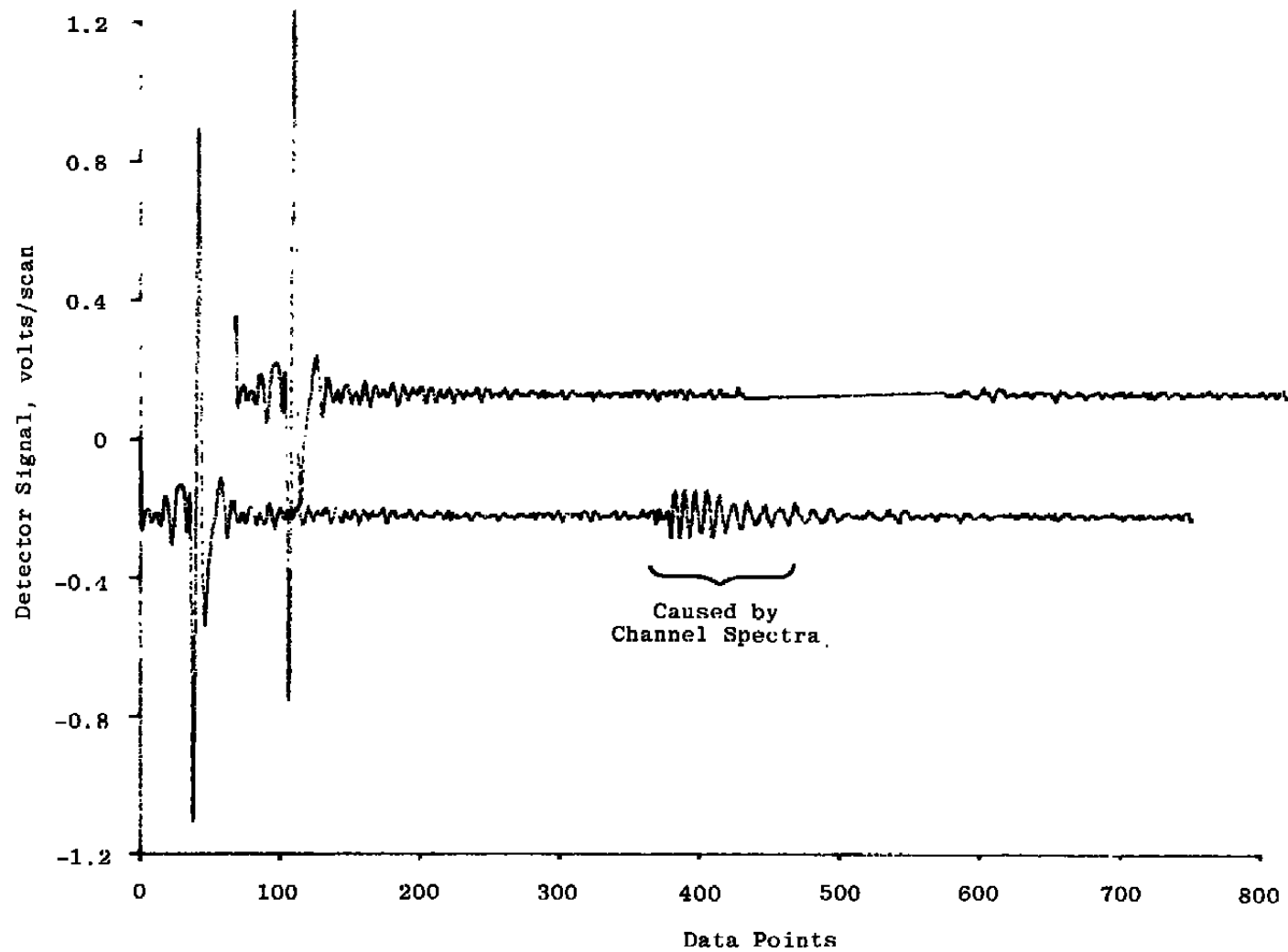


Figure 17. Interferogram displaying channel spectra symptom and IGRAM with that signal "fixed".

partially obscured by a thin wire at one location and by an interference filter in another. The experiment showed that the array elements viewing the wire produced an attenuated spectrum because of the lower temperature of the wire. The experiment showed that the filter eliminated, outside its passband, transmitted radiation from the source. The conclusion of numerous experiments of this sort was that spatial information was passed through the system, along with the spectral information, in a retrievable form. The other conclusion was the detector sensitivity was much lower than desirable and that the time required to scan a sufficient number of times to improve the signal-to-noise ratio adequately for high resolution work was prohibitive. Also, data reduction time (≈ 4 hr per data collection) was excessive with the current data system.

The transmission spectra in Fig. 18 are presented as an interesting set of low resolution data depicting the operation of the 1-D imager. In this experiment a spatially varying sample was suspended at the source image between mirrors M1 and M2 using the setup described in Fig. 12. The source viewed by the IRIFTS was therefore the back-illuminated sample. In Fig. 18 the source is depicted on the left and consists of an image of the blackbody above a plastic film backlit by the blackbody and finally a piece of aluminum blocking the blackbody radiation. The image of this source was transferred to the detector array so that the image of the three sections of the source fell on the detector elements shown in the center of the figure. Resultant transmission spectra from the three sources and the transitions between sections are shown on the right in the figure. The resolution is 16 cm^{-1} for these spectra. The CO_2 absorption at $4.3\text{ }\mu\text{m}$ and H_2O absorption around 2.7 and $6.3\text{ }\mu\text{m}$ are present in the form of apparent noise. The spectrum from the open sample shows near 100-percent transmission. The spectrum is noisy but is reasonably flat beyond $3.0\text{ }\mu\text{m}$. In the interval below $3.0\text{ }\mu\text{m}$, the signal is so noisy that it does not portray factual data. In the second trace from the top, where the detector is seeing the transition between sections, the spectrum appears to include less long-wavelength contributions and is in fact probably seeing mostly radiation which has passed through the plastic. In the third trace radiation has passed through the plastic and shows some reduction in transmission around $5\text{ }\mu\text{m}$ and near zero transmission from 5.5 to $10.5\text{ }\mu\text{m}$. The transmission losses are caused by absorption and scattering by the plastic. The fourth spectrum shows some obscuration by the aluminum, and the fifth shows only noise as the aluminum has totally blocked the radiation from the blackbody.

The final results from this system were obtained with a setup similar to that of Fig. 12. Three different sources were examined with IRIFTS, at a spectral resolution of 8 cm^{-1} . The spectra presented have had the channeled spectra effects reduced using the technique described earlier. These sources were flames produced by a propane torch, an acetylene torch, and an alcohol burner. They were chosen because they are similar to jet engine exhaust plumes (Appendix F contains a discussion of typical IR sources) and might be investigated with the

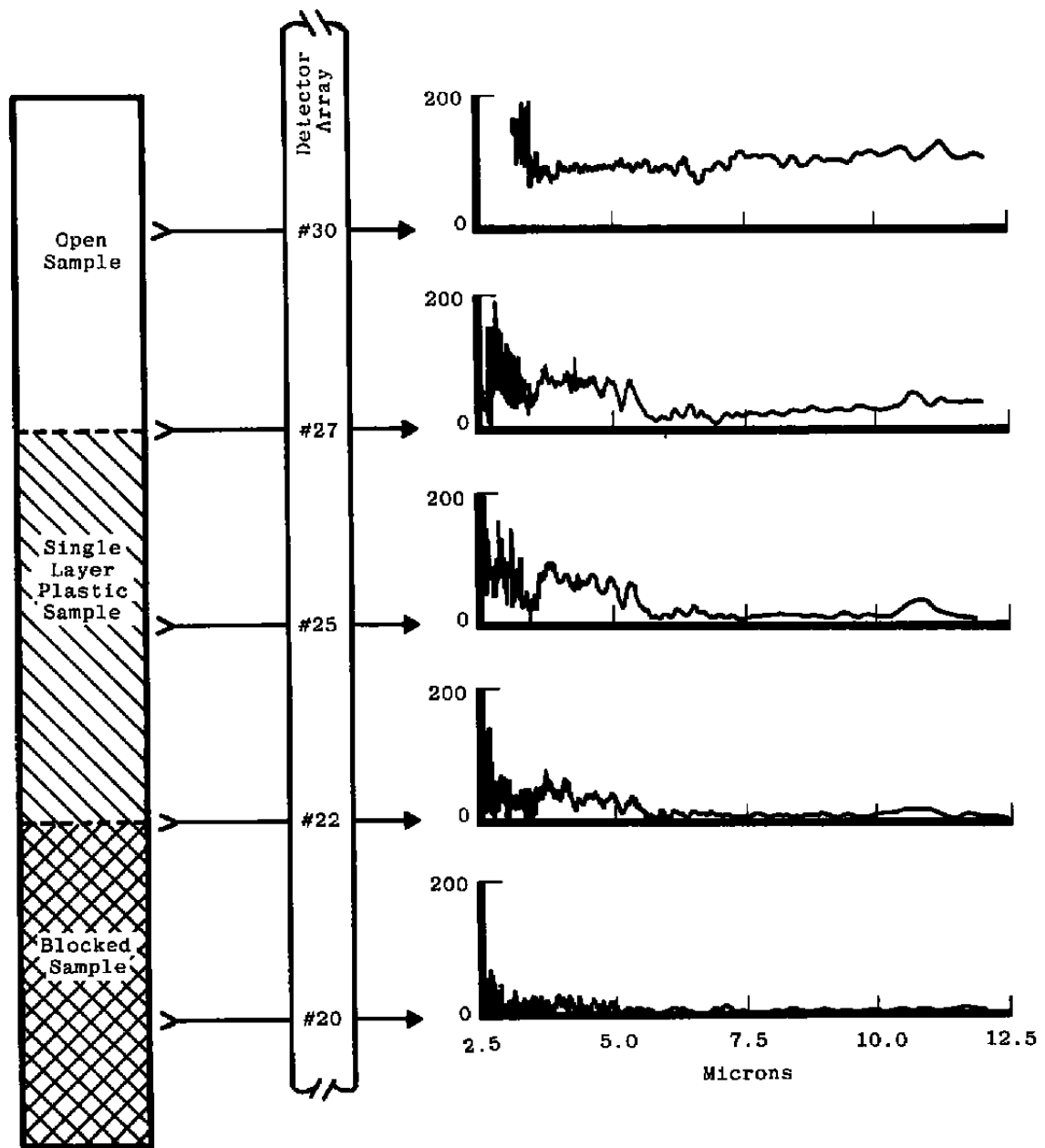


Figure 18. Transmission spectra from the one-dimensional imaging FTS.

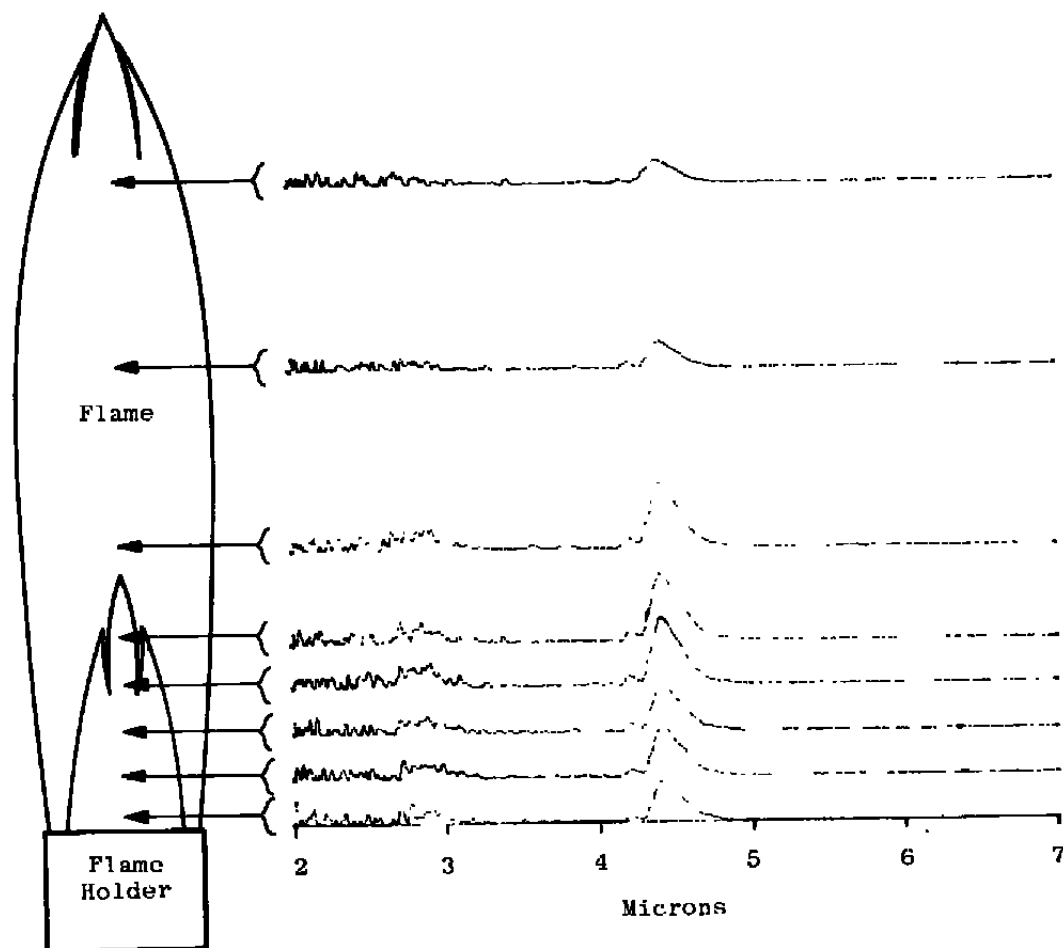
IRIFTS. Results of the propane torch experiment are shown in Fig. 19. Figure 19a is a summary of radiance spectra from points along the axis of the propane torch's flame, with an accompanying sketch of the flame to show where the radiance was measured. One of the spectra is expanded in Fig. 19b. The results show that the IR emission from the flame is chiefly from the 2.7- μm and the 4.3- μm H_2O and CO_2 bands. The conclusion can be drawn from these spectra that the combustion is nearly complete as the emission appears to be from hot H_2O and hot CO_2 rather than continuum emission as would occur if a significant amount of hot carbon particles was present.

A similar set of spectra is presented in Fig. 20 from an acetylene/air torch flame. These spectra are very similar to those in the previous figure. The major difference is that the emission from the acetylene/air flame is much less than that from the propane/air flame. In addition to the reduction in the magnitude of the spectra, these spectra are much noisier than the previous ones, especially in the shorter wavelengths where the instrument response is low.

A last set of spectra was obtained from an alcohol burner flame. These were similar to those from the other flames; however, the burner in this case did not use a pressurized gas and therefore produced a very unstable flame, and consequently noisy spectra were generated. These spectra are summarized in Fig. 21.

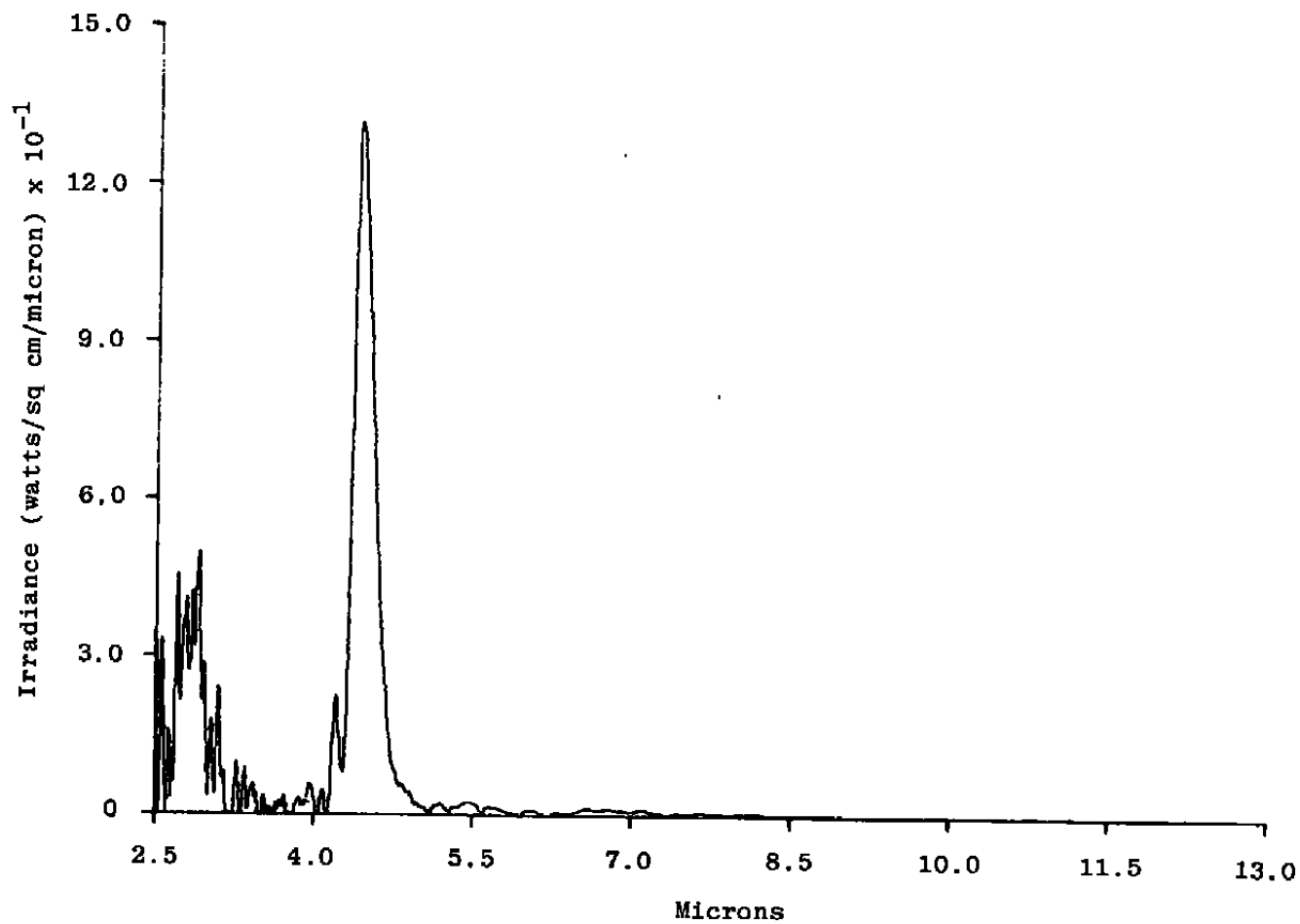
3.3 TWO-DIMENSIONAL IMAGING FTS

In the work which has been described, the concept of using multiple detectors within the half-angle obliquity limit to produce an instrument capable of simultaneously acquiring spectral and spatial information has been shown. The next step in the evolution of the imaging instrument was to increase the spatial resolution to two dimensions. The obvious approach was the incorporation of a two-dimensional (2-D) detector into the previous concept. However, the major considerations in this effort have been to operate within a small budget and to determine the limits to which currently available hardware can be taken. These considerations prevented further work using a 2-D detector array as their cost is prohibitive. An alternative approach was pursued briefly. This approach involved incorporating a scanning IR camera into an FTS. Some work was directed toward synchronizing the FTS mirror velocity with the field rate of the camera. Results of that effort were limited. The FTS modulator traveled so slowly that numerous vibration and velocity control problems were generated which were not solved. Therefore the effort served to prove the approach would not yield a reasonable instrument. The velocity control loop worked adequately with a scanning camera operating in the line scan mode where the mirror velocity was comparable with the velocity used in the previous approach, and limited results were obtained.

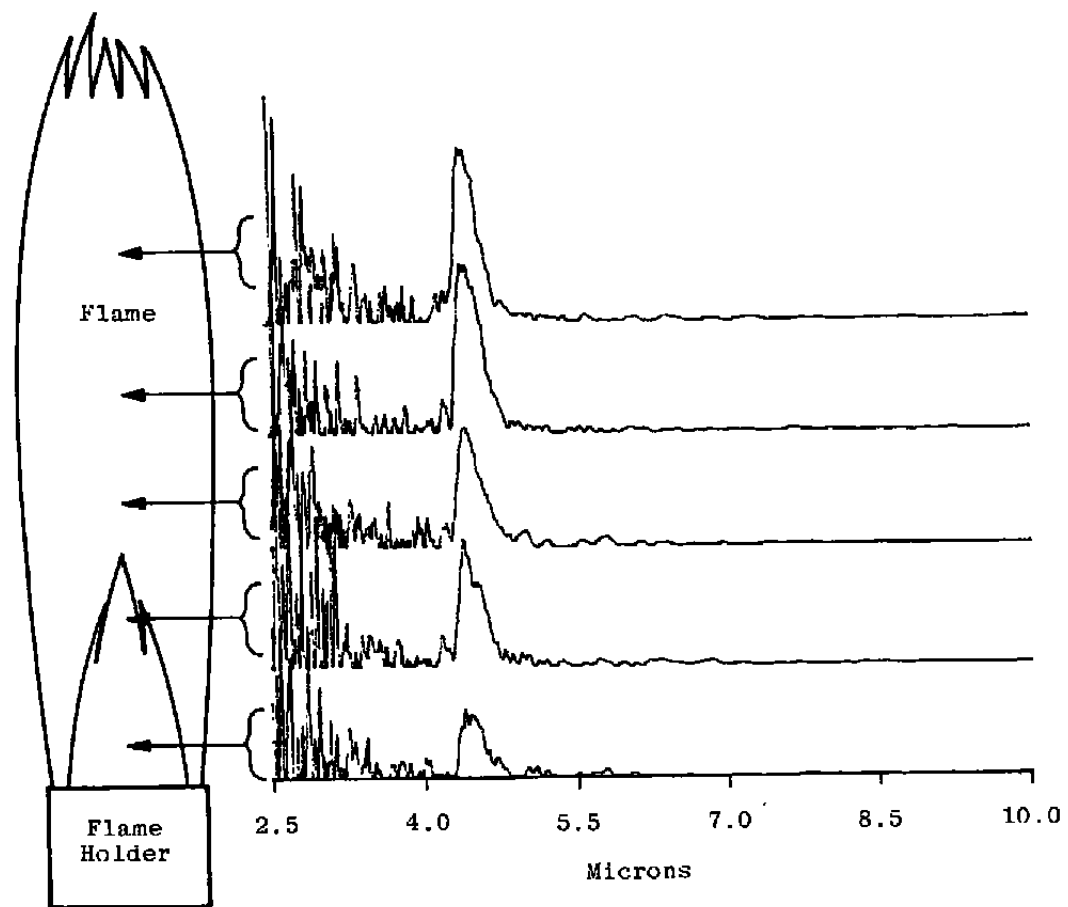


a. Low resolution summary

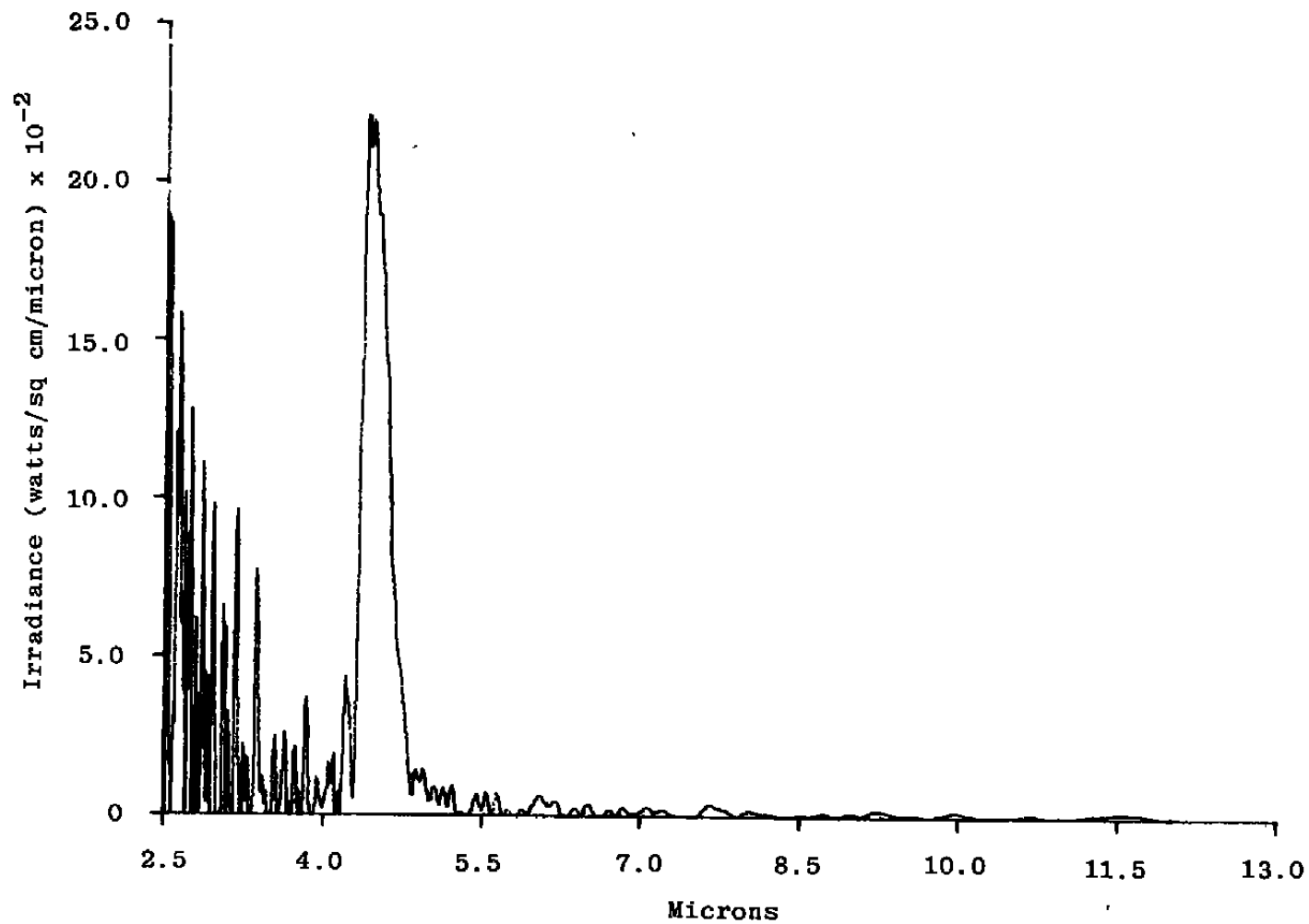
Figure 19. Emission spectra of a propane flame.



**b. Higher resolution spectrum
Figure 19. Concluded.**



a. Low resolution summary
Figure 20. Emission spectra of an acetylene flame.



b. Higher resolution spectrum
Figure 20. Concluded.

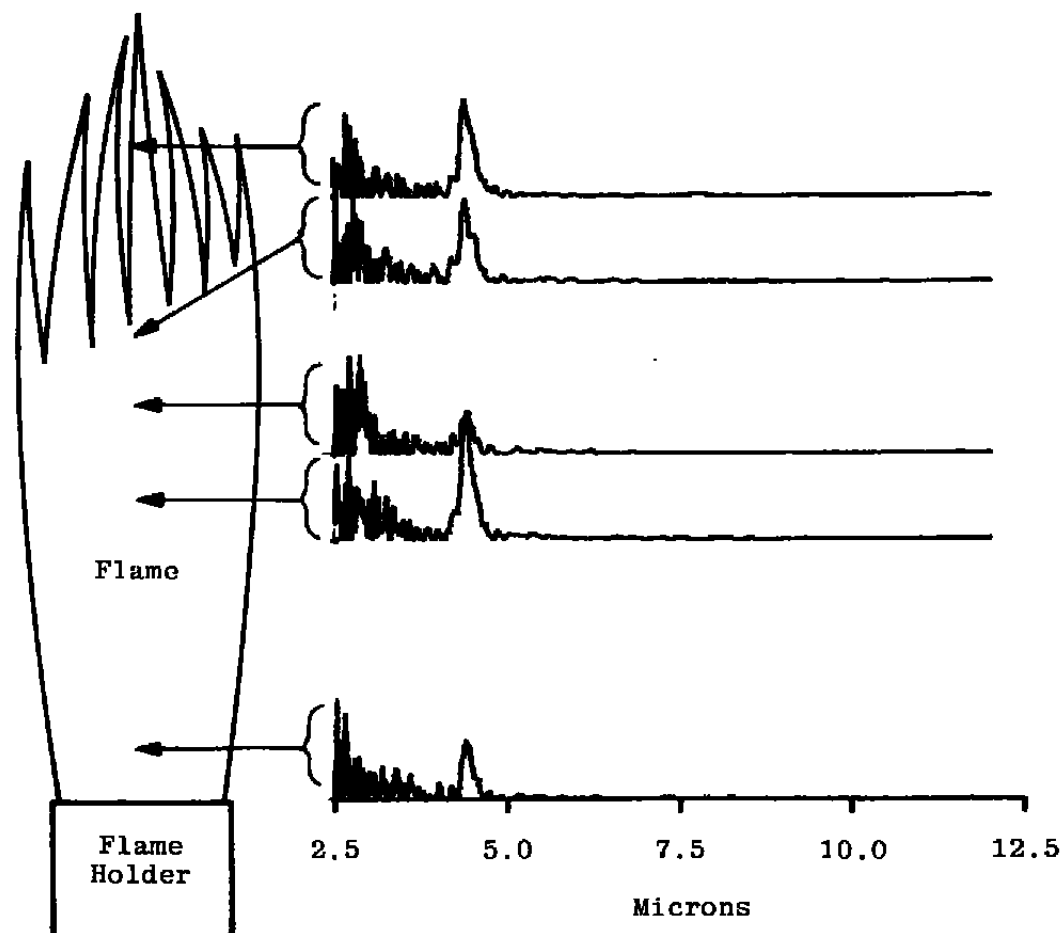


Figure 21. Emission spectra of an alcohol flame.

The experiments were conducted using the setup shown in Fig. 22 in which the IR camera looked through an interferometer. Controls were designed and prototyped to synchronize the laser sync signal with the line scan rate of the camera (2500 lines/sec). The timing and synchronization circuit, described in Ref. 37, was used to select the spatial position at which the camera signal would be digitized. A DEC® general purpose data acquisition and processing system was used for this set of experiments. Figure 23 is a sample of data acquired and processed by the system. Figure 23a shows a typical interferogram obtained with the system viewing a global source, and Fig. 23b is a Fourier transform of the data with no phase correction or apodization. The shape of the spectrum is similar to the spectral transmission of the IR camera.

4.0 CONCLUSIONS AND RECOMMENDATIONS

The goal of the effort was to show the feasibility of an Infrared Imaging Fourier Transform Spectrometer System and to develop a working prototype. The theory of the required components was reviewed, extended where necessary, and found to show the feasibility of the concept. The feasibility was experimentally confirmed with proof-of-principle experiments. Commercially available components were then acquired, interfaces were constructed and a 1-D imaging FTS system prototype assembled. Results have been presented showing the operation of the system.

The classical half-angle obliquity limit associated with the conventional FTS has been found to be inadequate to describe the response of the off-axis detectors of an imaging spectrometer. The limit which should be applied was derived [Eq. (35)] and found to permit use of detectors well beyond the generally accepted limit.

A prototype 1-D IRIFTS was assembled and evaluated. As was expected, because of the low sensitivity of the pyroelectric detector array, the system could be applied only to very "bright" sources. However, the prototype served to illustrate the principle and to point to areas that must be addressed in the construction of the next generation instrument. The main shortcomings can be overcome with an array of InSb detectors and a more potent data system.

The utility of the prototype 1-D imaging spectrometer was somewhat constrained because of the limited data processing capabilities of the system. The amount of time required to process and output final data was excessive (approximately 4 hr to process and plot data that were acquired in 2.5 sec). This problem is dramatically increased if a higher resolution (more detector elements) linear or 2-D array is considered. A high-resolution image coupled with high spectral resolution produces a tremendous volume of data. For a 100-line by 100-pixel image with 2-cm^{-1} spectral resolution, 81,920,000 words of data must be acquired and processed. For high temporal resolution, the data acquisition system throughput problem

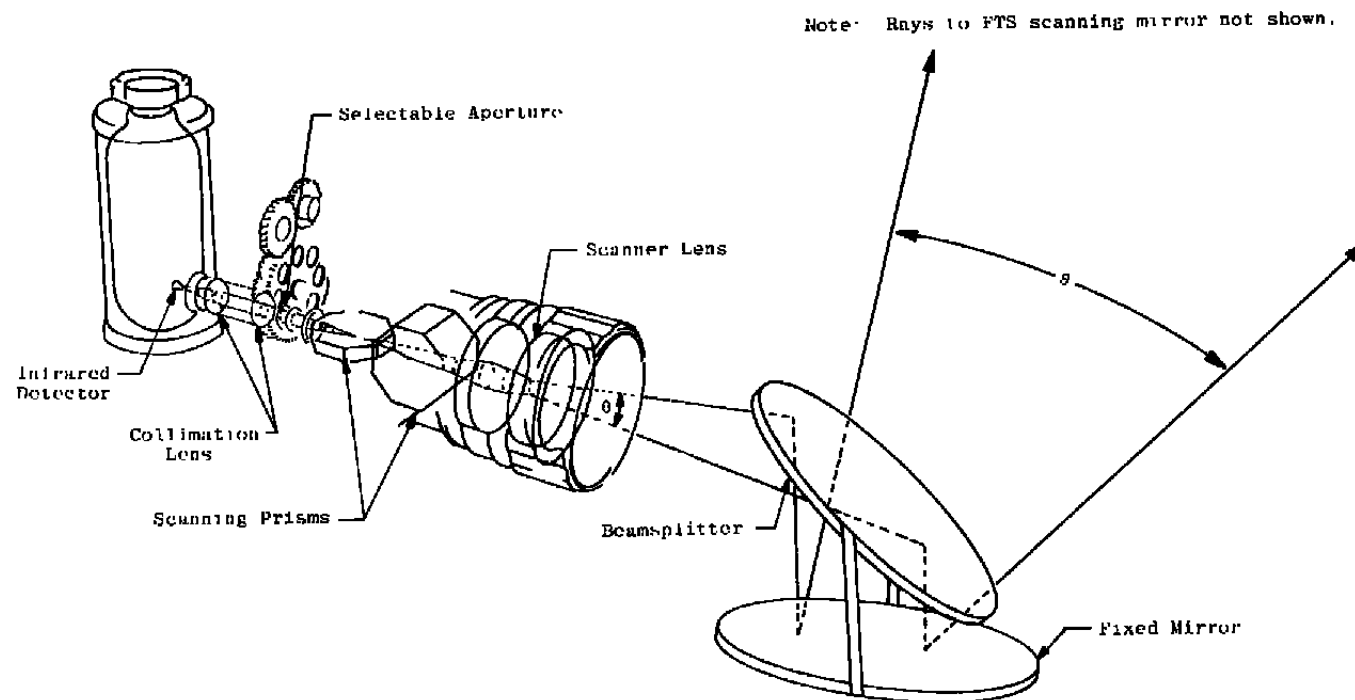
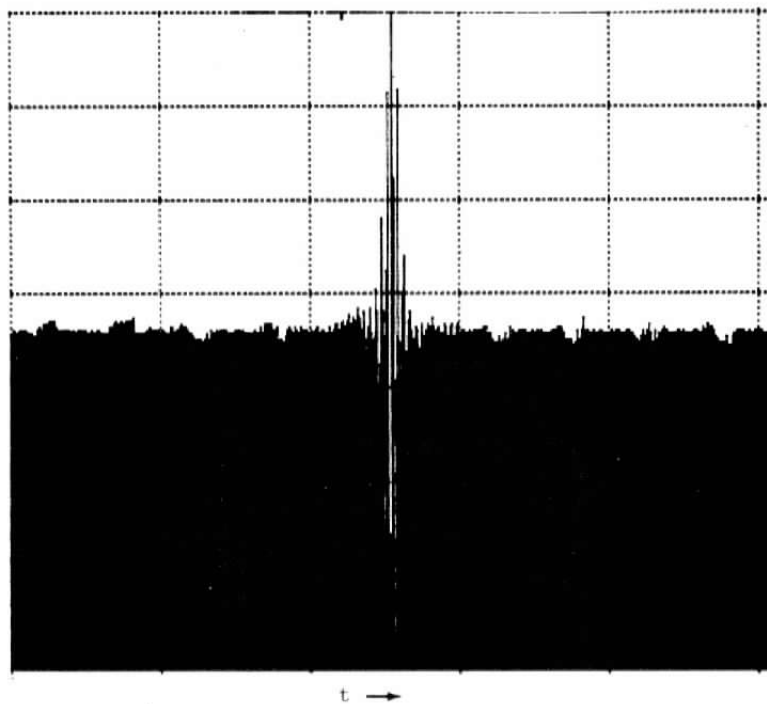
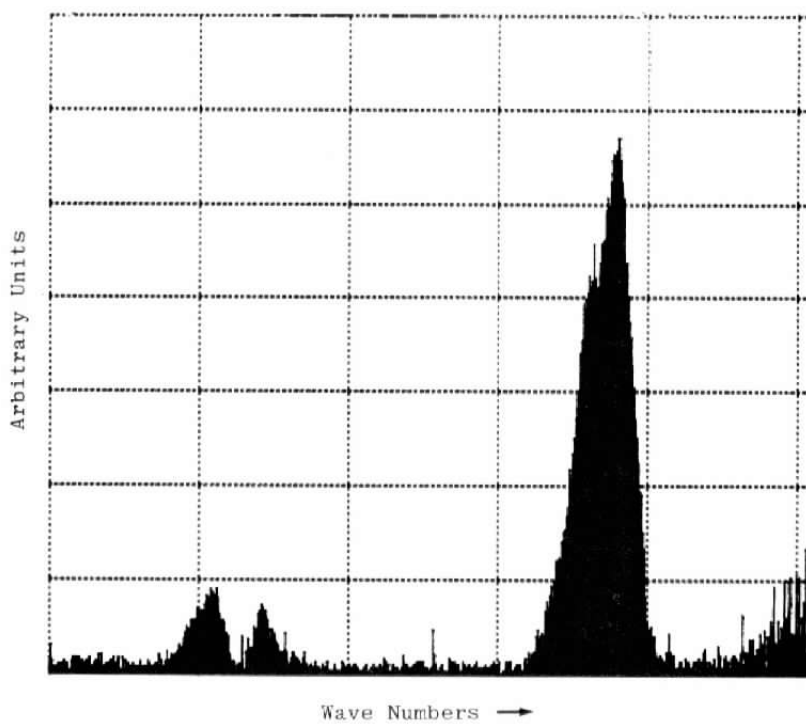


Figure 22. IR Camera/FTS system.



a. Interferogram



b. Spectrum

Figure 23. IR Camera/FTS 1-D system results.

is seen to be prohibitive. A compromise is necessary for any near-term developments (for example, spatial, spectral, or temporal resolution must be degraded) unless a substantially more sophisticated data system is used. Both data acquisition hardware and technique improvements could remove some of the compromises forced by the current system.

Potential applications of the Imaging FTS include:

1. Use of the IRIFTS in a sophisticated weapons system that could identify missile threat parameters such as missile type, missile fight path, and velocity from the spectral image examined at two times.
2. Use of the system to view both an unknown source and the background for background suppression.
3. Use of the system as a dual or multibeam instrument to provide simultaneous transmittances.
4. Use of the system as a "super-throughput" spectrometer in which the spectra derived from each of the detectors in the imaging system are combined to achieve superior signal-to-noise performance.
5. Use of the system concept in the visible, ultraviolet, and longer wavelength IR spectral regions.

Areas requiring additional effort include:

1. Development of more useful information displays from an IRIFTS. The multidimensional nature of the information (spatially, spectrally, and temporally resolved radiances) is very difficult to display and interpret.
2. Development of more efficient on-chip detector electronics and improvements in the manner in which detector arrays can transmit information to a data system. Separate detectors, preamplifiers, and multiple data system channels are the most practical means of achieving system requirements today, but are prohibitively cumbersome. Smart arrays currently do not generate information containing all required data from which spectral images may be extracted.
3. Further investigation into the half-angle obliquity limits would be desirable. The half-angle obliquity limit derived in this study used the constraint that

the maximum phase difference acceptable by a detector is π . Another constraint might be more appropriate.

4. Investigate the use of dc-coupled electronics to permit the use of both the ac- and dc-components of the signal derived from the imager to enhance the imaging aspect of the instrument.

From the beginning of this effort, different concepts for achieving an imaging spectrometer have been considered. The conclusion at the end of this study is essentially the same as at its inception. The most promising concept appears to be an FTS using a focal plane array of detectors. A further conclusion is that imaging spectrometry is both a viable possibility and a technical challenge.

REFERENCES

1. Born, Max and Wolf, Emil. *Principles of Optics*. Pergamon Press, Oxford New York, 1975 (Fifth Edition).
2. Bell, Robert John. *Introductory Fourier Transform Spectroscopy*. Academic Press, New York, 1972.
3. Mertz, Lawrence. *Transformations in Optics*. John Wiley and Sons, New York, 1965.
4. Martin, A. E. *Infrared Interferometric Spectrometers*. Elsevier Scientific Publishing Company, The Netherlands, 1980.
5. Hecht, E. and Zajac, A.. *Optics*. Addison-Wesley Publishing Company, Reading, Massachusetts, 1974.
6. Vanasse, G. A. "Fourier Spectroscopy A Critical Review." AFCRL Technical Report 74-0093, December 1973.
7. Steel, W. H. *Interferometry*. Cambridge University Press, London, Great Britian, 1967.
8. Huppi, R. J., Shipley, R. B. and Huppi, E. R. "Balloonbourne Fourier Spectrometer Using a Focal Plane Detector Array." *Proceedings of SPIE*. Vol. 191, 1979, pp. 191-204.
9. Yap, B. K., Blumberg, A. M. and Murphy, R. E. "Off-Axis Effects In A Mosaic Michelson Interferometer." *Applied Optics*, Vol. 21, No. 22, November 1982, pp. 4176-4182.

10. Johnson, N. J. E. "Spectral Imaging with the Michelson Interferometer." *Proceeding of SPIE*. Vol. 226, Washington, D. C., April 1980, pp. 2-9.
11. Strobel, Howard A. *Chemical Instrumentation: A Systematic Approach To Instrumentation Analysis*. Addison-Wesley Publishing Co., Reading, Massachusetts, 1973.
12. Strong, John. *Concepts of Classical Optics*. W. H. Freeman Co., San Francisco, 1958.
13. Smith, Warren J. *Modern Optical Engineering*. McGraw Hill Book Company, New York, 1966.
14. Sanderson, R. B. "Fourier Spectroscopy." *Molecular Spectroscopy Modern Research*. Academic Press, New York, 1972.
15. Steel, W. H. "Interferometers without Collimation for Fourier Spectroscopy." *Journal of the Optical Society of America*, Vol. 54, No. 2, February 1964, pp. 151-156.
16. Vanasse, G. A., ed. *Spectrometric Techniques, Vol. 1*. Academic Press, New York, 1977.
17. Atherton, P. D. et al. "Tunable Fabry-Perot Filters." *Optical Engineering*, Vol. 20, No. 6, November/December 1981, pp. 806-814.
18. Goodman, Joseph W. *Introduction to Fourier Optics*. McGraw Hill Book Company, San Francisco, 1968.
19. deHaseth, J. A. "Stability of Rapid Scanning Interferometer." *Applied Spectroscopy*, Vol. 36, No. 5, 1982, pp. 544-552.
20. Esplin, R. W. et al. "Tuneable Optical Filter Using an Interferometer for Selective Modulation." *Proceedings of SPIE*. Vol. 268, Los Angeles, California, February 1981, pp. 129-139.
21. Schwider, J., et. al. "Digital Wave-front Measuring Interferometry: Some Systematic Error Sources." *Applied Optics*, Vol. 22, No. 21, November 1983, pp. 3421-3432.
22. Vanasse, G. A., Stair, A. T., and Baker, D. J. eds. *Aspen International Conference on Fourier Spectroscopy, 1970*. AFCRL Technical Report 71-0019, January 1971.

23. Mertz, M. V., Shukla, R. K. and Shukla, R. P., "Michelson Interferometer with Beam Divider and Compensating Plate Having Slight Wedge Angles." *Optical Engineering*, Vol. 22, No. 5, September/October 1983, pp. 615-618.
24. Tescher, A. G. "Beam Splitter Optimization for Fourier Spectroscopy." *Aspen International Conference on Fourier Spectroscopy, March 16-20, 1970*. AFCRL Technical Report 71-0019, January 1971, pp. 225-230.
25. Lindsay, R. and Margenau, H. *Foundations of Physics*. Dover Publications, New York, 1963.
26. Jackson, J. D. *Classical Electrodynamics*. John Wiley and Sons, New York, May 1962.
27. Lowenstein, E. V. "Fourier Spectroscopy: An Introduction." *Aspen International Conference on Fourier Spectroscopy, March 16-20, 1970*. AFCRL Technical Report 71-0019, January 1971, pp. 3-17.
28. Sakai, H., Vanasse, G. A. and Forman, M. L. "Spectral Recovery in Fourier Spectroscopy." *Journal of the Optical Society of America*, Vol. 58, No. 1, January 1968, pp. 84-90.
29. Jenkins, F. A. and H. White. *Fundamentals of Optics*. McGraw Hill Book Company, New York, 1957.
30. Saperstein, D. D. "Resolution Limit of an IR Interferometer." *Applied Spectroscopy*, Vol. 37, No. 1, 1983, pp. 44-46.
31. Anderson, C. A. and Mattson, D. R. "Phase Correction Techniques in Fourier Transform Infrared." *Proceedings of SPIE*. Vol. 191, 1979.
32. Forman, M. L., Steel, W., and Vanasse, G. "Correction of Asymmetric Interferograms Obtained in Fourier Spectroscopy." *Journal of the Optical Society of America*, Vol. 56, No. 1, January 1966, pp. 59-63.
33. Giancaspro, C. and Comisarow, M. B. "Exact Interpolation of Fourier Transform Spectra." *Applied Spectroscopy*, Vol. 37, No. 2, 1983, pp. 153-166.
34. Kauppinen, J. K. et al. "Smoothing of Spectral Data in the Fourier Domain." *Applied Optics*, Vol. 21, No. 10, May 1982, pp. 1866-1872.

35. Sanderson, R. B. and Bell, E. E. "Multiplicative Correction of Phase Errors." *Applied Optics*, Vol. 12, No. 2, February 1973, pp. 266-270.
36. Bracewell, R. N. *The Fourier Transform and Its Applications*. McGraw Hill Book Company, New York, 1965.
37. Pender, C. W. and Roux, J. "Microcomputer System for Controlling an Infrared Scanning Camera." *Proceedings of SPIE*. Vol. 230, Washington, D. C., April 1980, pp. 120-129.
38. Hudson, R. D. and Hudson, J. W., eds. *Infrared Detectors*. Dowden, Hutchinson and Ross Inc., Distributed by Halsted Press a division of John Wiley and Sons Inc., 1975.
39. Putley, E. H. "New Infrared Detectors." *Advances in Geophysics, Part 5, Vol. 14*. Edited by H. E. Landsberg and J. Van Mieghem, Academic Press, New York, 1970.
40. "Cadmium-Telluride Detector Has Highest Sensitivity Yet." *Electronic Design*, Vol 12, June 1974.
41. Martineau, R., Robillard, G., and Wong, T. "HgCdTe: Number One in Night Vision." *Optical Spectra*, Vol. 13, July 1979, pp. 45-48.
42. Doyle, W. M., McIntosh, B. C., and Geist, Jon. "Implementation of a System of Optical Calibration Based on Pyroelectric Radiometry." *Optical Engineering*, Vol. 15, No. 6, November/December, 1976, pp. 541-548.
43. Pankratov, N. A. and Korotkov, V. P. "Cryogenic Semiconductor Bolometers." *Optical Technology*, Vol. 41, No. 4, February 1974.
44. Jones, R. C. "The General Theory of Bolometer Performance." *Journal of the Optical Society of America*, Vol. 43, No. 1, January 1953, pp. 1-14.
45. Roundy, C. B. "Application Note An-10." Spiricon, Logan, Utah.
46. Wang, S. *Solid State Electronics*. McGraw Hill Book Company, New York, 1966.
47. Pradhan, M. M. and Garg, R. K. "Pyroelectric Null Detector for Absolute Radiometry." *Applied Optics*. Vol. 21, No. 24, December 1982, pp. 4456-4458.

48. Huang, C. "Infrared Thermal Detectors: A Comparison." *Optical Spectra*, Vol. 12, September 1978, pp. 47-50.
49. Singer, B. "Pyroelectric Vidicons - The IR Imaging Dark Horse." *Electro-Optical Systems Design*, July 1975.
50. Watton, R. et al. "The Pyroelectric/CCD Focal Plane Hybrid: Analysis and Design for Direct Charge Injection." *Infrared Physics*, Vol. 22, No. 5, 1982, pp. 259-275.
51. Szymanski, H. A. *IR Theory and Practice of Infrared Spectroscopy*. Plenum Press, New York, 1964.
52. Chappel, A., ed. *Optoelectronics: Theory and Practice*. McGraw Hill Book Company, New York, 1978.
53. Wolfe, W. L. and Zissis, G. J., eds. *The Infrared Handbook*. Office of Naval Research Department of the Navy, Arlington, Virginia, US Government Printing Office, 1978.
54. Wolfe, W. L., ed. *Handbook of Military Infrared Technology*. Naval Research Laboratory, US Government Printing Office, 1965.
55. Dow, R. B. *Fundamental of Advanced Missiles*. John Wiley and Sons, New York, 1958.
56. Ludwig, C. B. et al. *Handbook of Infrared Radiation from Combustion Gases*. Editors R. Gonlard and J. A. L. Thomson, NASA SP-3080.
57. Siegel, R. and Howell, John R. *Thermal Radiation Heat Transfer*. Hemisphere Publisher Corporation, Washington, 1981 (Second Edition).
58. Friberg, A. T. "Effects of Coherence in Radiometry." *Optical Engineering*, Vol. 21, No. 5, September/October 1982, pp. 927-936.
59. Beran, M. J. and Parrent, G. B. *Theory of Partial Coherence*. Prentice-Hall, Englewood Cliffs, New Jersey, 1964.

APPENDIX A

IR BEAMSPLITTER

As the name implies, the beamsplitter divides incident radiation into two components. The beamsplitters used for the 2- to 15- μm region consist of partially reflecting films supported by transparent substrates and covered by similar transparent compensating plates. Figure A-1 illustrates a beamsplitter and an incident ray of light. In Fig. A-1 the angles of the illustrated rays have been calculated from Snell's law of refraction. Fresnel's formulas describe the transmission and reflection coefficients of the fields symbolized by the rays in the figure. Fresnel's formulas for the amplitude reflection and transmission coefficients of reflected and transmitted fields are

$$t_{\text{par}} = \frac{2 n_i \cos(\theta_i) A_{\text{par}}}{n_i \cos(\theta_i) + n_t \cos(\theta_t)} \quad (\text{A-1})$$

$$t_{\text{per}} = \frac{2 n_i \cos(\theta_i) A_{\text{per}}}{n_i \cos(\theta_i) + n_t \cos(\theta_t)} \quad (\text{A-2})$$

$$r_{\text{par}} = \frac{n_t \cos(\theta_t) - n_i \cos(\theta_i)}{n_i \cos(\theta_i) + n_t \cos(\theta_t)} A_{\text{par}} \quad (\text{A-3})$$

$$r_{\text{per}} = \frac{n_t \cos(\theta_t) - n_i \cos(\theta_i)}{n_i \cos(\theta_i) + n_t \cos(\theta_t)} A_{\text{per}} \quad (\text{A-4})$$

where n_i and n_t are the indices of refraction of the materials, and the angles are as shown in the figure. The ratios of reflected and transmitted to incident energy fluxes, the transmissivity, τ , and the reflectivity, ρ , are

$$\tau_{\text{per}} = \frac{n_t \cos(\theta_t) t_{\text{per}}^2}{n_i \cos(\theta_i)} \quad (\text{A-5})$$

$$\tau_{\text{par}} = \frac{n_t \cos(\theta_t) t_{\text{par}}^2}{n_i \cos(\theta_i)} \quad (\text{A-6})$$

$$\rho_{\text{per}} = r_{\text{per}}^2 \quad (\text{A-7})$$

$$\rho_{\text{par}} = r_{\text{par}}^2 \quad (\text{A-8})$$

A beamsplitter used in this study, a germanium (Ge) film on a potassium bromide (KBr) substrate with a KBr compensating plate, is used as an example. At the first interface the optical properties, in the near infrared, are $n_i = 1.0$, $n_t = 1.5$, $\theta_i = 45^\circ$ and by Snell's

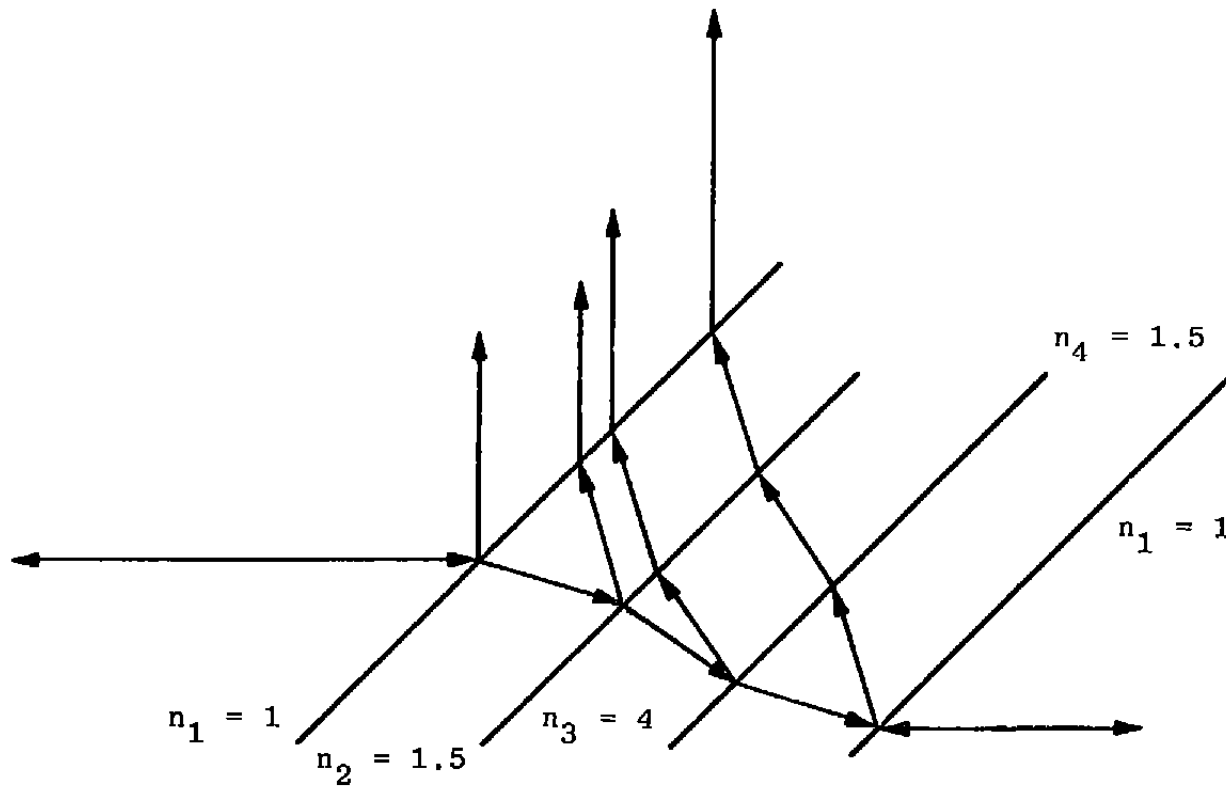


Figure A-1. Beamsplitter cross-section.

law $\theta_i = 28$ deg. For the primary ray, the calculated transmissivities and reflectivities are calculated to be

$$\tau_{\text{par}} = 0.99, \rho_{\text{par}} = 0.01$$

and

$$\tau_{\text{per}} = 0.91, \rho_{\text{per}} = 0.09$$

The addition of a secondary ray, because of reflection at the next KBr/Ge interface, increases the reflected component by an amount dependent upon the reflectivity at that interface. The addition influences the transmissivities and reflectivities by about 10 percent. At the second KBr/Ge interface, where $n_i = 1.5$, $n_t = 4(1 + 0.1i)$, and $\theta_i = 28$ deg, the division of energy by the germanium layer is a more significant problem than encountered at the first interface. Here several factors, including the thickness of the germanium film and the fact that the film is a borderline metal with a noticeable absorption coefficient, make the treatment more difficult. From Born and Wolf's treatment (Ref. 1) of absorbing films on transparent substrates an expression is found which relates the reflectivities and transmissivities of the beamsplitter as functions of the indices of refraction of the involved materials, the angles, and polarizations of incident radiation and the thickness of the metalloid film. The expression for the reflectivity is

$$\rho = \frac{\beta^2 e^{2\gamma n} + \beta^2 e^{-2\gamma n} + 2\beta^2 \cos(2\gamma n)}{e^{2\gamma n} + 2\beta^2 e^{-2\gamma n} + 2\beta^2 \cos(2\gamma n)} \quad (\text{A-9})$$

where

$$2u^2 = n_t^2(1 - k_t^2) - n_i^2 \sin^2(\theta_i) + \{[n_t^2(1 - k_t^2) - n_i^2 \sin^2(\theta_i)]^2 + 4n_t^4 k_t^2\}^{1/2}$$

$$2v^2 = -n_t^2(1 - k_t^2) + n_i^2 \sin^2(\theta_i) + \{[n_t^2(1 - k_t^2) - n_i^2 \sin^2(\theta_i)]^2 + 4n_t^4 k_t^2\}^{1/2}$$

$$n = 2\pi/\lambda$$

and for an electric vector parallel to the plane of incidence

$$\beta^2 = \frac{[n_t^2(1 - k_t^2)\cos(\theta_i) - n_i u]^2 + [2n_t^2 k_t \cos(\theta_i) - n_i v]^2}{n_t^2(1 - k_t^2)\cos(\theta_i) + n_i u]^2 + [2n_t^2 k_t \cos(\theta_i) + n_i v]^2}$$

and for an electric vector perpendicular to the plane of incidence

$$\beta^2 = \frac{[n_i \cos \theta_i - u]^2 + v^2}{[n_i \cos \theta_i + u]^2 + v^2}$$

where the indices and angles are as shown in Fig. A-1, l is the thickness of the film, and λ is the wavelength at which the calculation is valid. Figure A-2 shows the effect of different thickness Ge films in the near IR range.

Figure A-2 plots an average, $(R_{\text{per}} + R_{\text{par}})/2$, reflectivity since unpolarized sources are the subject of this study. The results show that a beamsplitter less than about $0.02 \mu\text{m}$ thick is reasonably uniform across the spectral range of interest for this study. Although the reflectivity is not truly 50 percent, it is reasonable. The final division of energy occurs at the final KBr/air interface, which is like the first interface considered except the direction of energy flow is reversed. Again the transmitted component dominates. At this interface the reflected component returning through the entire beamsplitter assembly is negligible. A similar exercise with a Ge/KBr beamsplitter has also been done by Roland and Steele (Ref. 15) and has been reported by Bell (Ref. 2). Their results support the conclusion that a film of germanium of appropriate thickness on a KBr substrate produces a beamsplitter of reasonable efficiency in the near IR region of the spectrum.

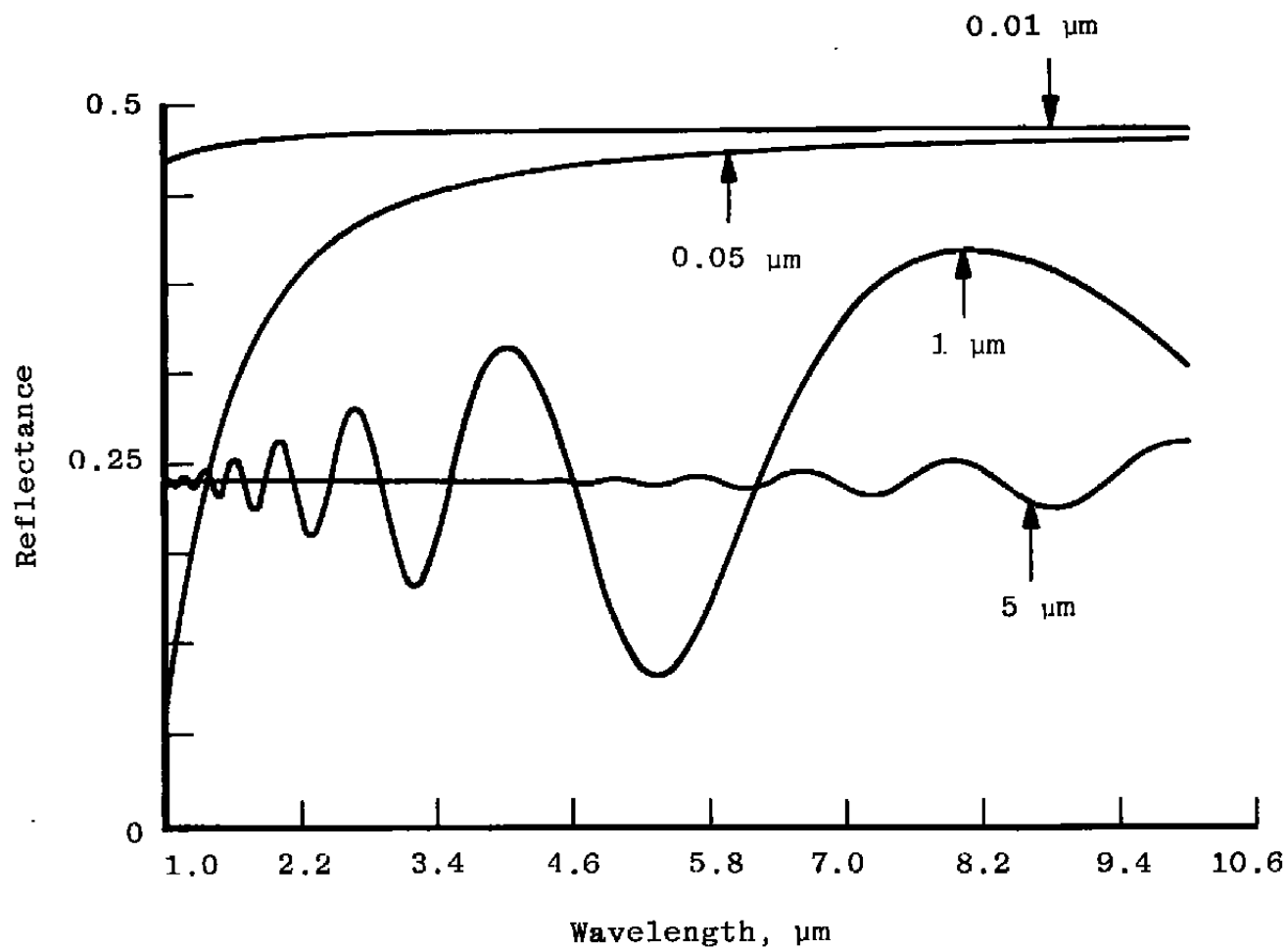


Figure A-2. Reflectivity of Ge/KBr interface for various thicknesses of Ge.

APPENDIX B

RADIATION TRANSDUCER

In an infrared measurement system, a sensor comprised of optical components, detector (or radiation transducer), and associated signal and control electronics, generates a signal that is passed to a data handling system for analysis. During an infrared measurement, a portion of the radiant flux leaving a source is collected and directed to the field stop of the optical system. Following or coincident with the field stop is the radiation transducer. The function of the radiation transducer is to convert the irradiance incident upon it to a voltage, a current, a change in conductivity, etc. The radiation transducer sometimes includes the detector and signal conditioning elements necessary to convert the output of the detector to voltages of appropriate levels to be handled by the data acquisition system.

The radiation transducer technology is especially interesting at this point in time because of the rapid developments going on in both the detector and electronics areas. The past decade has seen the acceptance of integrated analog and digital electronics into the transducer systems. During the same period the detector industry has progressed in capabilities to the point that mosaics of literally hundreds of thousands of individual detectors can be manufactured in a single package. Hybrid and integrated systems that incorporate detector, preamplifier, and signal processing in a single package are rapidly becoming commercially available.

In discussing radiation transducers, first the unique nomenclature of the detectors and then the detector types in use will be discussed with specific examples of detectors used in this study. The references cite numerous articles that describe the various detectors and systems mentioned in the report (Refs. 38 through 52).

Numerous figures of merit, operating characteristics, and other constraints must be considered when matching detectors and applications. The most often used figures of merit for infrared detectors are the responsivity, the noise equivalent power, and the detectivity. Also of extreme importance in many applications is the operating temperature of the detector since the requirement for cryogenic cooling can sometimes not be met. Additional factors that also must be considered are spectral response, size, and cost.

The responsivity, R , is the ratio between the root-mean-squared (rms) signal voltage (or current) and the rms incident signal power. Spectral responsivity refers to a monochromatic input signal, and blackbody responsivity refers to an input signal having a blackbody spectrum. Typical units for responsivity are volts or amperes per watt.

The noise equivalent power, NEP, is the value of incident rms signal power for a given radiation source, bandwidth, and chopping frequency required to produce an rms signal-to-noise ratio of unity. The NEP is a measure of the minimum power that can be detected. The NEP is given by

$$\text{NEP} = E_d A N / (V \sqrt{f}) \quad (\text{B-1})$$

where E_d is the irradiance on the detector, A is the detector surface area, V is the voltage developed, N is the noise voltage developed by the detector, and f is the noise bandwidth used in measuring N .

Since most detectors are spectrally selective, the radiation source must be specified. Usually a 500-K blackbody or a particular wavelength source is specified. Further, since many detectors are used with a mechanical chopper to permit the use of phase sensitive detection, for extraction of a signal from noise, it is customary to specify the chopping frequency used for the NEP measurement. For uniformity, NEP values are specified for an equivalent noise bandwidth of 1 Hz.

The detectivity, D , is simply the reciprocal of NEP. A more commonly used expression is the dee-star, D^* , of the detector. D^* is the S/N ratio at a given source temperature and chopping frequency with an amplifier bandwidth of 1.0 Hz for a 1.0-cm² detector receiving one watt of radiant power. It is therefore a normalization of the reciprocal of NEP.

The detector time constant, τ , is a measure of the speed of response of a detector. This time constant indicates the responsivity of the detector as a function of modulation frequency. Knowledge of this parameter is necessary to choose an appropriate chopping rate or the applicability of a detector for a rapidly transient source. The time constant is generally defined as

$$\tau = \{2\pi f_c\}^{-1}$$

where f_c is the signal frequency at which the responsivity has dropped to 70.7 percent of its maximum value. The detector responsivity is generally

$$R(f) = R_0 \{1 + 4\pi^2 f^2 \tau^2\}^{-1/2} \quad (\text{B-2})$$

where $R(f)$ is the detector responsivity at f Hz, R_0 is the responsivity at low frequency, and f is the modulation frequency.

A wide variety of infrared detectors is in use. The most common are photoelectric detectors and thermal detectors. The thermal detectors include bolometric, thermovoltaic, pyroelectric, and thermopneumatic types. The photoelectric detectors include photovoltaic, photoconductive, photomagnetic, and photoemissive types. Of the different types, the most unusual is probably the thermopneumatic Golay detector. The Golay detector consists of a gas cell into which radiation is allowed to enter. The radiation heats the gas, deforms the cell, and causes motion of an attached mirror or alters the character of an integrated capacitor. The detectors used in this study are the pyroelectric thermal type, the photovoltaic indium antimonide (InSb), and the photoconductive mercury cadmium telluride types.

In thermal detectors the responsive element is sensitive to changes in its temperature, which are caused by fluctuations in the irradiance. In the bolometric type (for example, the thermistor), the electrical conductivity is the temperature - related variable. In the thermovoltaic detector (for example, the thermocouple), a temperature fluctuation of a junction of dissimilar metals results in a generated voltage. With the pyroelectric detector, a change in the temperature of the sensitive element results in the generation of a current proportional to the rate of change of the temperature.

The pyroelectric effect is based on the property of some noncentrosymmetrical crystals (also called ferroelectric crystals) of exhibiting an internal electric field along a certain crystal axis. A number of materials, for example, triglycene sulfate (TGS) or lithium tantalate (LiTaO_3), display this response. In these crystals the electric field is produced by the polarization of electric dipole moments. Polarization of the dipoles is dependent upon the lattice spacing within the crystal, which is in turn proportional to the crystal temperature. These crystals are insulating materials, and electrodes may be attached to the crystal surfaces normal to the axis of polarization so that an electric charge will result from the electric field. The electrodes make the detector essentially a capacitor. Then if the electric field is perturbed by a crystal temperature fluctuation, an observable current can be generated in an external circuit. The current is given by

$$i(t) = F(T) A \, dT/dt \quad (\text{B-3})$$

where $F(T)$ is the pyroelectric coefficient at temperature T , A is the electrode surface area, and dT/dt is the rate of temperature change. Since the current varies with changes in temperature, the detector is insensitive to steady irradiance and responds only if the irradiance fluctuates.

Since the detector response is based on its thermal condition, a judicious choice of detector size, material, and substrate is required. As with any thermal detector, the response time depends in part on the heat-transfer rate. The heat-transfer balance is of the form

$$Q = A\sigma(T_2^4 - T_1^4) + AK(T_2 - T_1)/l + cAl(dT/dt) \quad (B-4)$$

where Q is the radiation power being absorbed by the detector, the first term on the right represents heat losses caused by radiation, the second term is the conduction loss, and the last term reflects the ability of the detector to store heat according to its heat capacity. In Eq. (B-4), A is area, σ is the Stefan-Boltzmann constant, K is the thermal conductance, l is the detector thickness, c is the specific heat of the detector, and t is time. Generally it is assumed that the radiation loss is insignificant, and the expression is simplified. Then the equation is solved to obtain the expression for the temperature of the detector

$$T(t) = \text{constant} + \text{constant} \cdot \exp\{-Kt/(cAl)\} \quad (B-5)$$

so that the thermal time constant, τ , is cAl/K . This thermal behavior will influence the frequency response of the detector unless the irradiance fluctuations are significantly faster than the time constant. For the pyroelectric detector, the detector current response at low frequencies is

$$R_{ilo} \propto \pi F(\tau)A/k \quad (B-6)$$

while at higher frequencies

$$R_{ihi} \propto F(\tau)/c1 \quad (B-7)$$

The high frequency response is valid throughout this study.

The photoelectric (or quantum) detectors are based on the internal or external photoelectric effect. The internal photoelectric effect involves the excitation of electrons to higher energy levels in the conduction band by the irradiance on the detector. Electron hole pairs are generated, either near a semiconductor p-n junction or inside a homogeneous semiconductor, which establish a voltage across the junction or change the conductivity of the semiconductor. The external photoelectric effect is more dramatic and results in the escape of "free" electrons from the irradiated substance. The irradiated substance absorbs sufficient energy to excite electrons on the photosensitive material sufficiently to liberate them from the material. Most quantum detectors used in the infrared are based on the internal effect because of low energies associated with low-frequency photons. The two quantum detectors used in this study are the photovoltaic InSb and the photoconductive HgCdTe types.

The InSb detector operating at 77 K acts as a diode that generates a current proportional to the number of photons falling on it. A general expression for the conversion of arriving photons to a photocurrent, i , is

$$i \propto QE q N \quad (B-8)$$

where QE is the fraction of photons absorbed (quantum efficiency), q is the electron charge, and N is the average number of incident photons arriving per unit time. This current occurs when photons with sufficient energy to photoexcite electrons from the valence band to the conductive band in the detector material fall on it. The photoexcitation can occur only when the energy associated with incident photons equal or exceed the band gap of the material. If the photoexcitation process takes place, electron-hole pairs are generated either near the p-n junction or in the bulk region where they diffuse to the junction. Then the electrons are attracted to the positive charge in the n-type material while the holes are attracted to the negative charge in the p-type material. These changes modify the equilibrium charge concentration in the junction and if sufficient electron-hole pairs are formed, cause the photocurrent to flow in an external circuit.

In the case of the InSb detector, which has a band gap of about 0.23 eV at 77 K, incident radiation must be of wavelengths less than or equal to about 5.3μ to be absorbed. The InSb at 77 K has a quantum efficiency greater than 50 percent from 3.5μ to over 5μ making it an excellent detector for $4.3\text{-}\mu\text{m CO}_2$ band investigations. A typical InSb photovoltaic detector has a peak $D^* \approx 8 \times 10^{10} \text{ cm Hz}^{1/2}/\text{w}$. The short circuit current developed is linearly related to the irradiance on the detector over five or six orders of magnitude.

The frequency response of the photovoltaic detector is shown by the expression for photocurrent

$$i = QE q N_m \{1 - \exp(-j\omega T_r)\} / [j\omega T_r] \quad (B-9)$$

where m is the modulation index of the irradiance, and T_r is the drift transit time. Therefore, from the standpoint of the photoelectric phenomenon alone, the transit time has the dominant influence on the response of the detector. The dimension of the detector through which the carriers must travel should be as small as possible to minimize the transit time. Additionally, the associated capacitance, inductance, and resistance associated with a practical diode and circuit have a strong influence on the frequency response. For the typical InSb detector mentioned earlier, the D^* is nearly constant at modulation frequencies from about 10 Hz to about 100 kHz.

The HgCdTe detector operating at 77 K acts as a resistor whose value varies according to the number of photons falling on it. In this detector electrons in the valence band absorb the energy of the incident photons and are excited into free states in the conduction band. The electrons remain in the conduction band for a characteristic lifetime. Electrical conduction then takes place by the electrons in the conduction band or by the holes vacated in the valence

band. The resistance varies inversely with irradiance. The HgCdTe is a pseudo-binary alloy composed of the semimetal HgTe and the semiconductor CdTe. This composition permits a continuously adjustable band gap of -0.3 to 1.6 eV depending upon the ratio of CdTe to HgTe. The cutoff wavelength can therefore be tailored in the near infrared range according to the equation (a rewrite of $E = h\nu$)

$$\lambda_c = 1.24/E_g \quad (\text{B-10})$$

where λ is the threshold wavelength in microns, and E_g is the band gap in electron volts.

These photoconductive detectors are generally used with circuits which produce varying currents with fluctuating irradiance. In these detectors the free electron concentration, N_e , is related to the rate at which photons arrive at the detector, N , by

$$N_e = N Q E \tau_e \quad (\text{B-11})$$

where τ_e is the lifetime of the resulting excited electrons. Although a more complex situation occurs (involving changes in hole concentration, differing lifetimes of holes and electrons, and surface versus bulk behavior), it will be omitted for brevity. The change in conductivity, $\Delta\sigma$, is then

$$\Delta\sigma = N_e q u / (A l) \quad (\text{B-12})$$

where u is the electron mobility, q is the electron charge, l is the electrode separation, and A is the detector area. Then any current change, i , for a dc-biased photoconductor will be

$$i = \Delta\sigma A V / l \quad (\text{B-13})$$

The photoconductive HgCdTe detectors are capable of covering a wide portion of the near infrared spectrum in its various alloy compositions. A typical alloy has a cutoff wavelength in the vicinity of $14 \mu\text{m}$ and a peak D^* of $2 \times 10^{10} \text{ cm Hz}^{1/2}/\text{w}$. Generally as the cutoff wavelength is increased, the D^* is decreased.

The frequency response of the photoconductor is shown by the more complete representation of the optically induced current

$$i = Q E q N m \tau V \exp\{-j \arctan(\omega\tau)\} [1 + \omega^2\tau^2]^{-1/2} \quad (\text{B-14})$$

where m is the modulation index of the irradiance, and the other parameters are as previously mentioned. As this expression shows, a large τ is desirable for large current responsivity,

but a small τ is desirable for rapid frequency response. To obtain a flat frequency response means that the τ should be approximately equal to $1/(2\pi f)$ where f is the bandwidth of operation. In the typical HgCdTe detector referred to earlier, the τ is effectively constant at modulation frequencies from about 10 to about 300 kHz.

APPENDIX C

EOCOM MODULATOR SPECIFICATIONS

Type	Scanning Michelson
Beamsplitter mount	Quick change holder
Wavelength range	0.65 to 1000 μm
Maximum resolution	0.65 cm^{-1}
Maximum scan distance	8.9 cm
Maximum retardation	17.8 cm
Mounting mirror drive	Linear force motor
Moving mirror suspension	Symmetric air bearings
Velocity sensor	L. V. sync
Minimum scan time	1 sec
Sample generator	Laser reference
Maximum aperture size	10 cm
Zero retardation pulse	White light reference
Velocity error	Less than 1/2 percent
Sampling error	Less than 10^{-8} cm

APPENDIX D

DETECTOR ARRAY SPECIFICATIONS

Array model	Spiricon IR-64-42
Number of elements	64
Element spacing (center to center)	400 μm
Array length	25.6 mm
Element dimensions	360 \times 2000 μm
Pyroelectric material	LiTaO ₃
Window material	ZnSe
Clock rate	0.05 to 1.0 MHz
Voltage requirement	+ 5.0 and - 8.0 v
Optimum chopping frequency	15 Hz

Responsivity	180 v/w at 0.6328 μm
Noise, rms	80 nw at 15 Hz
Sensitivity, NEP	15 nw/[Hz] ^{-1/2} at 1 Hz
Saturation power	1.6 mw at 15 Hz
Dynamic Range at 200 Hz	2×10^4 rms noise

Reproduced by permission of Dr. C. Roundy (Ref. 45).

APPENDIX E

INFRARED MEASUREMENTS AND CALIBRATIONS

Figure E-1 shows the essentials of an infrared measurement. As can be seen a number of measurements can be considered. The radiance of the object might be in question or one of its properties such as emissivity. The transmission of the atmosphere might be the unknown or the radiant intensity of source B or C. In any case, all of the shown terms must be considered during the measurement process to produce a valid result.

Instrument calibration and characterization is essential to accurate measurements. The response of the instrument must be determined with known sources; its linearity or nonlinearity for possible inputs must be determined; parameters such as field-of-view, frequency, response, and the like must be known. During the body of this report, many of the parameters of interest have been discussed; however, the calibration remains to be outlined.

Figure E-2 shows the steps involved in calibrating the FTS. First, the calibration requirement is determined from the intended instrument calibration (for example, if the instrument is to be used for a transmission measurement, no calibration is required). Figure E-2 shows the steps required for a radiance measurement. First, an extended blackbody or other suitable calibration source is positioned to overfill the field-of-view of the instrument; second, data are acquired with the blackbody at a high temperature; later, data are acquired at a low temperature. The interferogram (IGRAM) from the low-temperature collection is subtracted from the high-temperature interferogram. The difference interferogram is then Fourier processed (that is, phase calculated, apodized, Fourier transformed, phase corrected, and stored) to produce an experimental difference spectrum. At this point a theoretical difference spectrum is calculated using Planck's equation for the temperatures that were used. The theoretical difference spectrum is then divided point by point by the experimental difference spectrum to produce an instrument response. This instrument response is valid for radiance measurements made with this FTS when background interferograms are collected as part of the measurement program. If background subtraction is not used, a slightly more involved calibration process is required to eliminate any instrumental biases.

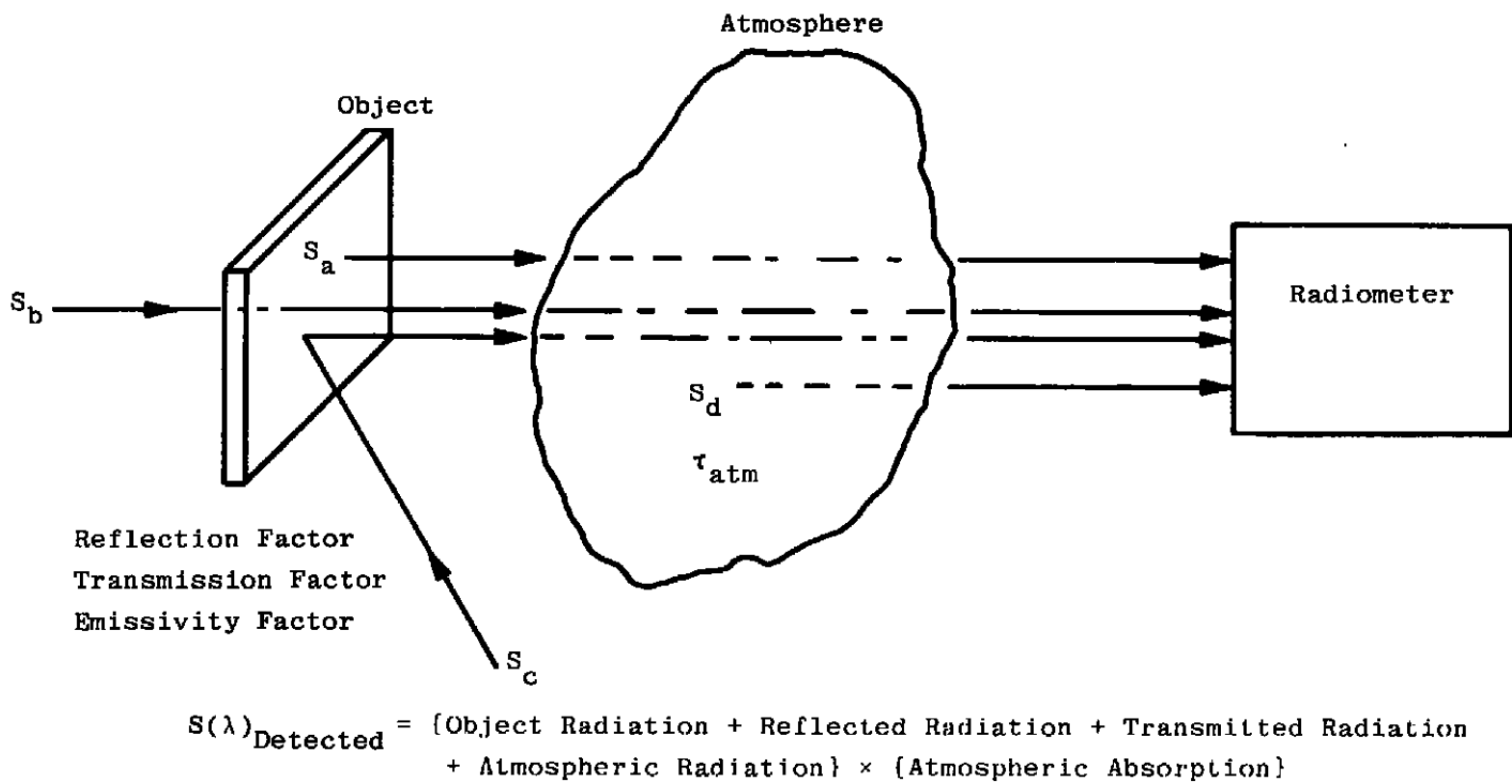


Figure E-1. IR measurement essentials.

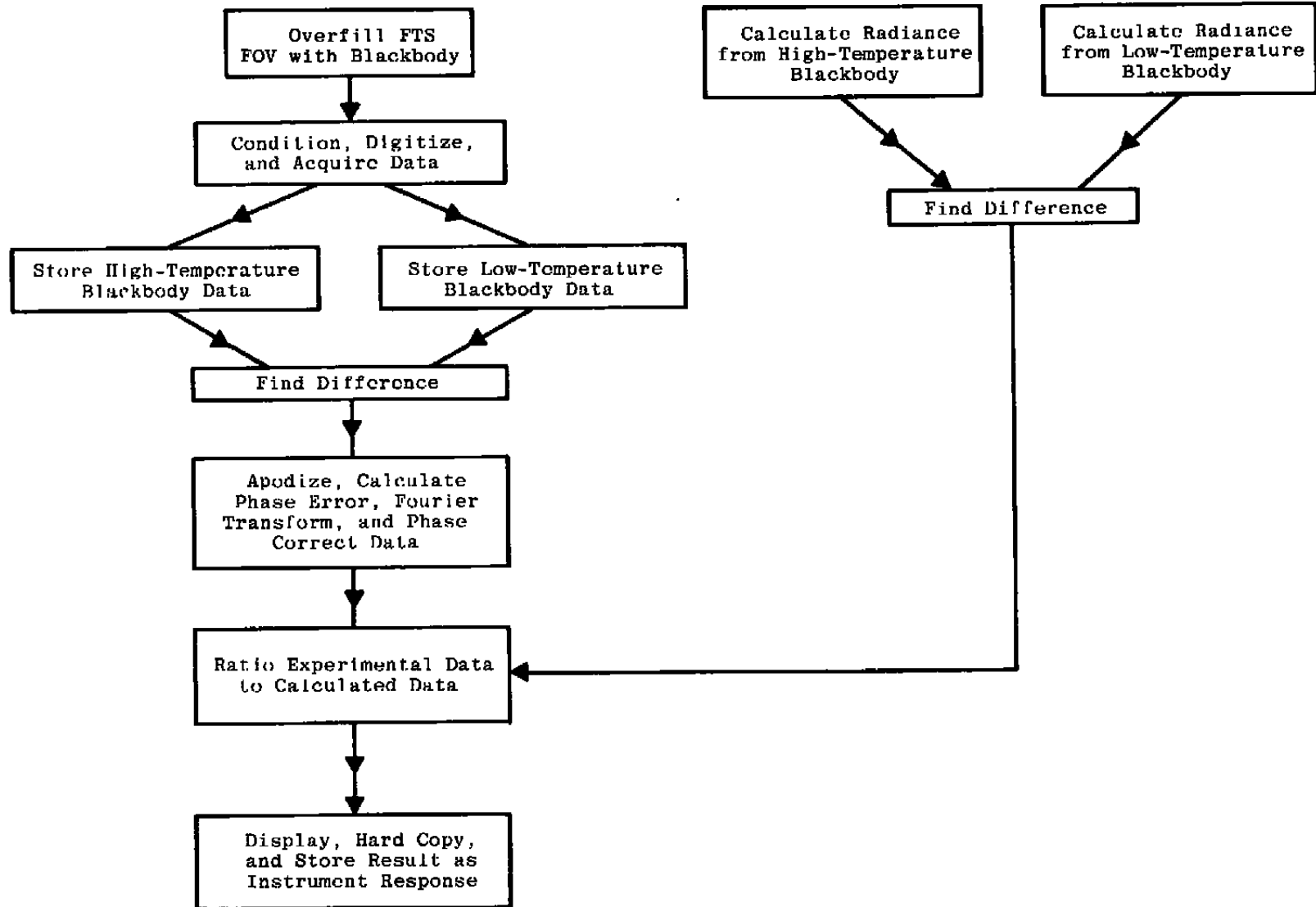


Figure E-2. Sequence of steps for FTS calibrations.

APPENDIX F

INFRARED SOURCES

The development described herein was aimed toward the hot gases (selective radiators) with entrained hot particles and the hot parts encountered in advanced propulsion systems. By virtue of the molecular and atomic agitation associated with their internal energies, these sources emit radiation in the form of electromagnetic waves. Table F-1 is a summary of the electromagnetic spectrum and quantities pertinent to this study. From Table F-1, it can be seen that the emitted energy or radiation from hot gases (flames) and thermal emitters is in the infrared, visible, and ultraviolet regions of the electromagnetic spectrum. Selected radiation production mechanisms for these sources are noted.

The spectroradiometric quantities of interest during the development of the IRIFTS include spectral radiance, spectral radiant intensity, spectral radiant exitance, and spectral irradiance. The concept of spectral irradiance is associated with the sensor, whereas the other quantities are associated with the source of radiation. Table F-2 summarizes these spectroradiometric quantities, their symbols, as used in this study, and includes an illustration for further clarity. A source is said to produce a spectral radiant energy, $W(\lambda)$, at a rate called the spectral radiant power or flux, $\phi(\lambda)$. A practical unit of spectral radiant energy is watt-second per micron; therefore, the unit for the spectral radiant flux is the watt per micron. The manner in which the flux leaves the source can be further qualified by specifying the quotient of the radiant flux leaving in a given direction divided by the solid angle element covered by the radiation. This quotient is called the radiant intensity, $I(\lambda)$, of the source. Since the unit of solid angle is steradians, the unit of radiant intensity is the watt per steradian-micron. This quantity is valid only for point sources. It is presumed applicable to extended sources if the entire source can be included within the instantaneous field-of-view of the viewing instrument. To further clarify the manner in which the source produces the radiation, two other quantities, the spectral radiant exitance and the spectral radiance, are also used. The spectral radiant exitance is the ratio of the radiant flux emitted from the surface divided by the area of the surface. Therefore, the spectral radiant exitance is the density of the radiant flux per unit area with units watts per square centimeter-micron. Spectral radiance is a source function relating the flux radiated from a unit area into a unit solid angle. The radiance is the quotient of the radiant intensity that passes through a surface element in a given direction divided by the projection of the surface element. The spectral radiance has units watts per steradian-square centimeter-micron. Both the spectral radiant exitance and spectral radiance are applicable to extended sources.

The quantities, transmission, τ , reflectivity, ρ , absorptivity, α , and emissivity, ϵ , are ratios. Transmissivity is the ratio of transmitted radiation to incident radiation. For example,

transmissivity is the ratio of spectral radiant intensity transmitted through a medium to the spectral radiant intensity incident upon that media. (The example could have been with either spectral radiances or spectral irradiances instead of intensity.) The reflectivity is the ratio of reflected radiation from an object to the radiation incident upon the object. The absorbtivity is the ratio of radiation absorbed by a medium to the radiation incident upon it. Emissivity is the ratio of emitted radiation from an object to the radiation emitted from a blackbody at the same temperature.

In a typical propulsion system (Refs. 53 through 56) the nozzle and other parts which operate at elevated temperatures fall into the thermal emitter category. Thermal emitters produce radiation that can be partially described by Planck's spectral distribution of emissive power equation

$$L = 2hc^2\epsilon / (\lambda^5 \{ \exp[hc/kT\lambda] - 1 \}) \quad (F-1)$$

where L is the spectral radiance of the source, ϵ is the spectral emissivity or measure of how well a body can radiate energy as compared to the blackbody, λ is the wavelength in microns, h is Planck's constant, k is Boltzmann's constant, T is the temperature in Kelvins, and c is the speed of light. Figure F-1 shows the spectral radiance, as a function of wavelength, as calculated from the equation for a series of blackbodies ($\epsilon = 1$) at different temperatures. As the figure and equation show, considerable energy is produced in the infrared. The presence of this source of radiation is of importance in weapons systems where thermal seekers are used.

The other source of interest in this study is the plume produced by the propulsion system. The plume is produced by a combustion process occurring in the region behind a rocket or jet engine and is an extremely complicated chemical and thermodynamic entity. In these typically complicated processes, there is rarely complete knowledge of the kinetics of both the series and the parallel chemical reactions occurring within the plume. Further increasing the magnitude of the complexity of the source is the fact that the selective radiation from the flame does not correspond to a relatively simple spectral distribution as did that from a blackbody. The character of the radiation from these sources is much more complex and difficult to treat than that from solid bodies. For the purposes of this study, the different models describing the production mechanisms do not need to be presented. It is sufficient that it be accepted that molecules or atoms exist in discrete energy states, and that the electromagnetic radiation emitted by an excited molecule appears only in discrete quanta of radiation. These quanta are called photons and are simply wave packets of finite length with energies proportional to their frequency, ν ,

$$E(\text{photon}) = h \nu \quad (F-2)$$

Table F-1 shows that the emissions from flames can be divided into rotational spectra caused by changes in rotational energy of a molecule, vibrational spectra caused by changes in vibrational energy of a molecule, electronic spectra caused by changes in energy of the molecule attributable to different electron arrangements, and to combinations of changes.

Common to most propulsion system plumes are the water and carbon dioxide molecules. In many types of plumes these molecules are abundant and are the major contributors to the infrared plume radiation. The water and carbon dioxide molecules are also present in the atmosphere surrounding the plume. In the atmosphere, however, they serve an opposite role. Water and carbon dioxide are the primary absorbers of infrared radiation in the atmosphere. Although scattering of radiation is a contributor, absorption is the major loss mechanism for infrared transmission. Within only a few feet of atmospheric transmission, losses can be significant. Figure F-2 is an uncorrected emission spectrum of a blackbody source through an atmospheric path of approximately 5 ft taken in the laboratory where the experimental part of this study was performed. The absorption in several of the major bands is very apparent. Molecular absorption is a rapidly varying function of wavelength. There are spectral regions with virtually no transmission and others, called windows, which transmit IR radiation for significant distances. The molecular absorption is a function of the concentration and pathlength. Like the emission from selective radiators, this related phenomenon is too complicated and of insufficient importance to this study to be presented.

Transmission is a consideration for all the transmitting components within any optical path, including windows, lenses, and the like, in addition to the atmosphere. Presently our attention will remain with the atmospheric transmission.

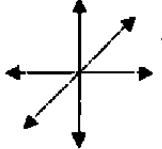
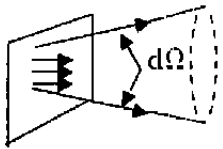
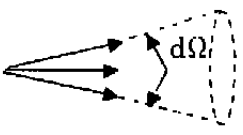
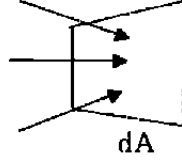
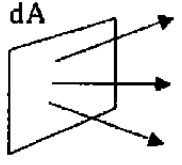
The range to the sources treated in this study were usually 3 to 10 ft. For the purposes of this study, the absorption losses will be accepted, noted, and otherwise ignored. For the purposes of other applications, with longer optical paths, the atmospheric losses can be calculated with commonly available atmospheric models, and measured spectra can be "corrected" to give, with a high degree of certainty, the true source spectrum.

Another area that must be remembered and considered is the target background. The background is any radiation additional to the source radiation that can confuse the source measurement. The background is therefore another, albeit unwanted, source within the field-of-view. For the imaging system under development, background problems are reduced over nonimaging systems because an imaging system provides spatial discrimination for objects, such as source and background, within its field-of-view. There are additional background problems the imaging systems do not resolve. One example is the reflection of radiation from a wall behind a semitransparent plume. In most measurements the background must be considered.

Table F-1. Typical Radiation Sources, Types, Spectral Range, and Appropriate Detector

Sources	Radiation	Wavelength, μm	Wave number, cm^{-1}	Detectors	Selected Production Mechanisms
Radioactivity	Cosmic Rays	10^{-6}	10^{10}	Scintillation Counters	① Electronic transitions in gases
	γ Rays	10^{-5}	10^9	Nuclear Emulsions	② Vibration-rotation transitions in gases, Molecular vibrations in solids and liquids
Electron Bombardment, X-Ray Tubes	Hard X-Rays	10^{-4}	10^8	Ionization Detectors, Geiger tubes	Bound electron transitions in solids
	Soft X Rays	10^{-3}	10^7		
Thermal Emitters		10^{-2}	10^6	Photographic Emulsions	
Flames	Ultraviolet	10^{-1}	10^5	Photoelectric Devices	①
Gas Discharges, Lasers, Arcs, Sparks, Plasmas	Visible	1	10^4	Thermal Devices	②
	Infrared	10^1	10^3	Photoconductive Devices	③
		10^2	10^2		
Electromagnetic Generators		10^3	10	Electromagnetic Detectors	
	Microwave	10^4	1		
		10^5	0.1		③ Rotation transitions in gases, Lattice vibrations in solids

Table F-2. Radiometric Units

Name	Symbol	Dimension	Units	
Spectral Radiant Power	Φ_λ	$\frac{\text{Power}}{\text{Wavelength } (\lambda)}$	$\frac{\text{Watt}}{\mu\text{m}}$	 $\Phi_\lambda = \frac{d^2w}{d\lambda d\Omega}$ <p>$W = \text{Radiant Energy}$</p>
Spectral Radiance	L_λ	$\frac{\text{Power}}{\text{Area} \times \text{Solid Angle} \times \lambda}$	$\frac{\text{Watt}}{\text{cm}^2 \text{ sr } \mu\text{m}}$	 $L_\lambda = \frac{\frac{d^2J_\lambda}{d\lambda \cos\theta d\lambda}}{\text{or} \frac{d^2J_\lambda}{dA \cos\theta d\Omega d\lambda}}$
Spectral Radiant Intensity	I_λ	$\frac{\text{Power}}{\text{Solid Angle} \times \lambda}$	$\frac{\text{Watt}}{\text{sr } \mu\text{m}}$	 $I_\lambda = \frac{d^2\phi_\lambda}{d\Omega d\lambda}$
Spectral Irradiance	E_λ	$\frac{\text{Power}}{\text{Area} \times \lambda}$	$\frac{\text{Watt}}{\text{cm}^2 \mu\text{m}}$	 $E_\lambda = \frac{d^2\phi_\lambda}{dA d\lambda}$
Spectral Excitance	M_λ	$\frac{\text{Power}}{\text{Area} \times \lambda}$	$\frac{\text{Watt}}{\text{cm}^2 \mu\text{m}}$	 $M_\lambda = \frac{d^2\phi_\lambda}{dA d\lambda}$

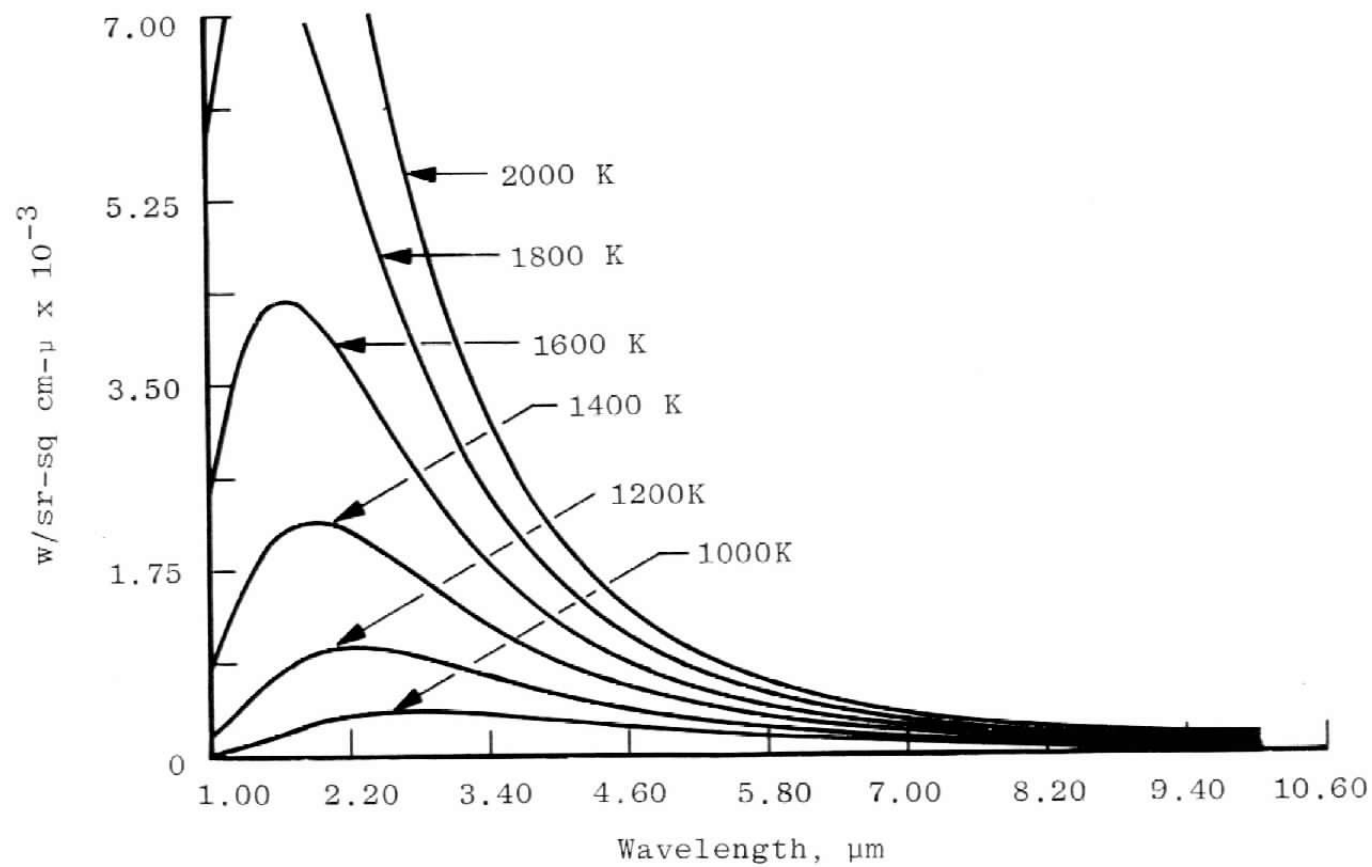


Figure F-1. Blackbody radiances.

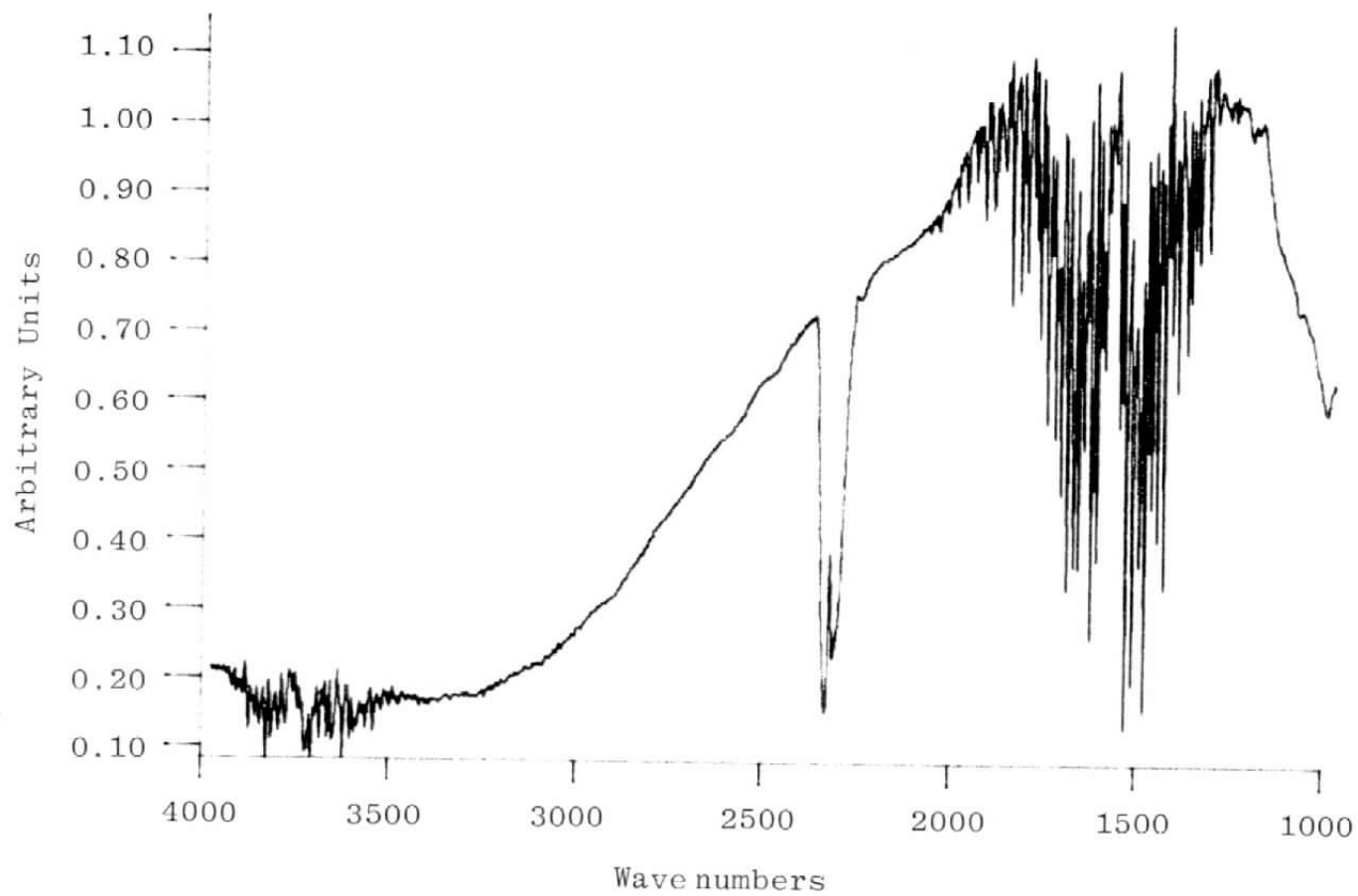


Figure F-2. Uncorrected emission spectrum.

The variation of a source as a function of time is another critically important factor. In this study, where the ultimate sources of interest are propulsion systems, a variety of source temporal characteristics are experienced. In solid-propellant rocket motors the plume radiance can vary rapidly and in some cases may be of very brief duration. For small tactical missiles the engine may operate for only a few seconds, whereas for other missiles and jet engines, combustion may continue for minutes or hours. With certain types of missiles, a booster may be used in the launch and a different motor or propellant used to sustain the missile flight; therefore, two or more radically different types of sources (the radiation from the boost as well as the sustain phase) may be encountered. For jet engines operating conditions will also significantly alter the radiation from the plume. Since the radiation can vary dramatically with time, it is important that a measurement system have an adequate response time to deal with the fluctuations of the source.

For the present study, several additional source characteristics are important. Peculiar to the Michelson-type interferometer are the sources' temporal and spatial coherence and stability. The time coherence is of interest since the interference phenomenon is dependent upon temporal coherence of the radiation during its transit through the modulator. Time coherence (Refs. 56 and 57) (related to the bandwidth by the uncertainty relation $\Delta t \Delta \sigma \leq h/4\pi$ for typical sources of interest) is approximately 10 sec and is therefore adequate for an interferometer with 1-m retardation, adequate for 0.01-cm^{-1} resolution. Spatial coherence that could add to the complexity of the measurement if present in any significant degree will not be addressed because of lack of spatial coherence in sources of interest herein. More information on the effects of coherence in radiometry is available in studies by Friberg, and Berran and Parrent (Refs. 58 and 59).

The source radiance, L , can be expressed as a function of spatial position (x,y) , time (t) , as well as spectral frequency (σ) or wavelength (λ) . With each of the independent variables there are associated considerations that can not be overlooked in the development of a measurement system. After the previously mentioned issues have been resolved, the more general considerations such as the dimensions of the source and the dynamic range of the radiances at different positions and wavelengths must then be considered.

NOMENCLATURE

A	Area, cm^2
B	Magnetic field
C	Conductivity
c	Specific heat or speed of light
D	Detectivity
D*	Dee-star, normalized detectivity
d	Distance, cm
E	Irradiance, w/cm^{-1}
e	Excited electron lifetime
F(T)	Pyroelectric Coefficient
f	Focal length or frequency
h	Planck's constant
I	Radiant intensity, w/sr
i	Current, amp
K	Thermal conductance
k	Boltzmann's constant or the propagation vector
L	Radiance, $\text{w/cm}^{-1}\text{sr}$
l	Length, cm
M	Emittance, w/cm^{-1}

m	Modulation index
N	Noise of average number of photons/second
n	Index of refraction
NEP	Noise equivalent power
NF	Noise figure
Q	Power, w
QE	Quantum efficiency
R	Responsivity
r	Retardation or reflection coefficient, percent
S	Poynting vector
T	Temperature, Kelvins
t	Time or transmission coefficient
u	Electron mobility
V	Bias voltage, v
v	Velocity, cm/sec
W	Radiant energy
α	Absorptivity, percent
δ	Mirror Displacement, cm
ϵ	Emissivity, percent
ϵ	Permittivity constant

θ	Angle, deg
λ	Wavelength, μm
μ	Permeability constant and μm
ν	Frequency, Hz
ξ	Electric field
ρ	Reflectivity, percent
σ	Wave number or Stefan-Boltzmann's constant
τ	Transmissivity or time constant
T	Half-angle obliquity limit
ϕ	Phase difference or radiant flux
Ω	Solid angle, sr
ω	Angular Frequency, radians/sec